ALGORITHMS AND METHODOLOGY FOR INCOHERENT UNDERSAMPLING BASED ACQUISITION OF HIGH SPEED SIGNAL WAVEFORMS USING LOW COST TEST INSTRUMENTATION

A Dissertation
Presented to
The Academic Faculty

By

Debesh Bhatta

In Partial Fulfillment
of the Requirements for the Degree
Doctor of Philosophy
in
Electrical and Computer Engineering

School of Electrical and Computer Engineering
Georgia Institute of Technology
December 2014

ALGORITHMS AND METHODOLOGY FOR INCOHERENT UNDERSAMPLING BASED ACQUISITION OF HIGH SPEED SIGNAL WAVEFORMS USING LOW COST TEST INSTRUMENTATION

Approved by:

Dr. David Keezer, Committee Chair
Professor, School of ECE
Georgia Institute of Technology

Dr. Linda Milor
Asst. Professor, School of ECE
Georgia Institute of Technology

Dr. Abhijit Chatterjee, Advisor
Professor, School of ECE
Georgia Institute of Technology

Dr. Atri Dutta
Asst. Professor, Aerospace Engineering
Wichita State University

Dr. David Anderson
Professor, School of ECE
Georgia Institute of Technology

Date Approved: December 2014

To my parents, teachers and friends

ACKNOWLEDGMENTS

I will take this opportunity to thank all the people without whose support it would have been impossible to cover the journey that led to this thesis.

First and foremost I would like thank my parents for their love and wisdom that helped me to survive the long and sometimes intimidating journey of the PhD. I would also like thank my brother and sister for their love.

Special thanks to my adviser Prof. A Chatterjee without whose support I would have been lost in the maze of research. Equally important was the support form all the current and past members of the Test and Reliability Engineering Lab, Jayaram Natarajan, Senwen Hsiao, Jigar Doshi, Josh Wells, Nicholas Tzou, Xian Wang, Thomas Moon, Barry Muldrey, Suvadeep Bannerjee, Sabyasachi Deyati, Debashis Bannerjee, Aritra Bannerjee, Shreyas Sen, Shyam Devorakond, Vishwanath Natarajan, and Hyun Choi.

I would like to thank Prof. David Anderson, Prof. Linda Milor, Prof. David Keezer, and Prof. Atri Dutta for their time and valuable comments. I would also like to acknowledge the role played by Dr. Joy Laskar and all the members of the erstwhile MAG group especially, Dr. Chris Scholtz, Dr. Edward Gebara, Kill-hoon Lee, Hyoung-soo Kim, Eric Juntunen, Kevin Chuang, Franciscu Barale, Gopal B. Iyer, Jun-hui Hoor, Shih-che Hsin and all the other members whom I forgot to mention by name.

It would be impossible to forget the contributions of James Steinberg, Bob House, and Kevin Pham who went out of their way to assist with the PCB board fabrication for hardware prototypes.

I would also like to thank Suriyaprakash Natarajan and Prashant Goteti of Intel Corp. for their valuable feedback. Equally important was the help and guidance provided by Ganesh Srinivasan, and Friedrich Tentzler of Texas Instruments.

I would like to acknowledge the role played by the ORGT and all its members especially David Knobbe, Lane Outz, Will Grier, Rob and Erin Hayward, Becca Winarski, Venkata Damaraju, Julia McMinn, David McNair, Kyle Gouchenour and Aaron Mosher who made

my years in Atlanta much more enjoyable as we shared together many adventures.

I would like to thank all my friends in Atlanta without whose support the journey would have been much more difficult. Special thanks to Mrinmoy Ghosh, Bevin Perumanna, Saikat Sarkar, Padmanava Sen, Tonmoy Mukherjee, Prabir Saha, Subho Chatterjee, Rishiraj Bheda, Sagar Uplanchiwar, Pawan Moradia, Aditya Devurkar, Ram, Gokul Kumar, Vijay Sukumaran, Kalyan Chakravarthi G., Amey Kaloti, Arindam Basu, Ken Chiu, and Salman Asif.

I would like to acknowledge the role played by all my teachers throughout my life as I am deeply indebted to them. Last but not least, special thanks to George Cham who I never met in person but his wonderful comics never failed to lighten up the day when things looked gloomy.

TABLE OF CONTENTS

LIST OF FIGURES

ACRONYMS

ADC analog to digital converter.

BERT bit error rate tester.

CS compressive sensing.

DAC digital to analog converter.

DAq data acquisition system.

DBI digital bandwidth interleaving.

DUT device under test.

ETS equivalent time sampling.

FFT fast Fourier transform.

FPE Fokker-Planck equation.

IFFT inverse fast Fourier transform.

IUS incoherent under-sampling.

LMS least mean square.

LO local oscillator.

PDF probability density function.

PRBS pseudo random bit sequence.

RF radio frequency.

RIS random interleaved sampling.

SDE stochastic dynamic equation.

SFDR spurious free dynamic range.

SNR signal to noise ratio.

THA track and hold amplifier.

TIS time interleaved sampling.

SUMMARY

The objective of this research is to develop and demonstrate low-complexity, robust, frequency-scalable, wide-band waveform acquisition techniques for testing high speed communication systems.

High resolution waveform capture is a versatile testing tool that enables flexible test strategies. However, waveform capture at high data rates requires costly hardware because the increased bandwidth of the signal waveform leads to an increase in the sampling rate requirement, cost of front-end components, and sensitivity to phase errors in traditional (source) synchronous Nyquist-rate tester architectures. The hardware cost and complexity of wide-band waveform acquisition systems can, however, be significantly reduced by using (trigger-free) incoherent undersampling to achieve reduced sampling rates and robustness to phase errors in signal paths. Reducing the hardware cost of such a system using incoherent undersampling requires increased signal processing at the back end.

This research proposes computationally-efficient, time-domain waveform reconstruction algorithms to improve both performance, and scope of existing incoherent undersampling-based test instrumentation. Supporting hardware architectures are developed to extend the application of incoherent undersampling-based waveform acquisition techniques to linearity testing of high-speed radio-frequency components without any synchronization between the signals involved, and to the acquisition of wide-band signals beyond the track-and-hold bandwidth barrier of the traditional incoherent undersampling architectures, using multi-channel bandwidth interleaving. The bandwidth is extended in a source-incoherent framework by using mixers to down convert high-frequency signal components to base band followed by digitization using undersampling, and back-end signal processing to reconstruct the original wide-band signal from multiple band-pass components.

CHAPTER 1

BACKGROUND AND PROBLEM DEFINITION

1.1 Introduction

As data rates in communication links increase towards 100 Gbps enabled by rapid technology scaling and innovative system level solutions, the test equipment for characterizing the signals becomes prohibitively costly. The cost is driven mainly by the higher sampling rate requirement of Nyquist-rate data converters due to increased signal bandwidth, and by the high engineering cost of achieving phase synchronization between the source and the tester at high data rates for source-synchronous sampling-based waveform acquisition systems. Incoherent sub-sampling has been investigated by various researchers to alleviate the costs associated with acquiring high-speed signals. Incoherent undersampling-based techniques achieve lower hardware complexity since they use trigger-free periodic sampling at sub-Nyquist rates. Such systems do not require any phase synchronization between the tester and the source clocks and achieve a significant reduction in the conversion rates of the analog to digital converters. However, traditional incoherent undersampling suffers from the high cost of back-end signal processing particularly when the period of the input signal is not precisely known in the absence of triggering mechanisms traditionally used for source-instrument synchronization. In such scenarios, most of the cost of signal reconstruction results from the cost of performing frequency-domain transformations and evaluating a frequency-domain metric to estimate the period of the acquired periodic waveform. In addition, the ability to acquire high-bandwidth signals is also limited by the bandwidth of the wide-band track-and-hold amplifier used to sample the analog signal in the signal-acquisition system front-end.

The key contributions of this dissertation are as follows:

- This research develops and demonstrates low computation-complexity, time-domain incoherent undersampling-based input signal reconstruction algorithms and support

hardware modules, that do not require the use of digital Fourier Transformation algorithms as in existing incoherent undersampling based signal acquisition methods

- To meet the demands of acquiring high-bandwidth signals, it applies for the first time, novel time-domain incoherent undersampling-based signal reconstruction algorithms to (frequency) band-interleaved signal acquisition architectures. This has the additional benefit of surmounting the bandwidth limitations of the track and hold amplifiers in the signal acquisition system front-end through use of narrow-band mixers in each channel of the band-interleaved system. Such band-interleaved systems are traditionally used in high-speed oscilloscopes for acquisition of high-speed signals using coherent sampling (with triggering for clock synchronization)

- A key contribution of this research is that it develops signal reconstruction algorithms and infrastructure that do not require any synchronization between the source and the tester clocks, significantly simplifying the design and implementation of the end-to-end high-speed signal acquisition systems

- This research proves the applicability of the proposed techniques by developing waveform-acquisition modules to acquire both wide-band periodic signals, as well as narrow-band amplitude-modulated signals. It also demonstrated a novel tester architecture for radio-frequency amplifier linearity test using amplitude modulated signals

The challenges of high-speed waveform acquisition will be elaborated in the next section in order to present the background of this research.

1.2 Challenges of high-speed waveform acquisition

This section, presents in detail the specific challenges associated with high-speed waveform acquisition. The major challenges include hardware complexity, algorithmic computation cost and frequency scalability.

1.2.1 Hardware cost

A major barrier to reducing the cost of high-speed test equipment comes from the high rate of data conversion vis-a-vis the large number of bits required when using traditional Nyquist rate architectures. The issue can be solved by using undersampling-based techniques, but classical undersampling-based equipment uses either undersampling in a coherently-triggered setup, in which the effective sampling rate is boosted by directly combining signals from multiple parallel channels in time domain, or by sampling a periodic signal with a source-synchronous sampling clock whose synchronizing trigger is provided by the signal source. However, at high data rates (reduced bit period), it is not only extremely costly, but also practically impossible to achieve phase synchronization, because of small manufacturing imperfections. Incoherent undersampling-based architectures bypass the need for synchronization altogether. However, incoherent undersampling-based techniques using periodic sampling are effective for a very limited class of signals that are mostly periodic. Using incoherent undersampling-based architecture, reduces the cost and complexity of test instrumentation, although it does increase the signal processing effort required at the back-end.

1.2.2 Computation cost

In an incoherent undersampling-based waveform-acquisition architecture, the period of the signal waveform is unknown and needs to be estimated from the acquired samples. The estimation accuracy usually improves with the number of samples acquired due to the fundamental limits imposed by uncertainty relationships between the time domain and the frequency domain. However, the computation effort required to estimate the waveform period and reconstruct the waveform grows with the number of samples and, is especially large for classical frequency-domain metric-based period estimation algorithms, which require the estimation of the spectra at each iteration. This makes it necessary to design efficient incoherent undersampling-based waveform-reconstruction algorithms to reduce the computation effort without sacrificing the estimation accuracy.

1.2.3 Bandwidth scaling

Another challenge of the undersampling-based architecture is the problem of scalability to higher frequencies. The lack of phase synchronization in an incoherent undersampling-based system is advantageous at higher frequencies where phase synchronization becomes harder to achieve because of reduced timing margins. However, the maximum bandwidth of the classical sampling digitizer system is limited by the bandwidth of the front-end component, usually a track-and-hold amplifier. Since wide-band track-and-hold amplifiers are hard to scale in frequency, it is necessary to develop systems that are easily scalable to a higher frequency range without the requirement of wide-band track-and-hold amplifiers at high frequency ranges.

1.2.4 Applicability

The classical periodic undersampling-based waveform reconstruction algorithms are limited to periodic signals. This excludes the possibility of applying the undersampling-based reconstruction techniques to the high-frequency, narrow-band, waveforms used in radio-frequency linearity testing. Often times, the multi-tone waveforms used in radio frequency testing are derived by modulating a periodic carrier with a periodic envelope giving rise to waveforms that are not periodic or that have extremely long periods. New algorithms need to be developed to extend the periodic undersampling-based waveform reconstruction techniques to radio frequency testing applications.

The specific contributions of this thesis addressing the above problems are presented in the next section.

1.3 Proposed solutions

As mentioned earlier, the major contributions of this dissertation involve the development of algorithms and hardware modules for high-speed waveform acquisition. The proposed techniques target solutions to reduce the cost of high-speed waveform capture in test applications by removing the major cost barriers, which include the high conversion rate required in classical Nyquist-rate converters and the cost of achieving phase synchronization

between the signal source and the test equipment.

The proposed techniques include, incoherent undersampling and bandwidth interleaving, along with computationally efficient back-end algorithms to reconstruct test waveforms with high accuracy. These techniques achieve a reduction of the overall cost of the test system by not only reducing the number of high-speed components required, but also the computation effort required in the back-end signal processing. The next few subsections expand upon each of the major contributions.

1.3.1 Time domain reconstruction algorithms

As mentioned before, the cost of waveform reconstruction using incoherent undersampling is dominated mainly by the algorithmic cost of estimating the fundamental period of the input waveform. The period estimation algorithm usually requires a large number of iterations involving a high-resolution serial-search algorithm using a discriminating metric. Previous solutions involving frequency-domain metrics required the evaluation of the spectrum by using a fast Fourier transform (FFT) at each iteration. Even though the FFT based algorithms were very efficient, the computation cost added up very fast due to the large number of iterations. Hence, this research develops a simple, low-cost, time-domain metric to address the issue of computation cost. The proposed metric uses a 1-bit approximation of the signal to count the number of oscillations in the reconstructed waveform about the average value. The time-domain metric is $O(n)$ complexity compared to the $O(nlogn)$ complexity of an FFT based algorithm.

1.3.2 Incoherent bandwidth interleaving

The classical technique of incoherent undersampling is limited to periodic signals with a bandwidth that is less than the track-and-hold amplifier bandwidth. This work extends the classical incoherent undersampling based technique to signals with frequency components beyond the track-and-hold bandwidth, while maintaining the trigger-free waveform acquisition framework. The signal is acquired using a bandwidth-interleaving-based configuration, where the signal waveform is acquired over multiple channels of smaller bandwidths.

The bandwidth of each channel is limited to that of the track-and-hold amplifier. The signal in each channel is down-converted in frequency by mixing with a locally generated (tester side) tone to the base band before being digitized by incoherent undersampling. The signal from the multiple channels are then combined in the back end to reconstruct the original broad-band signal waveform. The proposed architecture combines bandwidth interleaving and incoherent undersampling to provide a (source) trigger-free, time-domain waveform reconstruction scheme beyond the track-and-hold amplifier bandwidth.

1.3.3 Applicability: Wide-band periodic waveforms and an RF linearity test

While the incoherent undersampling-based reconstruction techniques provides an efficient solution for acquiring wide-band periodic waveforms, radio frequency (RF) testing often involve multi-tone signals that are often not periodic or have extremely long period. A modified time-domain reconstruction algorithm along with a supporting trigger-free hardware architecture is developed to extend the classical incoherent undersampling-based technique to possibly non-periodic, narrow-band signal waveforms. More specifically, the proposed technique covers the class of waveforms that includes narrow-band amplitude modulated signals, modulated with periodic envelopes. Such signals, as mentioned before, are not necessarily periodic (or may have a very long fundamental period) and are usually used in the testing and characterization of RF transmitter components. The proposed reconstruction method extracts the carrier period and the envelope period independent of each other to enable the extraction of instantaneous amplitude and phase information of the amplitude modulated waveform. The developed technique is easily scalable to higher frequencies.

While developing low-complexity, robust, test equipment and reconstruction algorithms remains the main focus of this dissertation, an efficient simulation flow is also presented to estimate the input-output observability of extreme parametric deviations and gross faults in a system under test.

1.4 Organization of thesis

Chapter 2 gives a brief overview of the existing solutions and state-of-the-art. Chapter 3 then presents the details of the time-domain reconstruction algorithm for incoherent undersampling based signal waveform acquisition. Chapter 4 presents an extension of the technique to general multi-tone signals for radio frequency linearity testing. Chapter 5 extends the basic time domain technique to frequencies beyond that of the track and hold amplifier bandwidth. Lastly, Chapter 6 presents a mixed signal simulation framework to enable the rapid assessment of the fault observability in mixed signal systems using the proposed test techniques. This will be followed by conclusions and a brief description of the possible future course of the presented research.

CHAPTER 2

PRIOR WORK

The test strategies used in identifying faulty units involve both on-chip and off-chip solutions. While on-chip test solutions can provide observability at the internal nodes of the system, often times, the accuracy of the system is limited by practical issues associated with the design overhead. The achievable resolution is limited by the fact that the on-chip components are subjected to the same technology limitations as the system-under-test and are severely restricted in available area and power.

Off-chip test board based solutions, on the other hand, often rely on costly high-end equipment such as bit error rate tester (BERT), and oscilloscopes that can capture signal waveforms with high resolution to measure the bandwidth, dynamic characteristics and the compliance of the eye opening of the signal to the standard specifications. Additionally, a large part of the equipment cost is geared towards the ability to measure jitter performance of the system. Most of these systems use triggered sampling for synchronizing with the signal source.

This chapter reviews the state-of-the-art in the most common test solutions used today for high speed waveform acquisition and briefly reviews the underlying system simulation framework that is used to determine the decision boundaries in the measurement space.

2.1 On chip test solutions

While on-chip test solutions are limited in choice and accuracy, a few techniques are extremely common. One of these is eye monitoring which is a close on-chip analogue, for general class of random bit streams, of a full waveform acquisition system for periodic bit streams using off-chip components. The eye diagram is obtained by folding the digital signal waveform over one bit period in time. Most modern serial communication systems have a built-in eye-margin circuit, that samples the signal at varying phase and amplitude

offsets from the optimal sampling point over a unit interval of the data using variable-threshold comparator latches. At each point, the error rate is measured and mapped to produce an approximate bit error map over the whole signal eye. Eye opening monitors not only provide direct signal quality information at the core of the decision block as an indicator of the system health, but can also double up as a feedback sensor for tuning the equalizer filters. Many different solutions for eye opening monitors have been proposed in the literature[1, 2, 3, 4, 5].

However, on-chip test solutions, unlike off-chip test instrumentation suffer from three major drawbacks:

- Power and area overhead
- Susceptibility to process variation
- Unwanted loading effects at critical nodes

In light of the above shortcomings, the main focus of this thesis will be on developing off-chip waveform acquisition algorithms and hardware for the characterization of wide-band signal waveforms. The next subsection, presents a review of the past work in the field of wide-band signal waveform acquisition using off-chip components.

2.2 Undersampling-based off-chip waveform acquisition

The different architectures used for on-chip eye-monitoring circuits, usually sampling at an integer fraction of the bit rate, require very high-speed on-chip components such as track and hold amplifier (THA), latches, and comparators. Traditional off-chip test equipment, on the other hand, samples the data waveform faster than the Nyquist rate (NRS) to prevent aliasing. The high-speed data acquisition system (DAq) circuits required to achieve oversampling increase the cost of the test instrumentation. To reduce the sampling rate of each data channel without reducing the effective sampling rate, [6] proposed time interleaved sampling (TIS) in which, the waveform is acquired over N parallel channels. The sampling clock in each channel is offset in phase by $1/N$ of the clock period with respect to

its adjacent channel. The samples from all the channels are combined to obtain an effective sampling rate of N times that of each channel. However, TIS is very sensitive to gain and timing mismatch between the channels [7, 8, 9]. In a TIS-based system, a small amount of mismatch between the channels causes harmonic-distortion spurs in the acquired waveform by the regular and periodic excitation of the mismatch induced non-linearity. The harmonic spurs reduce the effective spurious free dynamic range (SFDR) of the system, leading to a loss of resolution. To reduce the harmonic spurs, [10, 11] proposed a technique called random interleaved sampling (RIS) which achieves a reduction of the harmonic spurs by randomizing the order in which each of the N channels is used to acquire the samples. However, extra channels are needed to ensure that the sampling rate in each channel does not exceed $1/N$ of the overall effective sampling rate.

Compressive sensing (CS), as proposed in [12], reduces the effective sampling rate of a sparse signal so that it is proportional to the actual spectral support of the signal instead of the bandwidth of the signal. However, CS requires complex sampling time bases in which the minimum sample-to-sample interval is much smaller than the mean sampling period, leading to no relaxation of the specifications on the THA sampling window and maximum sampling rate requirements of the data converters. However, the complex sampling time base used in CS is not required for periodic signals. Since most testing and characterization can be done with periodic signals, the signal acquisition systems for test-bed applications, can be simplified by exploiting the periodic nature of the waveform. One such solution, equivalent time sampling (ETS), is traditionally used to reconstruct periodic signals through periodic undersampling in sampling oscilloscopes [13]. The samples are acquired by a source-synchronous clock whose period is a rational multiple of the waveform period. The samples are folded into a single period of the waveform to reconstruct the waveform using phase remapping, where the samples are ordered in ascending order of the modulo of the sampling time with respect to the waveform period. The effective number of samples per period is given by the denominator of the ratio of the waveform period to the sampling period when expressed as an irreducible ratio of co-prime integers. As the main

shortcomings, the ETS technique has:

- limited effective sampling rate over one period
- requirement of phase lock between source clock and sampling clock

To overcome the above shortcomings of the ETS, [14, 15] proposed incoherent (trigger-free) undersampling-based eye diagram acquisition and blind period estimation technique. In the proposed incoherent undersampling-based system, the sampling period is randomly chosen, and the waveform period is estimated by searching over a range of test values, for each of which a test reconstruction of the waveform is performed by folding the samples into a single period. The accurate period is given by the value of the period that maximizes the horizontal eye opening or alternatively minimizes the number of peaks and the standard deviation of the probability distribution function of the jitter after reconstruction. These techniques can be easily extended to periodic signals. In a similar approach proposed in [16, 17], the cost function is modified to promote the spectral sparsity of the reconstructed waveform by minimizing the l_1 norm (sum of the absolute values of all the components) of the spectrum of the reconstructed signal. The search space is reduced, by initially estimating the period by directly computing the spectra of the uniformly under-sampled waveform under the assumption that the waveform period corresponds to the spectral peak of the acquired samples. Then two sets of samples are acquired at two different sampling frequencies to remove potential aliasing. The exact position of the peak of the aliased signal spectrum is approximated by Gaussian interpolation of the power spectra. The main problem of this technique is that it requires the presence of a dominant fundamental tone in the signal waveform. Such a dominant fundamental tone is not always present in general test signals. Another problem is that, the estimation of the spectrum of the reconstructed waveform at each iteration of the search space for the fundamental period is computationally cost intensive. In order to extend the applicability of the incoherent undersampling-based waveform acquisition to possibly non-periodic waveform, [18] proposed a dual frequency, two-channel sampling technique to create a compressive-sensing time base to acquire wide

band signals without reducing the minimum time between the samples in each channel. However, the technique suffers from the high algorithmic complexity and issues with frame synchronization between the channels.

A brief comparison of these ETS-based techniques and Nyquist rate sampling is presented in Table 2.1. All the techniques presented in Table 2.1, suffer from the bandwidth limitation imposed by the bandwidth of the front-end track-and-hold amplifier. This bandwidth barrier can be broken, however, by using bandwidth-interleaving architectures. A detailed survey of bandwidth-interleaving-based test instrumentation is presented in the next subsection.

Table 2.1: A comparison of different sampling techniques for periodic waveforms between Nyquist rate sampling (NRS), time interleaved sampling (TIS), random interleaved sampling (RIS), equivalent time sampling (ETS), and incoherent sub-sampling (ISS)

Sampling method	Minimum sample clock rate	Hardware requirements	Prior information of signal time base required(no aliasing)?
NRS	2 times bandwidth	High speed single channel	Yes
TIS	2 times bandwidth /N	Low speed N channels	Yes
RIS	2 times bandwidth /N	Low speed > N channels	Yes
ETS	slow, source triggered	Low speed single channel	Yes
ISS	limited by accuracy of back end algorithm and phase drifts	Low speed single channel	No

2.3 Bandwidth interleaving

Bandwidth interleaving can be considered as the frequency domain dual of the time interleaving. It is also known as a hybrid filter bank analog to digital converter (ADC) architecture. In bandwidth interleaving, the signal waveform is divided into multiple components of smaller bandwidths. Each component is digitized separately at Nyquist rate and combined after is corrected for the channel-induced distortions to obtain the actual signal waveform. A multi-band data acquisition architecture exploiting band-pass sampling theorem was first proposed in [19]. However, the technique suffered from the requirement of multiple band-pass filters with reasonably low in-band dispersion, and high out-of-band rejection. To ease the specification requirements on the band-pass filters, [20, 21] later proposed a modified architectures based on mixers. In [22], bandwidth interleaving was used to acquire wide-band digital signals in real time by sampling each individual channel at a rate faster than the corresponding Nyquist rate. However, if restricted to the special case of periodic test waveforms, frequency scalability of the bandwidth interleaving technique can be further improved by using incoherent undersampling to acquire the individual signal components. In all multi-band techniques, it is necessary to estimate the non-ideal channel characteristics and equalize for them. The channel estimation technique can be either least mean square (LMS) error based (using a known signal waveform as probe signal)[23], or blind (without a known signal as the test waveform) [24]. In this thesis, the basic bandwidth interleaving technique will be extended to an incoherent undersampling-based framework to achieve frequency scalability in the incoherent undersampling-based test architecture beyond the front-end track-and-hold bandwidth. A probe signal based technique will be used for channel estimation and equalization.

To enable the fast adaptation of any new test technique, it is important to be able to estimate the observability of potential failure modes using a given test, in simulation. A brief survey of such available simulation frameworks is presented in the next subsection.

2.4 Model development and simulation framework

After a low-cost test instrumentation is developed, it needs to be evaluated for its efficiency, both for any limitations in resolution and accuracy with which a waveform can be captured, and for the effectiveness of the test strategy in detecting potential failures without marking good parts as faulty. This requires a simulation flow with the capability to assess the impact of a given fault or extreme deviation in performance of a sub-module on the system's input-output behavior. While analog simulations at the transistor level can capture these effects, performing a full blown analog simulation for a large system is not feasible. Not only can the number of faults or process variation effects that need to be simulated can be large, but it is also slow, costly, and computationally expensive to perform transistor-level simulations for the whole system. Given these restrictions, it is necessary to develop models and simulation flows for the components that can handle non-ideal waveforms at the input of the circuit-under-test in the presence of noise so that the transistor-level simulation can be limited only to the components in which the faults are introduced, otherwise, the model development is prohibitively costly.

Traditionally, linearized parametric behavioral models have been used to estimate the effects of process variation and catastrophic failures in large systems. However, linearized behavioral models are valid only under the assumption that the input to the subsystem does not deviate too much from the ideal. Hence, simple behavioral model-based impact analysis as proposed in literature [25, 26, 27, 28, 29, 30, 31, 32] is valid only for simple circuits and can not be applied to large systems. Significant improvement is achieved in capturing the non-linear effects in different circuit components with non-linear model order reduction approaches such as trajectory piecewise linear models and manifold based techniques [33, 34].

The non-linear models available in the literature are suitable for simulation of circuits under the assumption that the effect of the erroneous performance of an upstream block in the signal-flow chain can be captured or translated through simplified models. One situation where such an approach fails, is any situation where the distorted waveform due to

erroneous behavior acts as an input to a latch or track-and-hold amplifier, where the behavior crosses from a continuous-time to a discrete-time domain. While the digital parts of the circuits are easier to simulate in a discrete-time event-driven state space framework with probabilities assigned to each state transition in a Markov chain based simulation flow [35], the analog behavior is hard to parametrize. Hence, an end-to-end modeling and simulation flow is required to translate the non-ideal waveforms and given noise characteristics of the analog circuit components into state-transition probabilities for an event-driven simulation at the system level. Considerable effort has been spent building faithful models of latches, especially to capture dynamic transients in the metastable region. Most approaches have assumed simple linear feedback systems [36, 37], sometimes with enhancements, to capture the effects of parasitic loading effects [38]. Detailed non-linear theoretical analysis was presented in [39], but the proposed model is too complex for practical use. A more practical solution for capturing the non-linear behavior due to large-signal conditions was proposed in [40].

However, all these models neglected the effect of noise. Noise characterization in a latch is difficult due to the large non-linearity involved and the multiple stable fixed points. Useful practical noise-aware latch models were proposed in [41, 42, 43], which considerably improved the ability to estimate the impact of the noise, but were unable to present a concrete flow to arrive at transition probabilities in presence of non-ideal input waveforms especially at the clock port. This research, attempts to bridge this gap by proposing a simulation flow using the basic stochastic dynamic equation framework proposed in [44], which can be used to estimate latch transition probabilities in the presence of noise and distorted input waveforms.

CHAPTER 3

INCOHERENT UNDER-SAMPLING BASED WAVEFORM ACQUISITION

3.1 Introduction

Incoherent under-sampling is a robust and cost effective method of periodic waveform acquisition. The sampling clock need not be temporally coherent with the waveform time base and can be, in theory, arbitrarily slow compared to the signal period as long as enough samples are acquired and the frequency remains reasonably stable. The period of the signal waveform is extracted by back end algorithms. Most of the acquisition cost is shared by the front end track and hold amplifier (THA) and the back end algorithm.

Previously, both time domain as well as frequency domain cost functions were used to estimate the period of the signal. However, due to the nature of the reconstruction technique and the high sensitivity to the accuracy of the estimated period, gradient descent based estimation technique is not applicable. Hence, it is important to reduce the computational effort required to evaluate the cost metric for period estimation due to large number of iteration and exhaustive search in estimating period. To reduce the computation cost and without sacrificing the accuracy of waveform period estimation with a given number of samples a time domain cost metric is proposed. This significantly reduces the computation cost per iteration as well as the number of data points required to achieve a given accuracy in waveform reconstruction.

Basic technique of incoherent under-sampling is reviewed in Sec 3.2 followed by a detailed discussion of the proposed signal reconstruction algorithm and associated cost function in Sec 3.3. Hardware validation measurements are discussed in Sec 3.5, followed by a summary of the main contributions.

3.2 Incoherent under-sampling and waveform reconstruction

The only unknown in reconstructing a periodic waveform from its samples is the period of the waveform. However in incoherent undersampling with periodic time base, the frequency components of the sample waveform are aliased and the period is unknown. Hence, the period needs to be estimated from the samples using the properties of the waveform. For periodic undersampling, the sampling period, T_s, is chosen in such a way that T_p/T_s is irrational. If T_s is chosen at random, this is satisfied with large probability. For a finite length representation of numbers a more correct statement is, T_p/T_s cannot be represented by using ratio of small integers. This ensures that the sampled data can be reordered to get an arbitrarily large effective sampling density on the periodic waveform and that the waveform is not aliased due to low effective sampling rate.

If the ratio of waveform period to sampling clock period is rational such that $\frac{T_p}{T_s} = \frac{m}{n}$ where m and n are small prime numbers then the effective sampling rate on the periodic waveform is limited to m which may cause aliasing. This is because $mT_s = nT_p$ and hence the k^{th} sample and $(k+m)^{th}$ sample are separated by integer multiple of waveform period and hence corresponds to the same phase on the periodic waveform. In general, to fully capture the effects such as rise time, fall time, jitter and distortion, the waveform needs to be acquired with high resolution and hence it is important that the effective sampling rate is large.

3.2.1 Phase remapping based reconstruction

To reduce the cost of acquisition it is desirable to be able to use $T_s << T_{s,nyq}$, where $T_{s,nyq}$ is the Nyquist sampling rate. This relaxes the conversion rate required of the digitizer and improves the accuracy of the conversion for better resolution. The reconstruction technique involves ordering the acquired samples according to its corresponding phase on the actual periodic waveform. More precisely, for a periodic function f,

$$\begin{aligned} f(t) &= f(t - nT_p) \text{ for } n \in \mathbb{Z} \\ \text{hence,} \quad f(nT_s) &= f(\tau_n) \text{ where, } \tau_n \equiv t \, mod(T_p) \end{aligned} \tag{3.1}$$

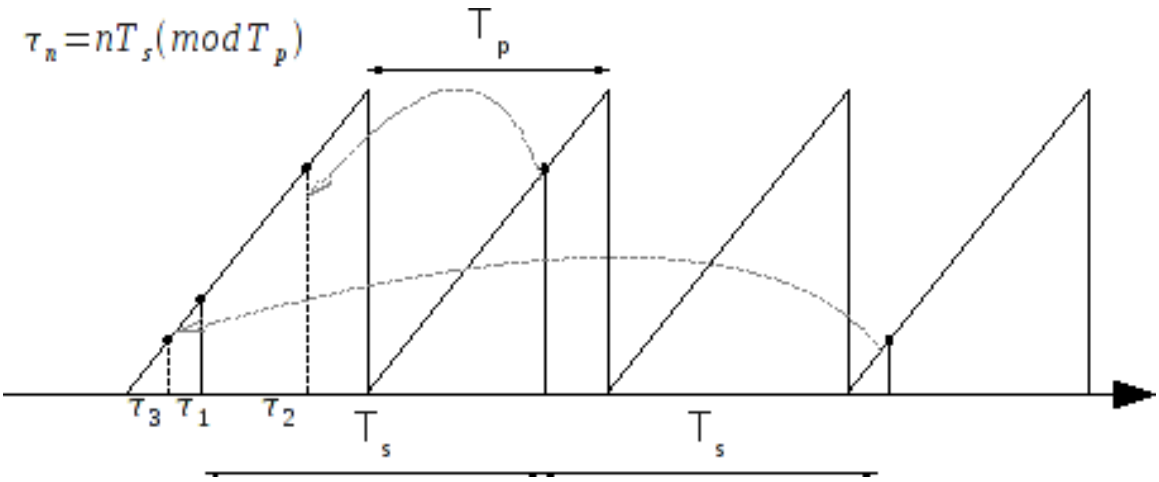

Figure 3.1: Phase remapping as used to reconstruct the waveform from incoherently sampled data by reordering the samples in ascending order of the phase of the sample in the original waveform

so by using the mapping,

$$\begin{pmatrix} f(nT_s) \\ nT_s \end{pmatrix} \longrightarrow \begin{pmatrix} f(\tau_n) \\ \tau_n \end{pmatrix} \tag{3.2}$$

it is possible to reconstruct the waveform. As mentioned before T_s/T_p not being rational, guarantees that $\tau_{n_1} \neq \tau_{n_2}$ whenever $n_1 \neq n_2$ and that $\{\tau_n\}$ are uniformly distributed on the interval $[0, T_p]$. The phase remapping concept is illustrated in Fig 3.1.

3.2.2 Period estimation

The period of the waveform needs to be known with high accuracy for using phase remapping. But, the exact value of T_p is not known in incoherent sampling. The period information is extracted from the acquired samples using the sparsity of the waveform. So a period $\tilde{T}_p$ is guessed and the phase remapping is done with $\tilde{T}_p$ in place of T_p. In absence of the prior knowledge of T_p some pre-defined cost function is minimized to find the best $\tilde{T}_p$.

Usually, test waveforms are sparse in the sense that they have finite number of features. In [16], the cost metric used to estimate the period used the spectral sparsity of the signal by minimizing the l_1 norm of the discrete Fourier transform of the signal. While this acted as a fine estimation technique for the period, to reduce the search range an initial estimator was used based on interpolation of the FFT. The technique assumed that the fundamental

tones are dominant and that they can be identified from the other tones based on a ranking of the spectral peaks by power. Once the spectral spur corresponding to the fundamental is identified, the digital frequency can be estimated with high accuracy using an interpolation to locate the peak of the spectral spur. However, as can be seen from the simulated spectrum of the samples of a filtered 127-bit pseudo random bit sequence (PRBS) signal in Fig. 3.2, except in very few special case such dominant tone is not present and it is not easy to estimate the period from the spectrum. This is also evident from the power of the first 10 most dominant modes, after the dc component, as shown in the following array, where the dominant tones differ by less than a dB from the next higher spur:

$$\begin{pmatrix} 1 & 2 & 3 & 4 & 5 & 6 & 7 & 8 & 9 & 10 \\ 66.82 & 65.96 & 65.80 & 65.13 & 64.94 & 64.78 & 64.73 & 64.49 & 64.48 & 64.32 \end{pmatrix}$$

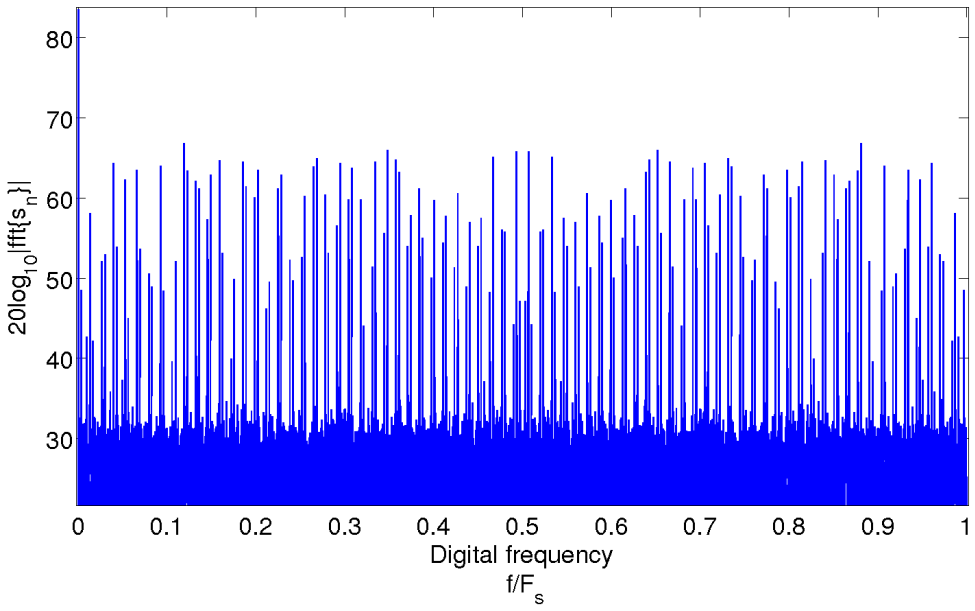

Figure 3.2: Spectrum of acquired samples by incoherently undersampling a 127-bit PRBS waveform

Hence, to avoid this problem of the absence of a dominant tone, it is assumed that the period of the signal is known approximately. I that case a search is performed to minimize the cost function around the approximate frequency. the search range is determined by the uncertainty range in the knowledge of the fundamental period of the signal. However, to

continue with the technique proposed in [16] one needs to estimate the spectrum in each iteration. Due to the large search range and fine resolution of estimation required it is necessary to reduce the computation effort per iteration. Total variation is an alternate measure of the sparsity of a given signal. It is widely used in the reconstruction of geophysical data. The total variation metric is given by:

$$C_{TV}(\tilde{T}_p) = \sum_i |s_i - s_{i-1}| \tag{3.3}$$

where s_i denotes the i_{th} sample after reconstruction with assumed period $\tilde{T}_p$. This significantly reduces the per iteration computation time to $O(N)$ from that using any spectral domain technique which has a $O(NlogN)$ computational effort to calculate fast Fourier transform (FFT).

The computational efficiency can be further improved by using a variant of the total variation where only a 1-bit approximation of the sample is used. The sample is approximated by its sign after removing the dc component of the signal. The proposed cost function measures the number of oscillations in the reconstructed waveform samples. For a wrong estimate of the period T_p, the mapping given in (3.2) causes a wrong ordering of the sample points in the reconstructed waveform causing an increase in the number of zero crossings of the signal. Since only the number of zero crossings are of interest, the signal is approximated by using two values (sign) and the computation involves 1-bits instead of full resolution values. The computation cost per iteration compares to calculating only the DC coefficient of the FFT. The technique thus gives an order $log\, N_s$ improvement in computational efficiency for same quality of reconstruction as with spectral domain techniques.

All data that falls between two pre-defined thresholds are rejected to reduce the effect of broadband noise leading to spurious zero crossings. The data after the threshold operation is represented as a two valued function with proper time stamps. After guessing a period $\tilde{T}_p$, and reconstructing the waveform using (3.2), the number of zero crossings in the reconstructed waveform are counted. For most wrong estimates of $\tilde{T}_p$ the number of zero

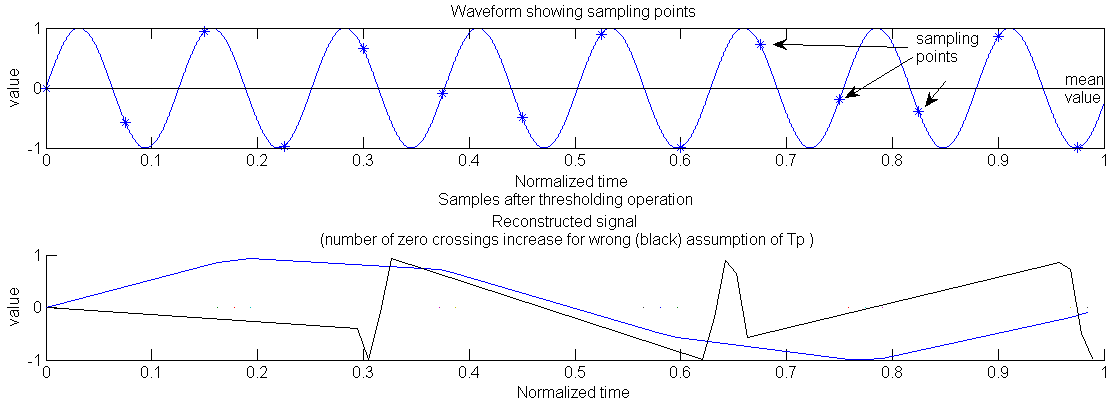

Figure 3.3: The original and sampled signal and subsequent increase in oscillation in the reconstructed waveform for wrong estimate of waveform period

crossings increase as illustrated in Fig 3.3. The assumption here is that the number of zero crossings cannot reduce in a reconstruction following (3.2), except for on extremely rare class of waveforms which we will discuss later. However, when the search is performed, there is aliasing over the whole range of $\tilde{T}_p$, i.e, there are multiple values of $\tilde{T}_p$ which creates a reconstruction with the minimum number of zero crossings. In fact all the aliased values of the fundamental period generate the same waveform or its time reversed (setting t to $-t$) equivalent. All the values of period have the same digital frequency $\tilde{F}_p \, mod \, F_s$, where F_s is the sampling frequency. These values depend on T_s and can be eliminated by using *two distinct sets of samples*, each with a different T_s. The only value of $\tilde{T}_p$ that gives a minimum number of zero crossings in both sets of data is T_p as illustrated in fig 3.4. If we assume that two different frequencies f_1 and f_2 match up in both samples acquired with sampling rates f_{s1} and f_{s2}, then we can write following the previous discussion:

$$f_1 = k_{11} f_{s1} + \phi_1 = k_{21} f_{s2} + \phi_2 \tag{3.4}$$

$$f_2 = k_{12} f_{s1} + \phi_1 = k_{22} f_{s2} + \phi_2$$

for some integers $k_{11}, k_{21}, k_{12}, k_{22}$. taking the difference of the two expressions we can write:

$$f_1 - f_2 = k_1 f_{s1} = k_2 f_{s2}$$

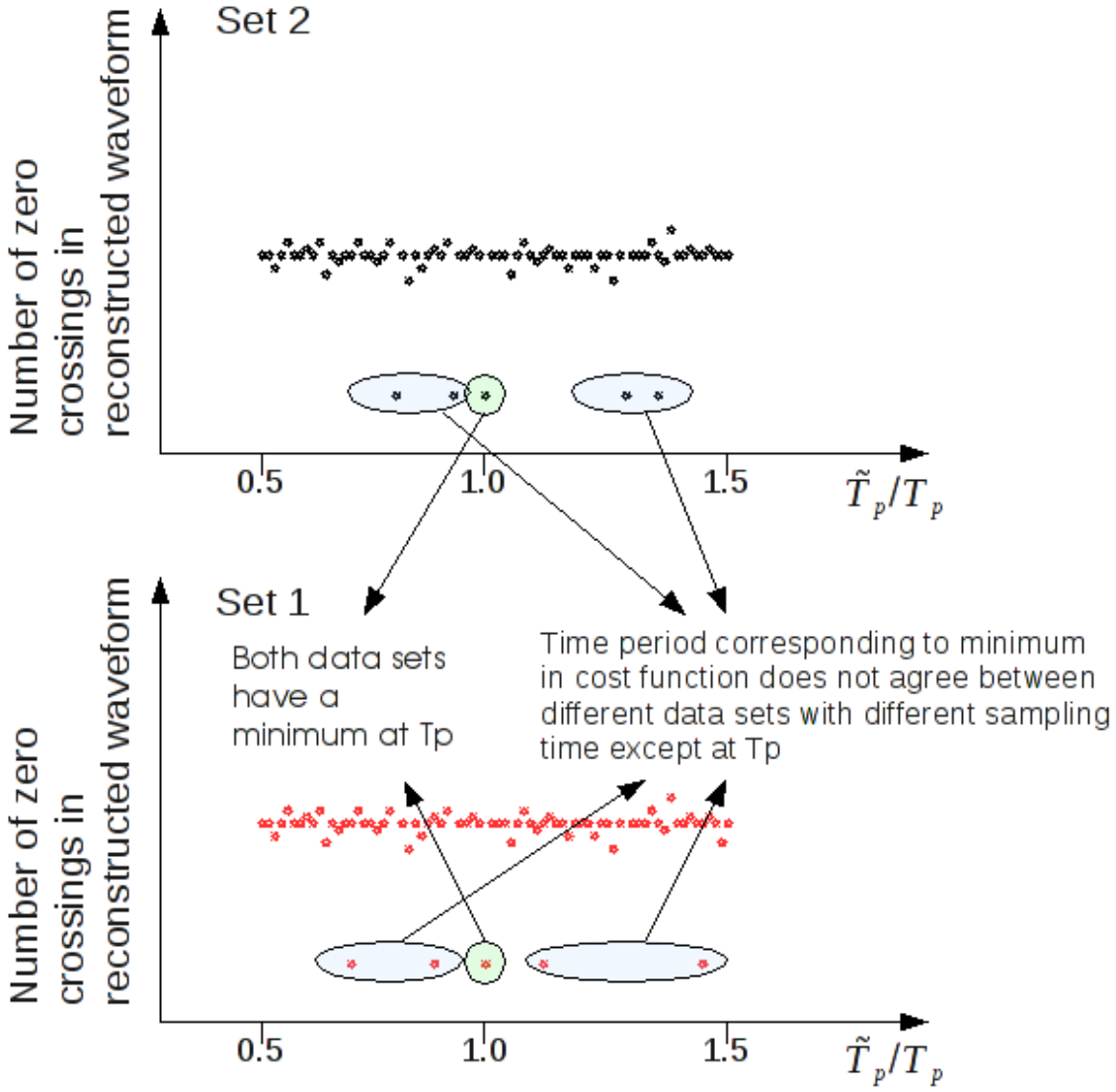

Figure 3.4: Aliasing with reconstruction process for two different sampling time

for some integers k_1 and k_2 or,

$$\frac{f_{s1}}{f_{s2}} = \frac{k_1}{k_2} \tag{3.5}$$

This gives an indication on the way the two sampling frequencies need to be chosen. Either they can be chosen such that $\frac{f_{s1}}{f_{s2}}$ is irrational and there are no two frequencies that are aliased since there is no solution to 3.5. Or such that the values of k_1 and k_2 is large so that $f_1 - f_2$ is large and both solutions are not in the search range.

Improving the estimate While the number of observed zero crossings is a good metric for estimating the fundamental period, in cases where the reconstructed data is used to extract timing noise, a better resolution may be required. A finer estimate of the waveform period can be obtained by searching for T_p at a higher resolution and minimizing against the residual error for a polynomial fitting of the signal around zero crossings. As illustrated in Fig 3.5, by defining thresholds around the zero crossing and grouping contiguous subset of samples that fall within the window, transition edges can be detected. Once the samples corresponding to each transition edge are identified, the mean (noise free) edge is estimated by using a polynomial regression fitting. The mean square deviation from the mean edge along the time axis then is a good measure of the accuracy of the period estimate. To accumulate information over the whole waveform the sum of mean square error for all the transition edges is minimized. The cost surface is locally convex and hence a gradient descent based technique can be used to estimate the best estimate of the period. The accuracy obtained by this secondary fine estimation is improved by an order over that from the zero crossing metric.

In light of the discussion we can express the reconstruction process concisely in the form of a flowchart as shown in Fig. 6.3.

3.3 Performance evaluation

In the previous section an intuitive reasoning was provided as a justification of the particular choice of cost function. However none of the non-idealities were considered. In this section the effects of noise, sampling clock jitter, sampling clock time base error, finite resolution of search space for T_p and possible aliasing of reconstructed waveform will be considered.

3.3.1 Resolution of the search space for $\tilde{T}_p$

A coarser resolution allows for faster computation time but has the potential danger of missing the optimal point due to granularity. The minimum resolution required for ensuring the optimal point is not missed is dependent on the number of sample points used and the under-sampling factor: $\eta_u = T_s/T_p$. It follows, that the minimum number of samples

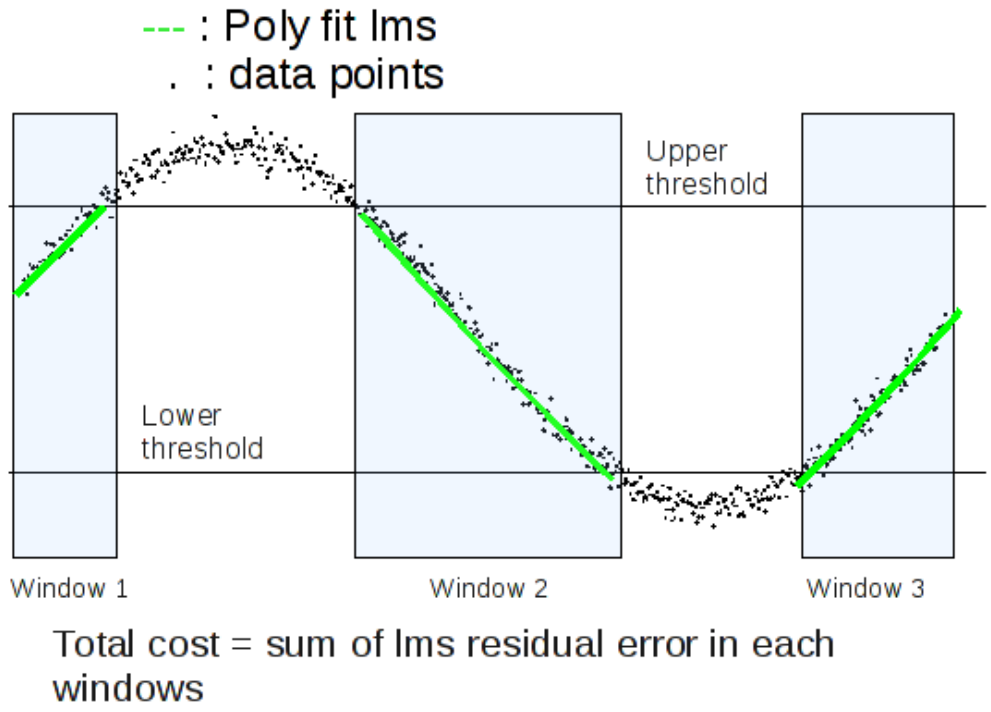

Figure 3.5: Cost metric used for fine reconstruction

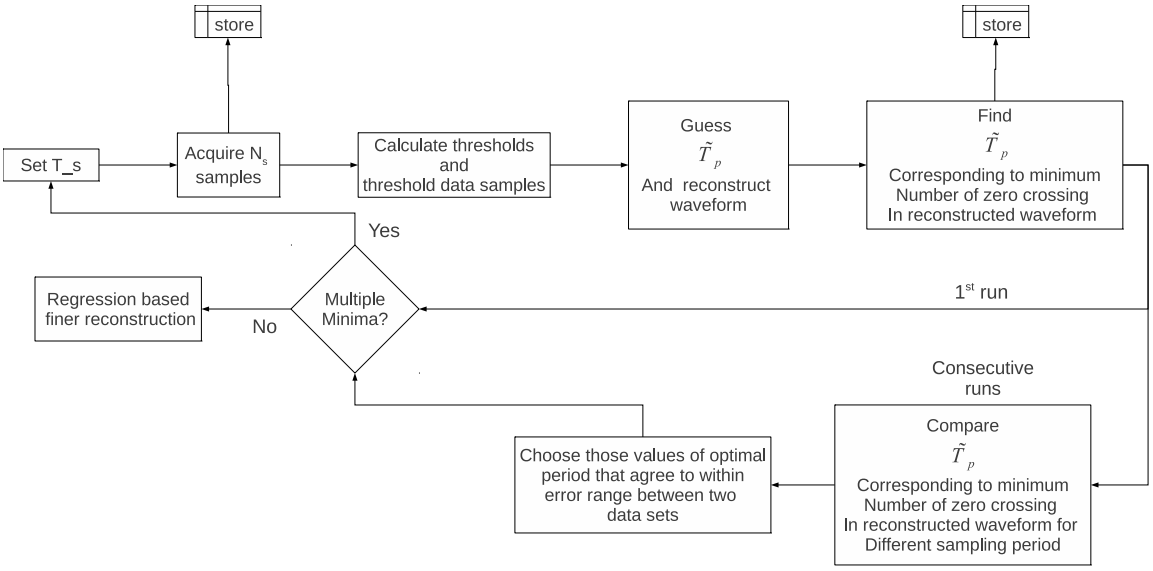

Figure 3.6: Flowchart showing the steps of reconstruction algorithm at coarse level

required should be much larger than twice the highest harmonic component present in the waveform such that there are enough points in the reconstructed signal to capture the waveform accurately. Under the assumption that enough samples are used to reconstruct the signal, the search resolution should obey the following relation:

$$\frac{|\mathrm{d}\tilde{T}_p|}{T_p} << \frac{1}{2N_s\eta_u} \tag{3.6}$$

3.3.2 Total number of operations

By selecting a resolution of an order of magnitude less than the right hand side of the inequality (3.6), i.e, a fractional resolution of $1/(20N_s\eta_u)$, the total number of search points assuming a 100% search range is given by:

$$N_{searchpoints} \approx 20N_s\eta_u$$

Since the number of zero crossings is calculated by taking difference of the modified data (through threshold operation), following which, the total number of operations per data set for a given choice of T_s is approximated by:

$$\begin{aligned} N_{calc} \approx & N_s(threshold) + 20N_s^2\eta_u(difference) \\ & + 20N_s^2\eta_u(modulocalculation) \end{aligned}$$

3.3.3 Signal noise and sampling jitter

Since the sampling clock provides the reference time base, an error in sampling clock frequency leads to an equal percentage error in the estimated frequency. This can lead to serious problems when the frequency error in the sampling clock varies independently over different sets of data. Appropriate margins should be considered for random errors in time base while choosing the correct frequency during reconstruction. The random component of sampling jitter causes the actual sampling instant to deviate from the ideal by a random τ_j, which translates to an equivalent additive noise component or an equivalent jitter in the reconstructed waveform. For a high signal to noise ratio (SNR), the total noise can be approximated as:

$$\nu_{tot} = \nu_{sampling\_jitter} + \nu_{additive}$$

If the noise components due to sampling jitter and due to additive noise are uncorrelated, the total noise power is the sum of the two. Noise in sampled data can cause spurious zero crossings to appear. To reduce the effect of the spurious zero crossings, all data inside the window defined by two threshold voltages are discarded. The threshold voltages are set at:

$$V_t = \mathcal{E}\{S_1, S_2, S_3, \ldots\} \pm 2\sqrt{\sigma_{v_{tot}}} \tag{3.7}$$

where $\mathcal{E}(\cdot)$ stands for average value. The samples are modified at the start as:

$$\tilde{S}_n = \begin{cases} 1 & \text{if } S_n > V_{ut} \\ 0 & \text{if } V_{lt} < S_n < V_{ut} \\ -1 & \text{if } S_n < V_{lt} \end{cases} \tag{3.8}$$

The samples which map to 0 according to (3.8), are not used for estimating T_p using zero crossings. However for finer reconstruction (by polynomial regression) and jitter characterization of the signal these values are included in the reconstruction and all the samples are used with their original value.

3.3.4 Tracking frequency drifts

In presence of frequency drift in the signal, the waveform period is ill defined and there is a limit to the maximum number of consequent samples that can be used to extract the period by this technique. The maximum number of samples that can be used to extract the period using zero crossing metric is given by n_{max} such that the accumulated phase deviation due to the frequency deviation from the ideal frequency , $f_{dev} = f - f_{ideal}$ is less than $T_b/2$, T_b being the bit period. The accumulated phase is given by:

$$\phi_{acc}(nT_s) = \int_0^{nT_s} f_{dev} \mathrm{d}t$$

If n_{max} given from this is less than the minimum number of samples that is required for the proper estimation of the fundamental period of the waveform then the technique fails with the given value of sampling rate and the sampling frequency needs to be increased. If however the deviation is small enough so that the period can be extracted from the samples,

then the frequency deviation can be tracked by using sliding window. For the j^{th} window defined by samples $s(iT_s)$ such that $n_{0,j} \leq i \leq n_{0,j} + n_{win} - 1$, the estimated frequency f_j is obtained as the mean frequency at the center of the window at $t = T_s(n_{0,j} + \frac{n_{win}-1}{2})$. And for each step the window can be translated by $(n_{win} - 1)/2$ samples such that $n_{0,j} = n_{0,j-1} + (n_{win} - 1)/2$. For each iteration the search range for period is chosen to be centered at the mean frequency of the last window, and the span is chosen to cover the maximum expected change in frequency over a time $T_S(n_{win} - 1)/2$.

By estimating the frequency drifts over the series of sliding windows a coarsely sampled estimation for the frequency drift is obtained which is interpolated and integrated to obtain a first order estimation of phase drift. After compensating for the coarse estimation of the phase drift, the residual phase due to resolution limit of the frequency estimation in each step, needs to be corrected. This is achieved by estimating the extra phase deviation required for each window to maximize the correlation of the reconstructed sample with that in the first window with the time axis normalized with respect to the period of each window. The extra phase drift obtained in this manner represent a higher order correction that can not be tracked through frequency tracking due to resolution limitation. After compensating for the phase drifts the samples from all the windows can be combined to obtain a high-resolution reconstruction of the waveform preserving the residual timing noise. While the phase compensation required for each window represent the low frequency drift component of the phase noise.

To verify the technique, in simulation, a low frequency drift with a triangular waveform was used to perturb the data clock in a filtered 127 bit PRBS waveform with peak to peak deviation of 5000 ppm along with a injected $1/f$ noise. The first order estimated frequency drift along with the ideal injected drift is shown in Fig. 3.7. The injected $1/f$ noise is shown in Fig. 3.8. The second order correction is shown in Fig. 3.9. The final compensated waveform reconstructed from 40000 samples is shown in Fig. 3.10

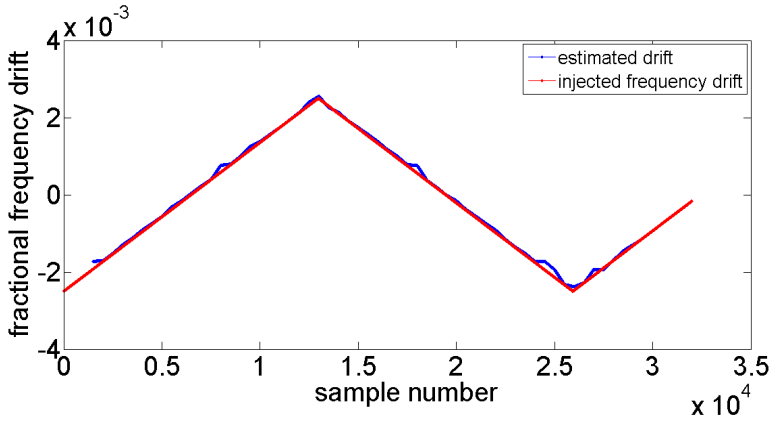

Figure 3.7: Ideal and first order estimate of injected frequency deviation

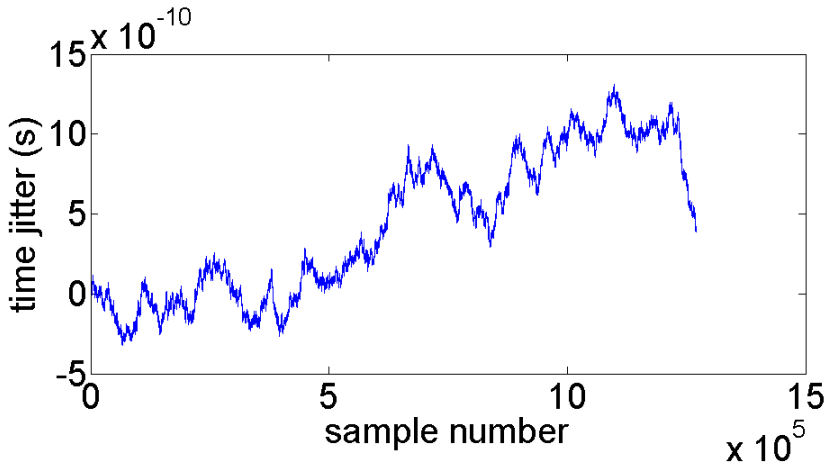

Figure 3.8: Injected $1/f$ noise

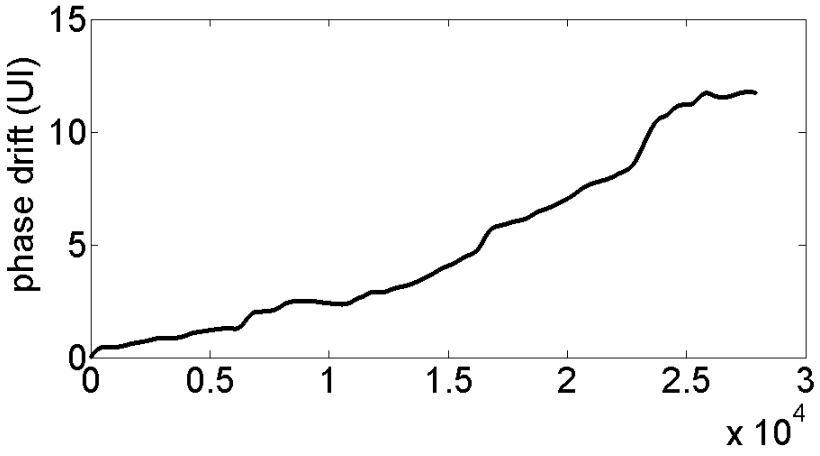

Figure 3.9: Higher order phase error estimation

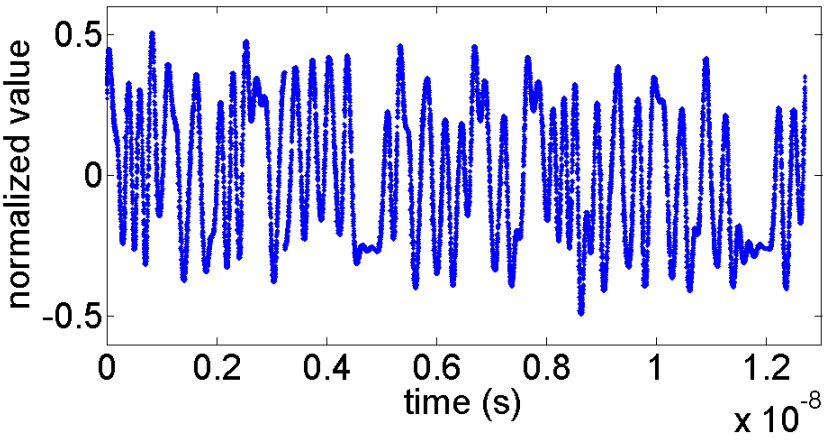

Figure 3.10: Clean waveform from 40000 samples after canceling the phase deviation error due to frequency drift

3.3.5 Waveforms for which zero crossing based estimation fails

Since the proposed zero crossing based metric uses only a sign approximation for the waveform (after removing the dc component), it loses a large amount of information about the signal waveform. For some waveforms this may change the fundamental period, that is, $Period\{f(t)\} \neq Period\{sign\,(f(t))\}$, $Period\{f(t)\}$ being the fundamental period of the waveform $f(t)$. An example waveform is shown in Fig. 3.11. Clearly the waveform period is 3

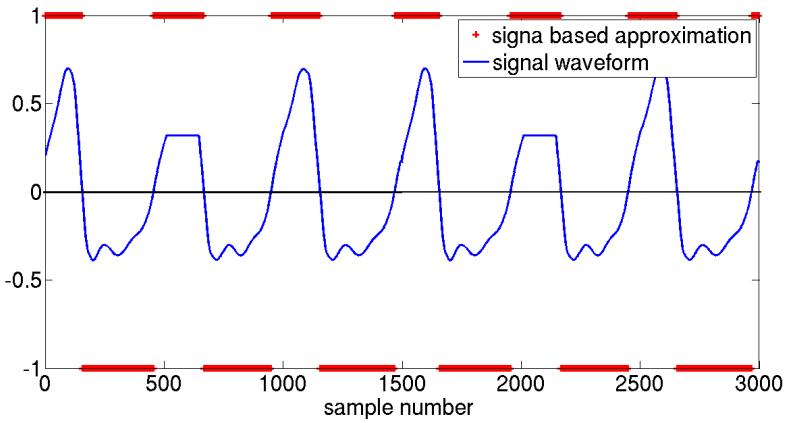

Figure 3.11: Example waveform for which 1-bit approximation changes the fundamental period. The waveform (blue) has fundamental period which is 3 times that of the corresponding 1-bit approximation

times that of the 1-bit sign approximation and the number of zero crossings is also more in the actual signal leading to a false estimate of period which is $1/3$ of the actual period

and hence the resultant waveform is not the actual waveform. The cost function plot is shown in Fig. 3.12. As expected the total variation metric is able to estimate the correct fundamental period (since there is no loss of information) while the zero crossing metric fails and instead the minima is equivalent to a fundamental period which is $1/3$ of the ideal period.

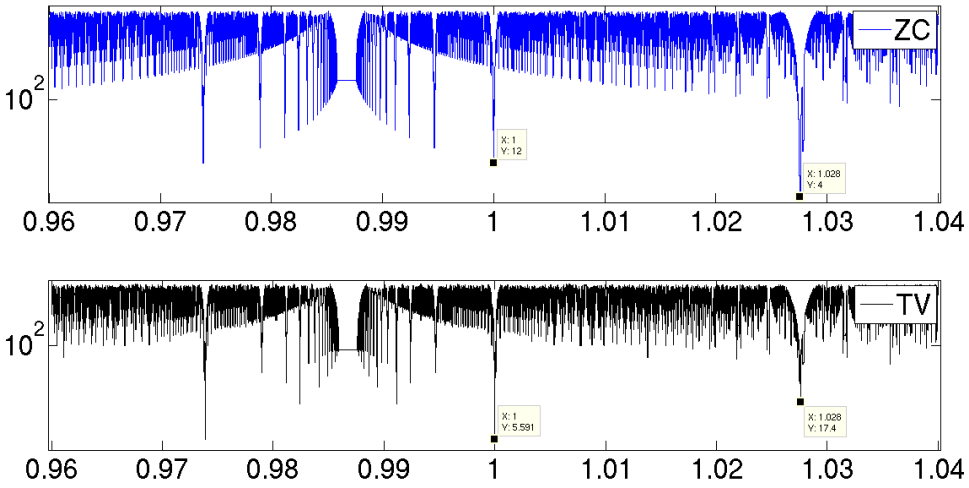

Figure 3.12: Cost plot vs normalized frequency for example waveform for which 1-bit approximation changes the fundamental period. The total variation cost detects the correct frequency while the zero crossing metric fails

3.4 Comparison with other cost metric

As mentioned in the previous section the zero crossing metric discards a large amount of information per sample. This improves the computation load but at the same time, can cause a loss of resolution or even false period estimation. To compare the computational efficiency gained the average run time for a 1% search range around the nominal fundamental period is plotted in Fig. 3.13 for the 3 cost metrics viz., L_1, total variation and zero crossing. All the other parameters including the search resolution are kept constant.

It is clear from Fig. 3.13, that for a given number of samples the zero crossing metric is significantly more efficient than the other two metrics. The minimum number of samples required to resolve the waveform period correctly is shown in Tab. 3.1. The resolving

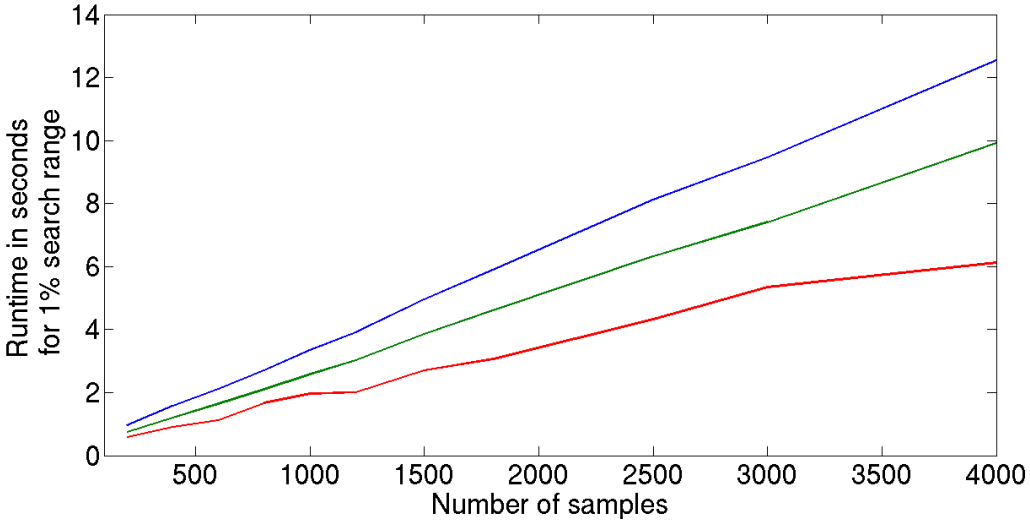

Figure 3.13: Average MATLAB run time of the L_1, total variation and zero crossing metrics with increasing number of samples showing computation load

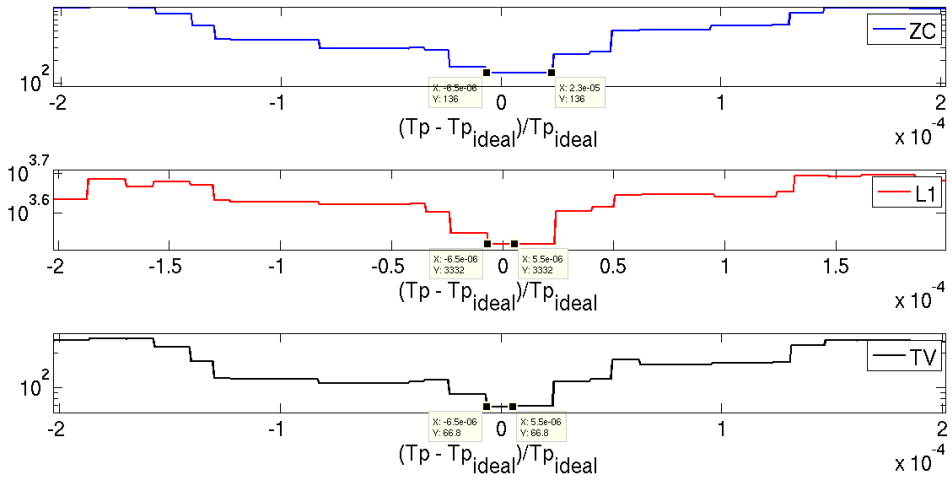

Figure 3.14: Resolution achieved from all three cost functions are comparable

power of the three metric is shown in Fig. 3.14. It is clear that the zero crossing metric compares well with the other metrics.

3.5 Hardware validation

The proposed algorithm was tested using two different signals generated by hardware. The signals consisted of a single tone, and PRBS.

The block diagram of the setup is shown in Fig 3.15. An IN1821TH (18 GHz, 2 GS/s)

Sampling jitter (synthesized color noise)	Data jitter (cumulative white noise)	Additive noise	Minimum number of samples		
			L_1	TV	ZC
0	0	0	260	280	280
0	0	-20dB	300	300	300
0	1 UI (over 1000 samples)	-20dB	500	500	500
0.23 UI	1 UI (over 1000 samples)	-20dB	1000	1100	1100
0.50 UI	1 UI (over 1000 samples)	-20dB	fails	fails	fails

Table 3.1: Minimum number of samples required to resolve the period of a spectrally rich waveform with varying SNR

track and hold amplifier was used as the front-end. The output of the track and hold amplifier was sampled using National Instruments data acquisition system (DAq) with bandwidth of 125 MHz.

3.5.1 Single tone signal

A 1.5 GHz tone was used as the test signal. The sampling frequencies used were chosen randomly and were set to approximately 83.41 MHz and 70.51 MHz respectively. Which is equivalent to an under-sampling factor of 17.98 and 21.27 respectively. 200 consecutive samples were used from each data sets for validating the algorithm.

The number of zero crossings vs the assumed waveform period is shown in Fig 3.16. The frequency estimation accuracy is 20 ppm. Afterwards, a fine reconstruction step was performed. The corresponding behavior of the cost function with respect to the assumed frequency is plotted in Fig. 3.17 around the coarse estimate at a resolution of 10 ppb. Both the coarse (blue) and the fine(red) reconstruction of the waveform are shown in Fig. 3.18.

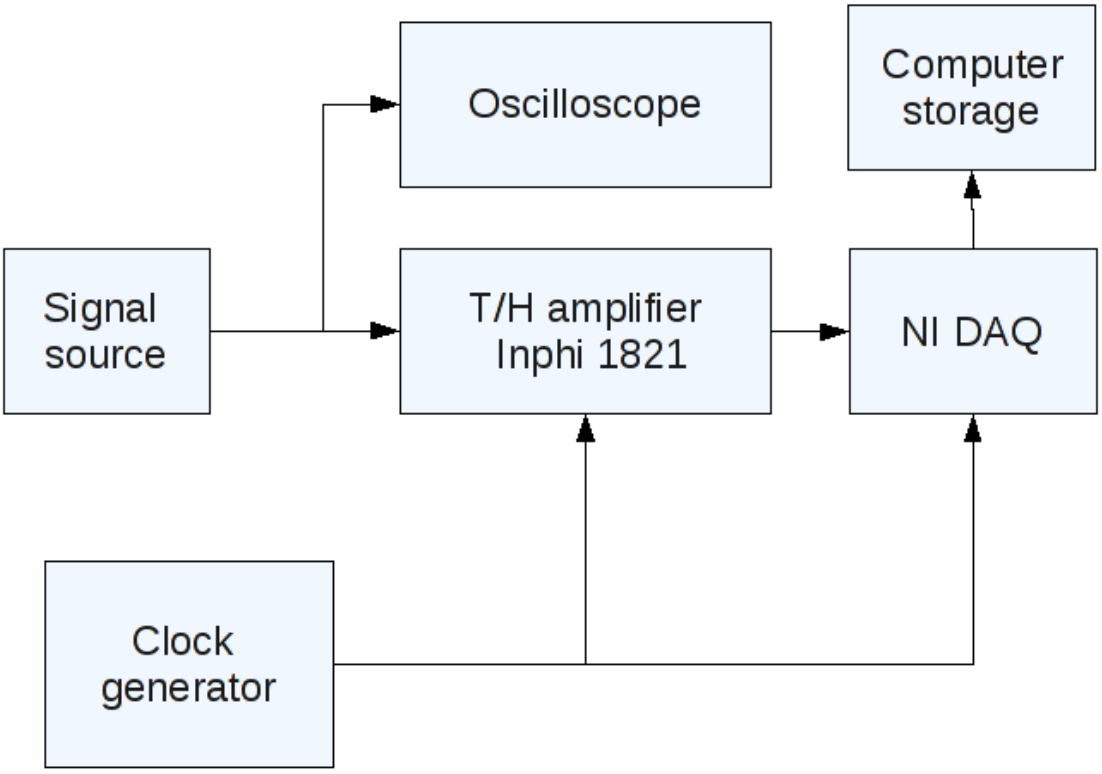

Figure 3.15: Hardware setup used for data acquisition

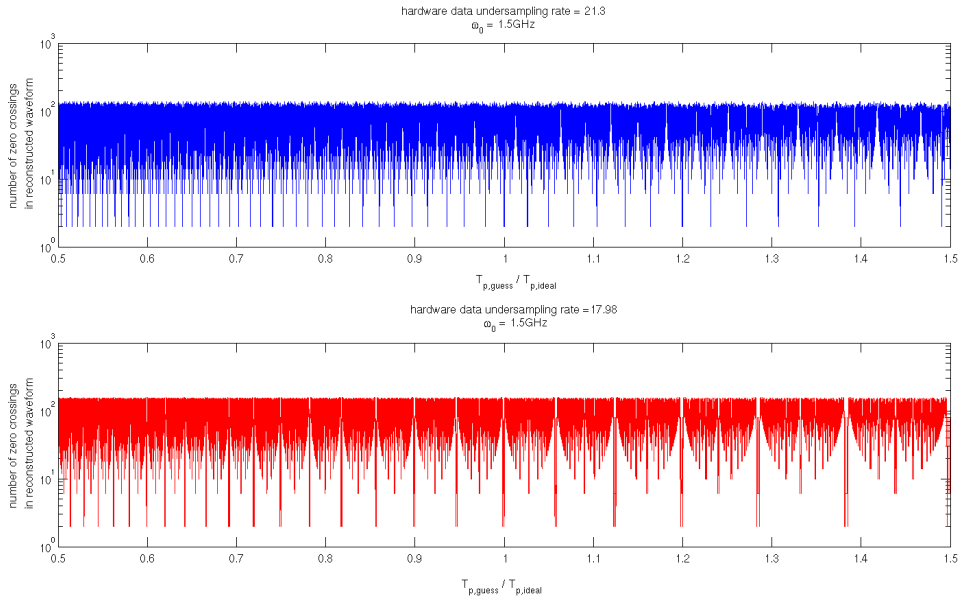

Figure 3.16: Number of zero crossing of reconstructed waveform vs assumed signal period

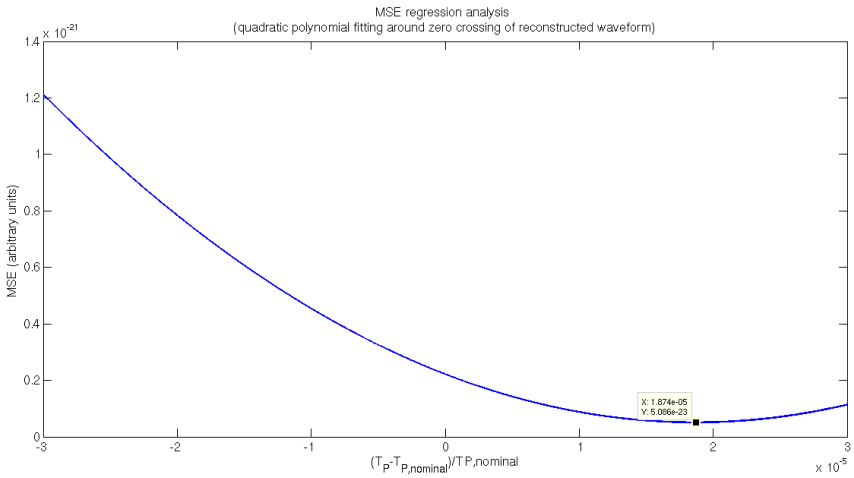

Figure 3.17: Residual LMS error for quadratic fit around zero crossings of reconstructed waveform vs assumed signal period

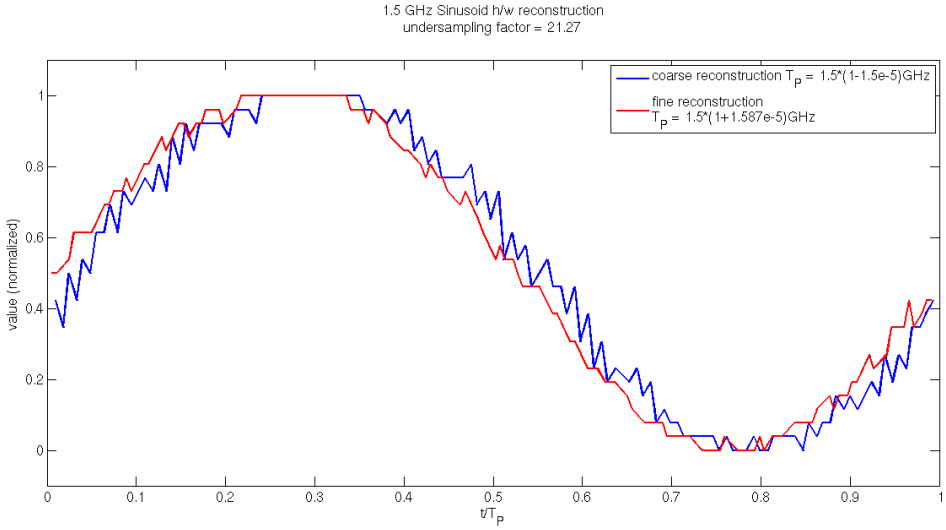

Figure 3.18: Reconstructed sinusoidal waveform from hardware acquired data 1.5 GHz sine wave 200 samples at 70.5 MHz coarse (blue) and fine (red) period estimation

3.5.2 Two tone signal (no fundamental frequency)

A two tone signal at 2 GHz and 2.5 GHz was used. The period is 500 MHz and there is no fundamental frequency present in the signal. The signal was sampled at 96.9 MHz and 99.6 MHz. The corresponding cost function plots are shown in Fig. 3.19 and fig 3.20. And the reconstructed waveform is shown in Fig. 3.21. The reconstructed waveform is shown in Fig 3.21.

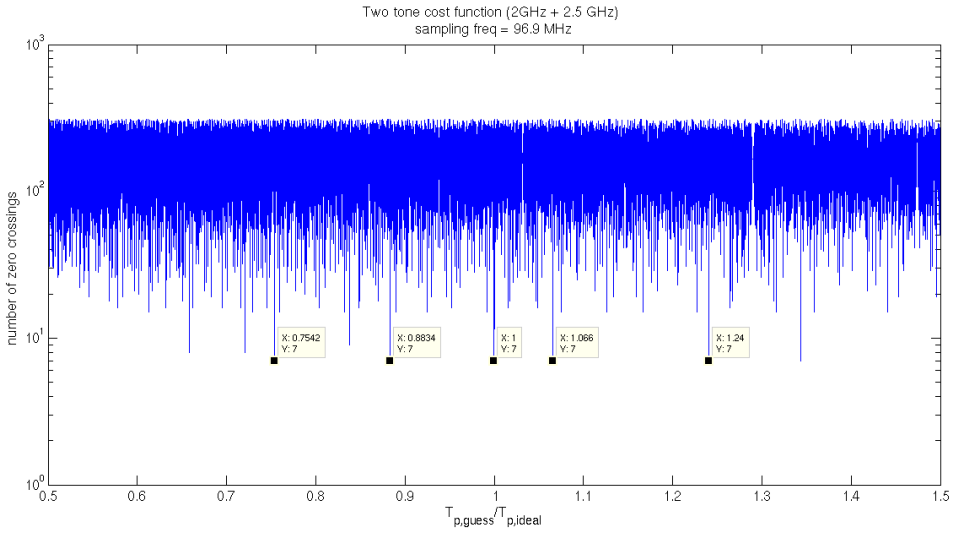

Figure 3.19: Two tone cost function 2GHz + 2.5GHz sampled at 96.9MHz 200 samples

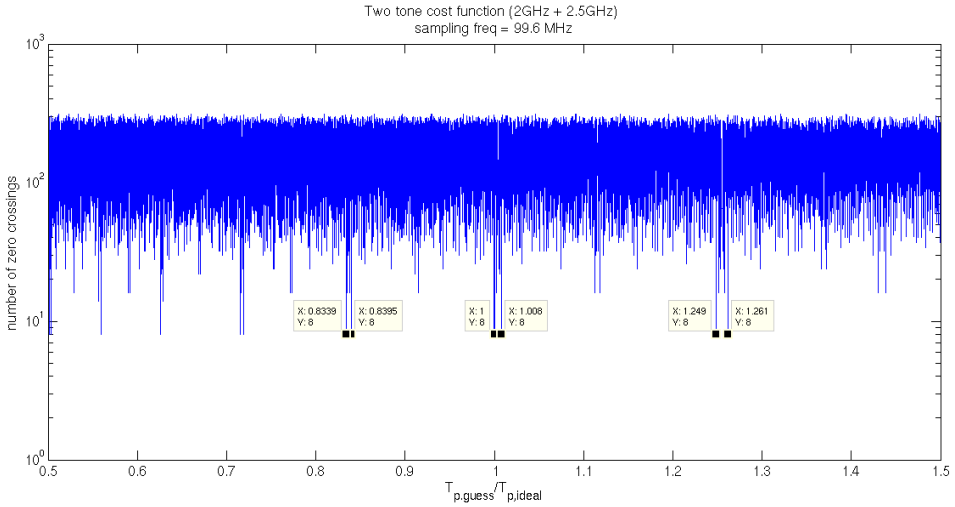

Figure 3.20: Two tone cost function 2GHz + 2.5GHz sampled at 99.6MHz 200 samples

3.5.3 PRBS signal

A $2^7 - 1$ prbs waveform at 3.5 Gbps was applied from a BERT source. The signal was sampled at 99.6 MHz and only 800 samples were used to estimate the waveform period. The plot of the cost function is shown in Fig. 3.22 and the corresponding reconstruction is shown in Fig. 3.23. The reconstructed signal eye is shown in Fig. 3.24.

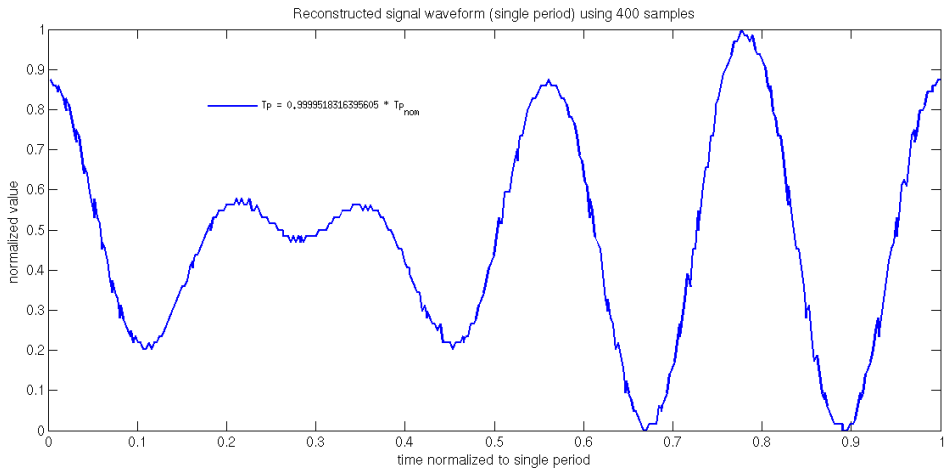

Figure 3.21: Two tone reconstructed waveform 2GHz + 2.5GHz sampled at 96.9MHz 400 samples

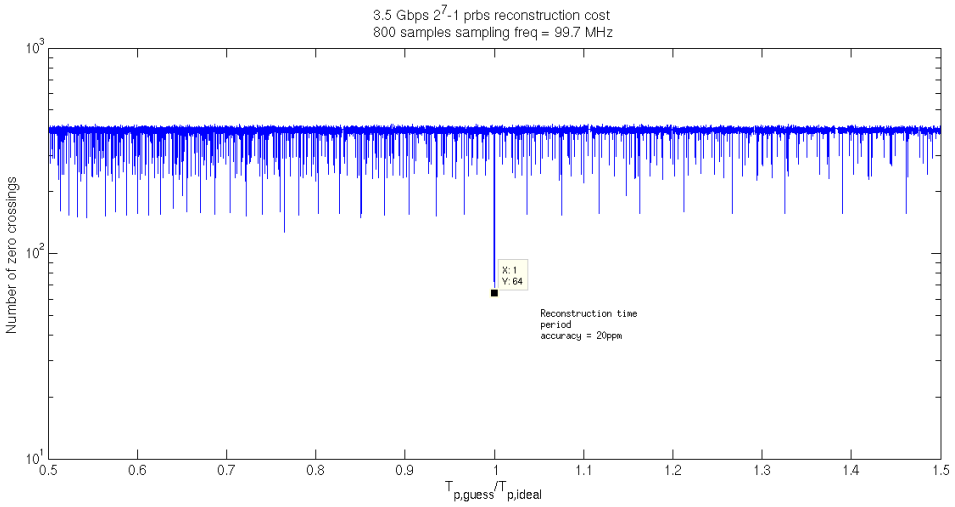

Figure 3.22: Cost function for 3.5Gbps PRBS sampled at 99.6MHz 800 samples

3.5.4 Tracking Frequency drift

for this experiment the track and hold amplifier was replaced by a Hittite track and hold with maximum sampling rate of 2 GHz and 18 GHz bandwidth. The sampling rate was chosen to be 987.654 MHz. The 10 MHz synchronizing reference input to the pattern generator was frequency modulated by 10 KHz. A 127 bit PRBS pattern was generated at 3.0 Gbps and 32000 samples were acquired. The ideal and the first order estimated frequency deviation is shown in Fig. 3.25. The second order correction in UI is shown in Fig. 3.26. The final reconstructed waveform after compensation using 32000 samples is

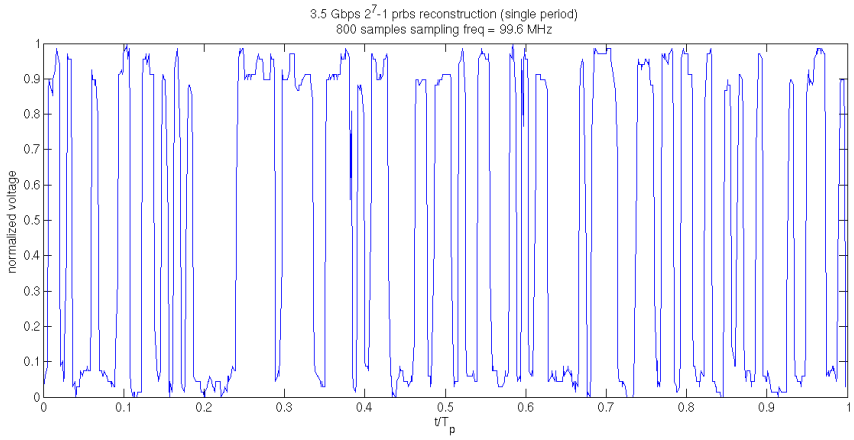

Figure 3.23: PRBS $2^7 - 1$ reconstructed waveform 3.5Gbps sampled at 96.9MHz 800 samples

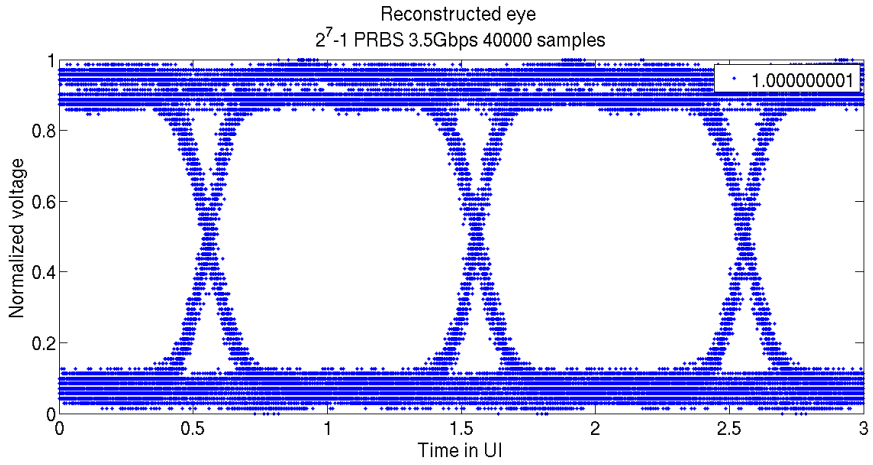

Figure 3.24: PRBS $2^7 - 1$ reconstructed eye 3.5Gbps sampled at 96.9MHz 40000 samples

shown in Fig. 3.27. As can be seen from the figures the technique can track and compensate the phase error in hardware data even though the frequency modulation is not as expected from the ideal triangular wave modulation of the reference.

3.6 Conclusions

The following are the main contributions in this part [45]:

- A time domain cost function for period estimation of incoherently under-sampled waveform
- Detailed analysis of the effects of non-ideal behavior of various components

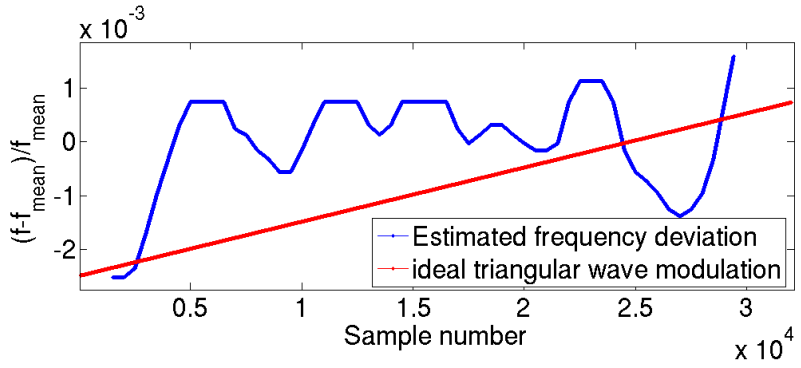

Figure 3.25: Ideal and first order estimate of injected frequency deviation

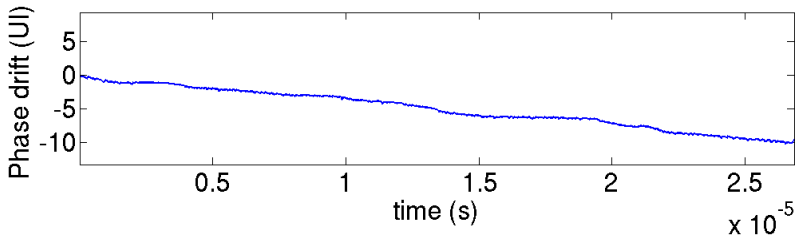

Figure 3.26: Higher order phase error estimation

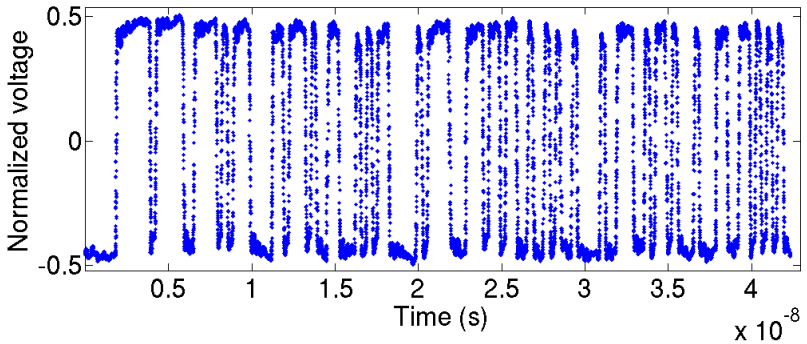

Figure 3.27: Clean waveform from 40000 samples after canceling the phase deviation error due to frequency drift

- Detailed analysis of the computation cost and the sample accuracy

The results are supported by detailed analysis and hardware results. Except for a few special cases it is found that the proposed cost function can detect fundamental period of signals with accuracy as good as spectral L_1 norm based or total variation based metric while at the same time being much more efficient in terms of the computational effort required to evaluate the cost function.

CHAPTER 4

INCOHERENT UNDERSAMPLING BASED LOW COST RF TESTING

4.1 Introduction

The general trend of radio-frequency communication systems moving to higher frequency bands poses a challenge of testing the transmitter devices with optimal cost and accuracy. While costly traditional test setups can provide static characterization of gain compression and amplitude to phase effects in devices using power sweeps, such measurements are often inadequate for decision making regarding the performance compliance in increasingly complex systems [46]. Dynamic measurements through base band testing using reference receiver to down convert the signal can provide more accurate results [47]. But the requirement of a golden receiver and the complexity of the test suite required to characterize bit error rates with enough confidence, hugely reduces the efficacy of such a test methodology. In absence of a reference receiver, it is usually hard to separate out the effects of the receiver non-idealities from that of the transmitter. As an alternate strategy, down-mixing-based parametric test methods [48] can extract the transmitter non ideality from the extracted modulation envelope. Besides suffering from the shortcoming of the requirement of a high-fidelity mixer, the down-conversion-based testing may not capture enough information about the transmitter. Fast and low-cost approaches to estimate the amplitude-to-amplitude and amplitude-to-phase distortion have been proposed [49, 50]. Other test strategies that have been proposed includes loop-back testing [51], or optimal test generation based on multi-tone testing using base-band processing in loop-back mode [52]. Indeed, with increasing speed and complexity a test strategy based on full waveform capture at high speed is more desirable. However due to the large analog to digital conversion rate required to enable digitization of the waveform using Nyquist rate sampling, undersampling is often employed to reduce the cost of the digitizer. One such popular strategy was described in [53], where using the periodicity of the high-frequency signal, the authors

reduced the conversion rate to enable transfer of waveform data through the low-bandwidth test port. But to ensure the periodicity, complex phase-locked loop based synchronization techniques were employed. This significantly adds to the cost and complexity of the test setup. Similar coherent undersampling-based test strategies were also reported in [54] for testing high power pulsed devices. In [55], a combination of coherent mixing and undersampling was used. However with the uncertainty of group delay and phase delay in the different signal paths in a practical test system it may not be always possible to control the phase precisely at every point in the test setup. To increase the efficiency of the test, the modulating test envelope is often optimized separately and may even be generated in a separate module either internal or external to the test system making it hard to synchronize various parts of the test system. As such it is desirable to have a test setup that can acquire high-speed narrow-band signals with free-running carrier and modulating envelope signals without any synchronization. Such a system greatly reduces both the cost and complexity of a tradition coherent undersampling-based setup without losing much in terms of accuracy due to more or less the same bottleneck as that of a coherent system in terms of the track-and-hold amplifier and digitizer non-linearity. In such a system, the modulated high-frequency signal is likely to be aperiodic due to the lack of a common period between the carrier and the modulating signal. In fact, the signal has two separate periods instead of one. In this work, a simple technique is proposed to separately estimate the envelope period and the carrier period and extract the high-frequency signal characteristics from incoherent undersampling (no synchronization between the source waveform and sampling clock) with free running carrier and envelope clocks. This allows one to extract the instantaneous dynamic non-linearity of the device under test (DUT) including memory effects. Such information can be used to reconstruct parametric models of any order or complexity from simple memory-less polynomial models to more complex memory models as proposed in literature [56, 57]. The major contributions of this work are:

- period estimation techniques for amplitude-modulated signal over a wide range of modulation index

- reconstruction of both amplitude and phase characteristics of amplitude-modulated signals
- fully incoherent setup with all three clocks (envelope, carrier and sampling) running free

The rest of the chapter is organized as follows: in section 4.2 a short motivation for the undersampling-based test setup is provided followed by a description of the modified reconstruction technique used in section 4.3. In section 4.4 hardware data is presented to prove the feasibility of the technique followed by a discussion of the accuracy limitations of the proposed setup in section 4.5. This will be followed by conclusions.

4.2 Incoherent undersampling based test setup

Dynamic testing of radio frequency (RF) components using amplitude modulated signal waveforms (with periodic envelope) can provide accurate estimation of device performance characteristics. Coherent undersampling is often employed to acquire these high speed test signal waveforms at the output of the RF device. With incorporation of more and more on-chip built in test features and higher level of system integration, the test envelope can be generated in a separate internal test generation module (within DUT) with low frequency clocks while, the reference carrier is generated from an independent phase locked loops (PLL). The internal clocks may not be accessible from outside for synchronization. Due to difficulty in phase synchronization at high speed, it is desirable to be able to reconstruct high speed amplitude modulated waveforms where the envelope signal, the carrier signal and the sampling clock are all free running. Standard incoherent undersampling based periodic signal acquisition techniques [16] can not be applied to a free running test signal, since the envelope and the carrier waveforms do not share a common period, and hence the modulated signal is not periodic. To reduce the cost and complexity of the test instrumentation for a transmitter device testing, a setup as shown in Fig. 4.1 is proposed. In such a setup the envelope, the carrier and the sampling clock are chosen to be free running with

respect to each other. Due to lack of periodicity of the modulated signal, a modified reconstruction technique is proposed. The signal waveform has two underlying periods (instead of a single period in a periodic signal), one for the envelope and one for the carrier. To reconstruct the signal waveform, it is necessary to estimate both the periodicity associated with the signal leading to a two step process of period estimation, one for estimating the envelope period and the other for the carrier period. The specific order in which the two periods are estimated depends on the modulation index of the AM signal. For low values of

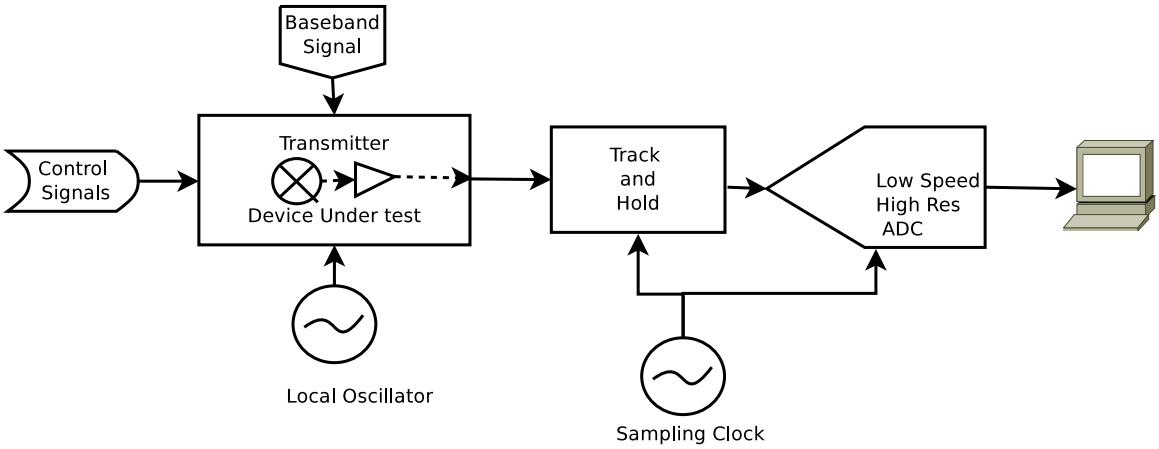

Figure 4.1: Schematic diagram of the proposed test setup for high speed RF components. The base-band signal, the carrier signal, and the sampling clock are allfree running

modulation index, the modulated signal waveform has the same sign as that of the instantaneous carrier. It is easier to identify the carrier period of the signal first followed by the envelope period using a sign based time domain metric (zero crossing metric). However, with high modulation index the carrier sign is not preserved in the modulated waveform and it is not possible to accurately identify the carrier period using phase remapping. But the envelope period can be estimated by using phase remapping (for a guess of the envelope period) and maximizing the peak power variation with envelope phase. After estimating the envelope period, the carrier period can be estimated from the samples corresponding to only a narrow range of envelope phase. This requires the phase and frequency of the carrier to be stable enough to keep the total accumulated jitter to a low value ($\ll T_P/2$, where, T_P is the carrier period). It must be mentioned here that the reconstruction method

proposed herein is different from that using bandpass sampling theorem [58], in the fact that the choice of sampling frequency is not strongly determined by the spectral support of the signal.

4.3 Reconstruction Technique

In this section the reconstruction technique for amplitude modulated signals is described. The process is summarized in a flowchart form in Fig. 4.2. However, to fully understand the challenges involved, the characteristics of a modulated signal are looked into in detail in the next subsection.

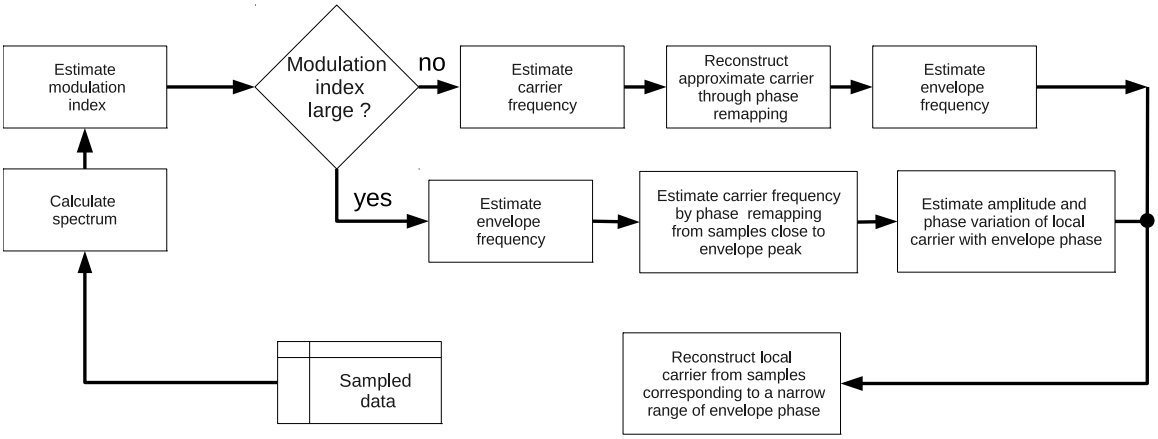

Figure 4.2: Flowchart for extracting envelope distortion parameters from extracted samples for AM signals

4.3.1 Characteristics of an amplitude modulated signal

An amplitude modulated signal $s_a(t)$ can be generally represented as,

$$s_a(t) = e(t)cos(\omega_c t) \tag{4.1}$$

where, $e(t)$ is the envelope signal and $cos(\omega_c t)$ represents a sinusoidal carrier signal with angular frequency ω_c. The spectrum $S_a(f)$ of the modulated signal $s_a(t)$ is given by,

$$S_a(f) = E(f - f_c) + E(f + f_c) \tag{4.2}$$

where $E(f \pm f_c)$ is a translation of the envelope spectrum. Now, if it is assumed that the envelope is periodic with a fundamental frequency f_e, the envelope spectrum is composed

of a collection of tones placed at the integer multiples of f_e and the modulated signal spectrum is given by its translation. It is worthwhile to notice here that for the modulated signal is periodic only when the the envelope and the carrier signals have a common period, i.e.,

$$s_a(t+T) = s_a(t) \iff e(t) = e(t+T) \text{ and } f_c T \in \mathbb{Z} \tag{4.3}$$

In this work it is assumed that the envelope and carrier are free-running and do not share a common period. So that the modulated signal is not periodic. Also both the carrier and the envelope frequencies are unknown. The envelope signal may or may not have a non-zero average depending upon whether the modulation scheme is a suppressed-carrier (no dc in envelope) or not. When the carrier is present, the modulation index, α, can be described as:

$$\alpha = [max\{e(t)\} - min\{e(t)\}]/2mean\{e(t)\} \tag{4.4}$$

without loss of generality, the dc component can be taken to be 1 and for simplicity it will be assumed the envelope to be sinusoidal i.e., $e(t) = 1+\alpha cos(\omega_e t)$. So that, for a modulating signal symmetric about dc, the envelope varies between $(1 \pm \alpha)$. For the case when α is less than 1, this implies, that the sign of the signal is same as the sign of the carrier. This allows one to easily estimate the carrier frequency with a high accuracy.

4.3.2 Envelope and carrier period estimation of signal with <100% modulation depth

Carrier frequency estimation As mentioned before, for an amplitude modulated signal with modulation index up to unity, the sign of the signal is same as the sign of the carrier. This implies that even though the signal overall is aperiodic, a one bit approximation involving only the sign of the signal is periodic with the same period as that of the carrier. Hence the carrier frequency can be estimated by using a zero-crossing based metric on the modulated signal reconstructed through phase remapping following [45]. The concept of phase remapping is shown schematically in Fig 4.3. The waveform is reconstructed by reordering the samples in ascending order of the modulo of the sampling time with respect to the assumed period. A wrong assumption of the period gives an erroneous ordering

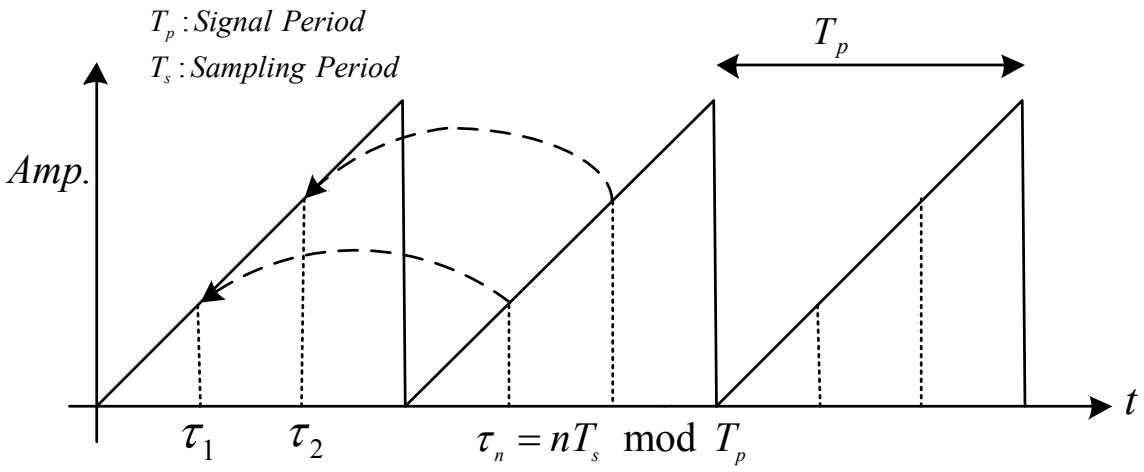

Figure 4.3: Phase remapping based reconstruction of periodic waveform

of samples having more number of zero crossing than the actual signal. Hence, the period of the waveform is given by that period which minimizes the number of zero crossings in the reconstructed waveform through phase remapping. After estimating the period of the carrier, a mean approximate waveform of the carrier can be estimated as described in the next subsection.

Approximate carrier reconstruction The best-fit reconstruction of the waveform is obtained by reordering the acquired samples through phase remapping technique with a period estimate from the last subsection. The resultant waveform is an overlap of multiple segments of the modulated signal with different amplitudes and possibly phases. To better illustrate the point,the result of folding the samples of the modulated signal into a single carrier period is shown in Fig 4.4a . When all the samples are included, the resultant waveform is a superposition of multiple sinusoids with different amplitude and phase. However if only the samples corresponding to a fixed phase of the envelope are included, the local carrier can be extracted as illustrated in Fig. 4.4b. However, to further proceed with the extraction of the local carrier or the instantaneous envelope, the envelope period needs to be estimated as described in next subsection.

Envelope period estimation To reconstruct the local carrier, the samples that corresponds to the same phase of the envelope need to be identified. But, to identify the envelope

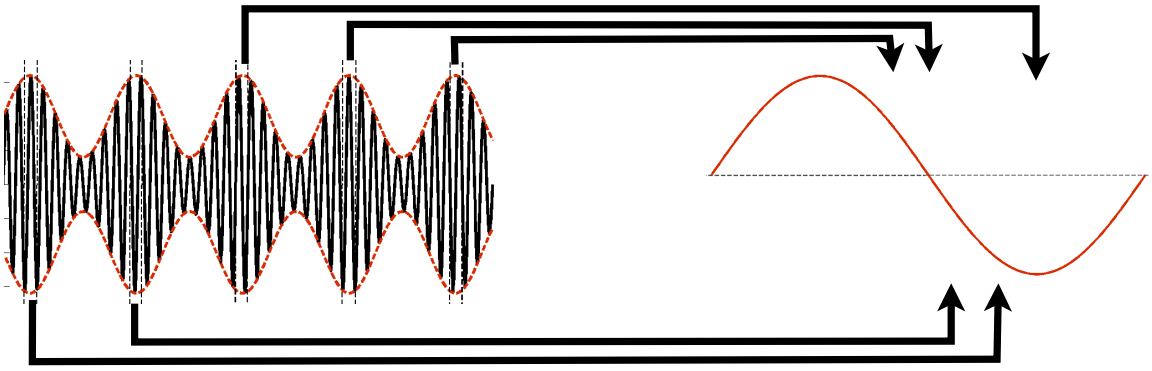

(a) Folding the modulated signal into one carrier period causes overlap of different sections of the signal waveform having different amplitude corresponding to different envelope phase

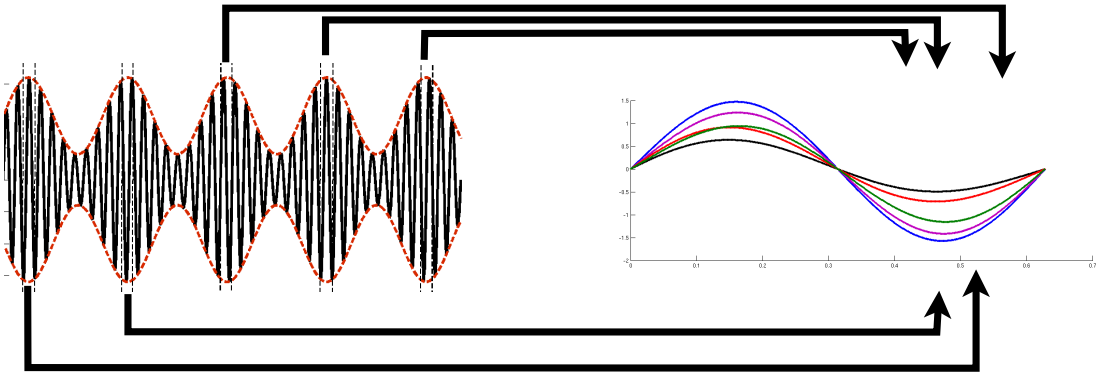

(b) Folding the modulated signal into one carrier period from sections with same envelope phase gives local carrier

Figure 4.4: Extracting carrier from different subset of samples

phase it is first necessary to identify the envelope period. To understand how this can be done, it is assumed that the signal is given by (4.1). Then the set of samples mapped to a narrow range of phase centered around the reference carrier phase ϕ_0 and width ϵ, is given

by,

$$\begin{aligned}\mathbb{S}^{\phi_0} = &\Big\{ e(nT_s)cos\Big(\frac{2\pi}{T_c}nT_s + \phi(e\,(nT_s)\,)\Big) \\ &\text{such that, } abs(2\pi\, mod(nT_s, T_c) - \phi_0) < \epsilon\Big\} \\ = &\Big\{ e(nT_s)cos\Big(\phi_0 + \phi(e\,(nT_s)\,)\Big) + \eta(nT_s) \\ &\text{such that, } abs(2\pi\, mod(nT_s, T_c) - \phi_0) < \epsilon \\ &\text{and, } \mathbb{E}\{\eta^2\} = O(\epsilon),\ \eta \text{ is a noise component}\Big\}\end{aligned} \tag{4.5}$$

where the phase component $\phi(e\,(nT_s)\,)$ represents the effects of amplitude to phase conversion and T_s is sampling period. If it is assumed that the carrier and the envelope signals are not related by a rational number and are free-running, the samples should be distributed uniformly across the full range ($[0, 2\pi]$) of the envelope phase. Now if the carrier period is divided into number of such small intervals, and in each interval the value of the carrier, $x_c(\phi_0)$, is approximated to be the expectation of all the sample values falling in that interval, the following relations are true,

$$x_c(\phi_0) = \mathbb{E}\{\mathbb{S}^{\phi_0}\} \tag{4.6}$$

which after simplifying gives,

$$\begin{aligned}x_c(\phi_0) = &\mathbb{E}\left\{e(nT_s)cos\Big(\phi(e(nT_s))\Big)\right\} cos(\phi_0) \\ &- \mathbb{E}\left\{e(nT_s)sin\Big(\phi(e(nT_s))\Big)\right\} sin(\phi_0)\end{aligned} \tag{4.7}$$

or,

$$x_c(\phi_0) = Acos(\phi_0 + \phi_e) \tag{4.8}$$

where, A and ϕ_e are independent of ϕ_0. If the actual sample values in a given carrier phase interval is divided by the estimated mean carrier and create a new map as,

$$y_{\phi_0}(nT_s) := s_a(nT_s)/x_c(\phi_0) \tag{4.9}$$

where n is chosen such that the sample corresponds to the given interval centered at ϕ_0

$$\text{or, } y_{\phi_0}(nT_s) = e(nT_s)\left(\frac{cos(\phi_0)}{Acos(\phi_0 + \phi_e)}\right) \tag{4.10}$$

the new map extracts the envelope at a given set of sample points up to a constant scaling factor dependent on ϕ_0. It must be noted that to avoid noise amplification only intervals close to the carrier peak should be used. Now using this subset of samples, the period of the envelope can be easily extracted by using a simple Fourier transform and finding the peak. If however, the resultant envelope is under sampled, the envelope period can be estimated by using a zero-crossing-based algorithm similar to the carrier phase estimation. Once the envelope phase is known, the actual shape of the envelope and the amplitude to phase component can be easily extracted.

4.3.3 Envelope and carrier period estimation of >100% modulation depth

Envelope period estimation For estimating the envelope period directly at high modulation depth, phase remapping on to the envelope period is used. When the samples are rearranged by time folding in a single envelope period, the samples falling close by on the rescaled time, have the same envelope phase. When the estimated envelope period is wrong the samples corresponding to any given envelope phase is distributed uniformly across the whole envelope period. Thus for a correct guess of the envelope period the peak power variation with envelope phase due to amplitude modulation is preserved in the reconstructed waveform after phase remapping, but reduced for wrong assumptions of envelope period. This is conceptually shown in Fig. 4.5. Hence to identify the envelope period, the samples are folded using phase remapping onto a single time window of a guessed value of envelope period. The rescaled time (of a single period) is divided into many ($\approx$64) small intervals. In each such interval the peak value of the signal is observed. This sequence of maximum value of signal in each interval, gives the peak power variation with envelope phase. The correct guess of envelope period maximizes the range of variation in this sequence and minimizes the number of oscillations (zero crossings). This sequence also gives the absolute value of the envelope waveform when the period is guessed correctly. This is shown in a flowchart in Fig. 4.6.

There are multiple sources of false positives in the technique that need to be identified for successful estimation of envelope period. Some values of trial envelope period can

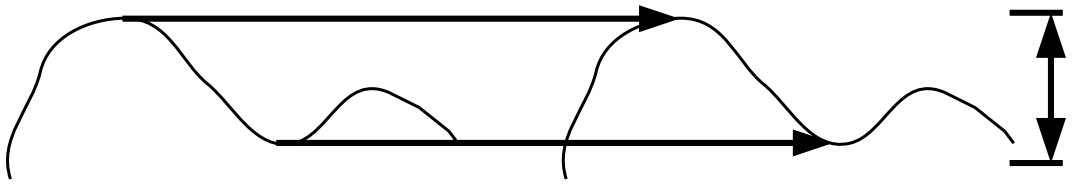

When points from peak are mapped only to peaks (correct estimate of envelope period), the range of variation is maximized

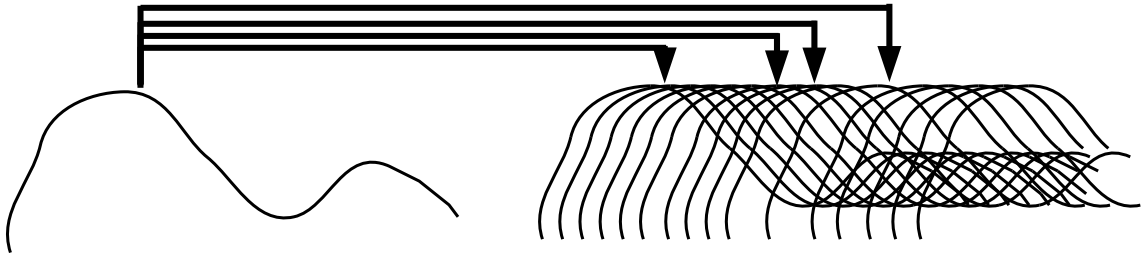

When points from peak are mapped everywhere (incorrect estimate of envelope period), the range of variation is less

Figure 4.5: Correct phase remapping maximizes the variation of peak power across different envelope phase

become coherent (ratio of sampling period to trial period is rational) with the sampling clock causing high variation of the envelope power. But in this case some of the phase intervals will have very few samples after phase remapping while others will have large number of samples, or all the samples in each phase interval will be clustered on the time axis. Hence, this kind of false positive can be eliminated by observing the variation of the number of samples in each of the intervals and the variation of the sampling phase (time) within each interval. Heuristically, a cost function for finding the correct envelope period (immune to chance coherent sampling) is obtained by dividing the peak variation range by a factor of the form $k_0 + n_{max} - n_{min}$, where, n_{max} and n_{min} are the maximum and the minimum of the number of samples falling within the different intervals respectively and k_0 is an appropriate constant chosen to reduce the scaling due to coherence with sampling time. A suitable choice for k_0 is half of the average number of samples in each interval for which the cost function takes the following form:

$$c(f) = \frac{\max_i\Big(\max(S_i)\Big) - \min_i(\max(S_i))}{(\frac{n_s}{2n_{int}} + \max_i(n_i) - \min_i(n_i))} \tag{4.11}$$

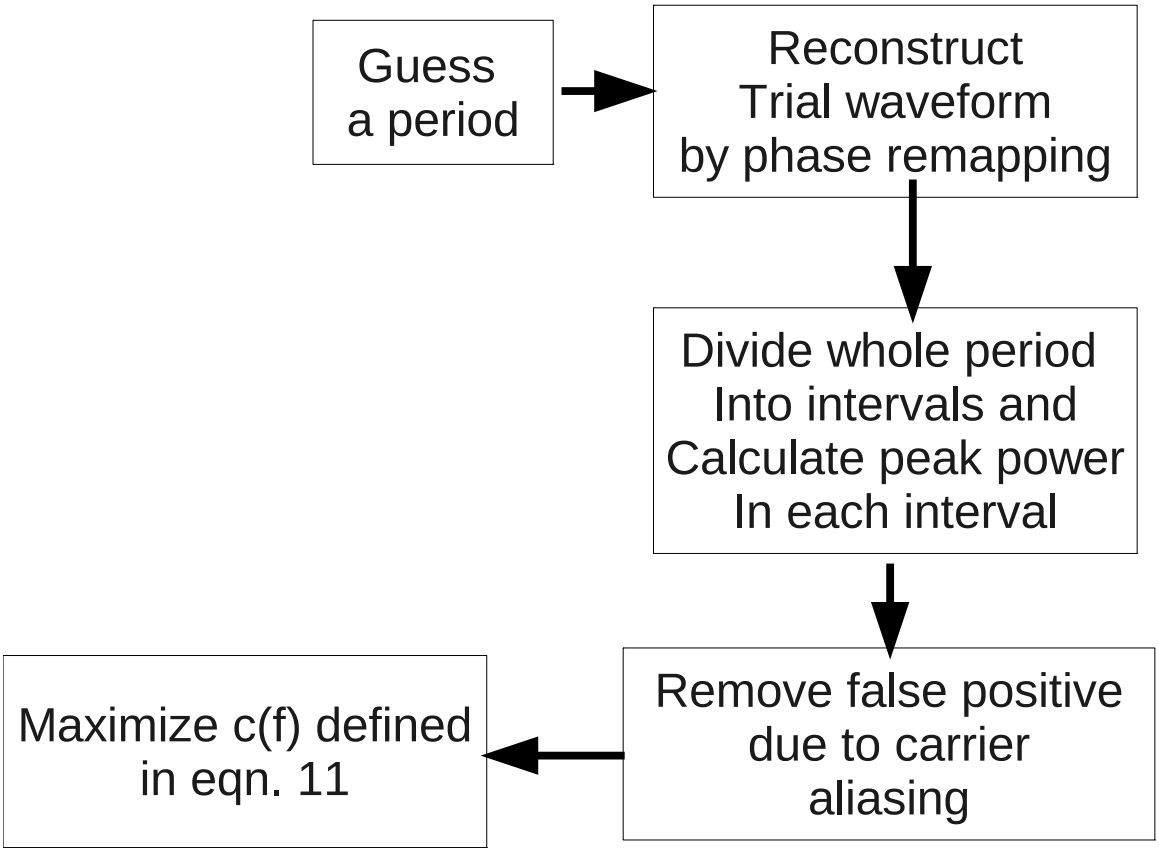

Figure 4.6: Flowchart showing the envelope period estimation for large modulation index. A search is performed over a range of frequencies where the period is expected to lie so that the cost function is maximized

S_i being the set of samples in the i^{th} interval, n_i the number of samples in the i^{th} interval, n_s the total number of samples and n_{int} is the number of intervals the unit period is divided into. It measures the range of power variation in each interval divided by the range of variation of the number of samples in each interval.

Another source of error is due to carrier aliasing. This is especially a problem when the signal has very low (<30%) depth of modulation. Since a low depth of modulation will have a low variation in the peak power of the signal over envelope phase, and in searching for the envelope period the power variation is maximized, the variation will show peaks for frequencies that are aliased version of carrier period or its rational multiples. This kind of false positives can be identified by observing the histogram of the signal within each interval of the rescaled time after phase remapping onto an envelope period. Since the

carrier synchronous folding with large variation will assign only small number of discrete carrier phases to each interval, with a small variation of power (due to small modulation depth), the histogram in each interval will show gaps. In the ideal case of correct envelope period the histogram in each interval cover all carrier phase uniformly and hence should, ideally, closely match the sinusoidal histogram. *Hence to avoid carrier aliasing, the trial values of envelope period for which the histogram (of sample values within the envelope phase interval) shows gaps are rejected as false positives.* However, identifying carrier aliasing based on the gaps in the histogram may fail as the modulation depth increases ($50\% < \alpha_m < 100\%$) because of the smearing across the gaps caused by amplitude modulation. Hence the modulation depth of the signal should be identified beforehand, from the spectrum of the raw samples before folding. Even in presence of aliasing due to undersampling, a signal with very low modulation index will show a single dominant peak corresponding to a strong carrier while the sidebands will occur in pairs (double sideband modulation). A signal with large modulation index will not have a dominant carrier tone in the spectrum. Based on the estimated modulation index the appropriate technique should be applied. Once the envelope period is identified, the next step involves the estimation of the carrier period.

Carrier period estimation For a signal with >100% depth of modulation, a direct application of phase remapping cannot recover the carrier period. This is due to the fact that the sign of the carrier flips periodically after modulation with varying envelope phase. However, after extracting the envelope period the sign changes due to the envelope phase can be removed. Once the envelope period is identified, the carrier period can be estimated using phase remapping and zero crossing metric, provided that the samples used for period estimation correspond to a narrow range of envelope phase centered around the peak of the envelope. This ensures that the carrier phase and amplitude is minimally affected by the envelope variation. However for a phase remapping technique to work, the phase of the carrier should be stable over the samples used in carrier recovery through phase remapping. This requires the carrier clock to be stable enough to limit the total accumulated time jitter

to a small value.

4.3.4 Extraction of local carrier amplitude and phase

After the estimation of both the carrier and the envelope periods the waveform features like amplitude and phase variation can be easily extracted by reconstructing the carrier at each and every point on the envelope. To extract the local carrier amplitude and phase corresponding to a specific envelope phase ψ_0, it needs to be ensured that the carrier is reconstructed only using those subset of samples which satisfy,

$$|mod(nT_s, T_e) * 2\pi - \psi_0| < \epsilon \tag{4.12}$$

where T_e is the estimated period of the envelope and 2ϵ is the width of the interval centered at envelope phase ψ_0. Once the required subset of samples are identified phase remapping is applied to one carrier period and reconstruct the carrier waveform. Afterwards, a sinusoid is fitted through the reordered samples. The amplitude and the phase of this best-fit sinusoid gives the local amplitude and phase of the modulated signal for a given phase ψ_0 of the envelope. From these two data one can easily extract the amplitude to amplitude and amplitude to phase distortion for the DUT by plotting the amplitude deviation from the ideal (sinusoidal) envelope and the phase deviation of the carrier across different envelope amplitude. Despite the fact that the technique mentioned here benefits from the lack of synchronization in the envelope and carrier signals, it has its own unique challenges as described in the next subsection.

4.3.5 Effect of free running carrier and envelope

In free running mode, an oscillator usually have poor frequency and phase stability. This can be important for the local oscillator clock providing the reference carrier. For a free running VCO, the accumulated jitter can be large (comparable to the carrier period), to an extent where the phase remapping technique fails. However if the phase varies slowly, there will be a maximum number of samples that can be used to reconstruct the signal waveform using phase remapping, limited by the total accumulated jitter. Additionally, since the resolution of the estimate of period is dependent on the number of samples used one might

need to increase the sampling frequency to acquire a given number of samples over a time window of length over which the accumulated phase error is within reasonable limits. This limits the minimum sampling frequency and hence the maximum undersampling ratio that can be used to acquire the signal.

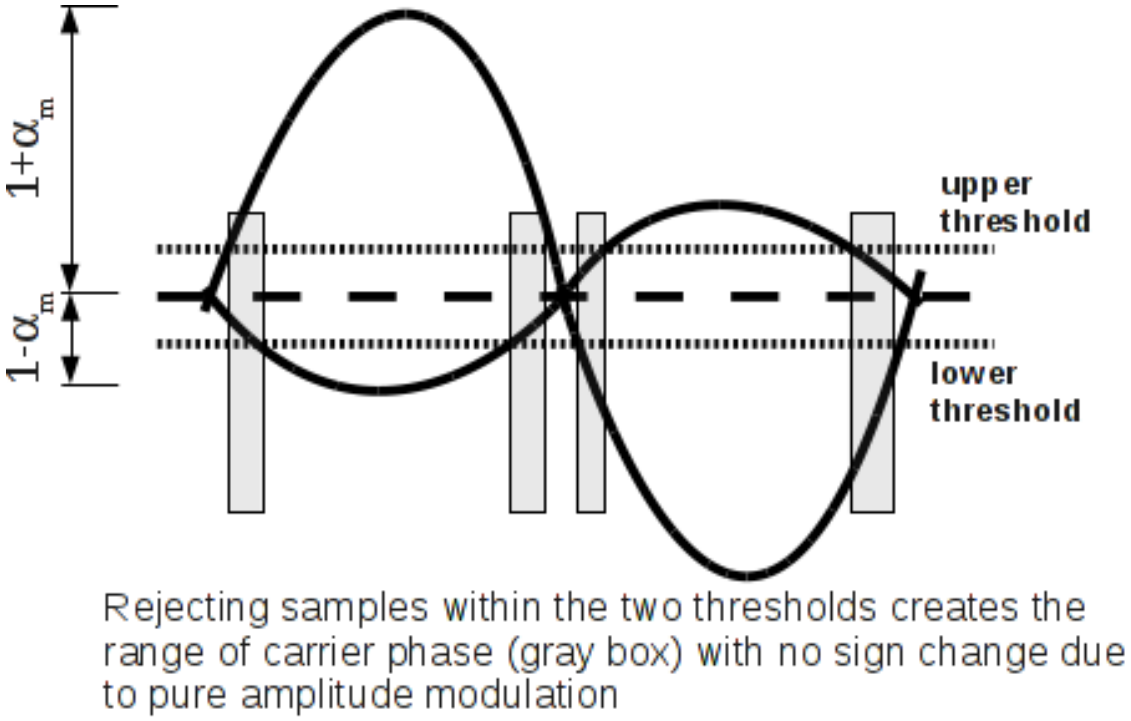

Figure 4.7: Removing samples around mean of the samples can increase the range of modulation index over which carrier period can be estimated by using phase remapping

4.3.6 Coverage of range of modulation index

The two techniques were evaluated for the range of modulation index over which they are valid ensuring an overlap between the two. So that waveforms can be reconstructed for a wide range of values of modulation index. For verifying in simulation, the signal is generated by multiplying a sinusoidal carrier with a periodic envelope. The envelope is generated by operating the sinusoid with a third order polynomial, $1+0.1x^2+0.01x^3$ to add nonlinearity and emulate amplitude-to-amplitude distortion. A small phase modulation, proportional to the envelope amplitude, is added to emulate amplitude to phase effects. Finally additive noise is added to the samples at -40 dBc. The modulation index is varied

form 0 to 2 in steps of 0.1 and for each case experiment is done with randomly chosen carrier and envelope frequencies. The experiment is considered successful if the carrier period and the envelope period is estimated correctly. Failure usually happens in the first step, i.e., carrier period extraction for technique 1 (<100%) and envelope period estimation for technique 2 (>100%). Also failure happens, if the envelope and carrier frequencies are rationally related. The results are collected in Table 4.1. There is an overlap between the two ranges for $0.7 < \alpha_m < 1.3$. Between the two techniques they can cover a large range of modulation index. The range for technique 1 can be increased further if the samples falling within a range of values around the mean of the signal are removed. Thus ensuring a range of carrier phase for which the samples have only one sign as shown in Fig. 4.7, and hence a zero crossing based algorithm can be used. However the range extension is not significant in presence of large amplitude to phase effect. The appropriate technique to be applied can be chosen by analyzing the aliased spectrum of the acquired samples. At low modulation depth there will be a single dominant carrier tone, while at higher modulation depth the carrier dominance will not be present since the sidebands typically appear in pairs in double sideband modulation.

Table 4.1: Range of modulation index covered by each technique

mod. index	tech. 1	tech. 2	mod. index	tech. 1	tech. 2
0.1	Y	N	1.1	Y	Y
0.2	Y	N	1.2	Y	Y
0.3	Y	N	1.3	Y	Y
0.4	Y	N	1.4	N	Y
0.5	Y	N	1.5	N	Y
0.6	Y	N	1.6	N	Y
0.7	Y	Y	1.7	N	Y
0.8	Y	Y	1.8	N	Y
0.9	Y	Y	1.9	N	Y
1.0	Y	Y	2.0	N	Y

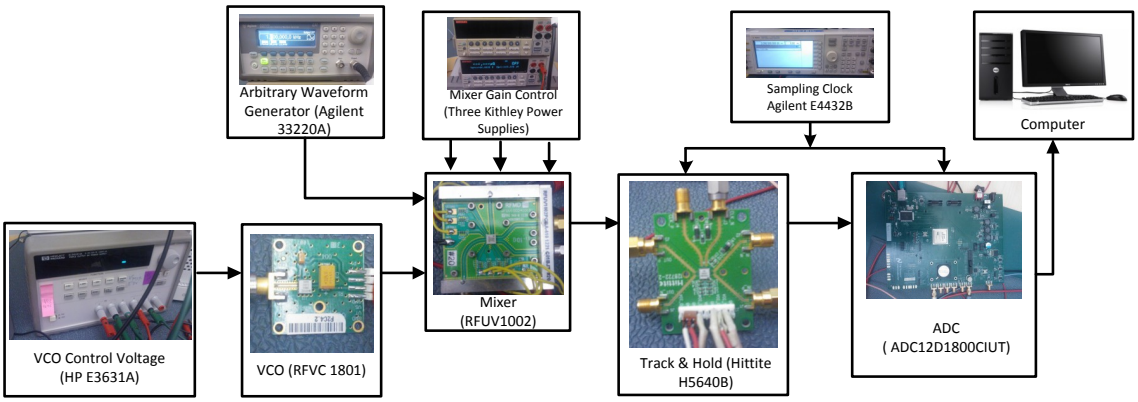

Figure 4.8: Description of Hardware Experimental Setup

4.4 Hardware Validation

The basic hardware setup is shown in Fig. 4.8. Three separate sources provide the sampling clock, carrier and the envelope signal. In the synchronous sampling case the sources are synchronized while for incoherent sampling they are used in the free running mode. The mixer DUT is a broadband mixer (RFUV1002) with local oscillator (LO) and RF bandwidth of 9GHz - 14GHz and inbuilt buffer amplifiers. The mixer LO is provided by a broadband voltage controlled oscillator (VCO) (RFVC 1801) operated in the free running mode. For the synchronous setup the carrier is provided by a signal generator. The VCO control is provided by a relatively stable DC supply. The modulating signal is provided by an arbitrary waveform generator (Agilent 33220A). The output of the mixer is sampled with a wide-band track-and-hold amplifier (Hittite H5640B) and digitized with a high-speed analog-to-digital converter board (ADC12D1800CUIT). The DUT has three inputs to control the gain and linearity of the mixer. Measurements were taken over a few different settings of the control inputs. The settings are varied to create a low gain mode, a high gain mode and an intermediate between the two. In the following subsection a validation for the reconstruction techniques is provided:

4.4.1 validation of reconstruction technique

modulation index <100% To extract the mean carrier of the signal the period of the signal is estimated using a zero-crossing metric and fold the signal into a window of single

carrier period. The carrier frequency is kept at approximately 10.67 GHz and modulated with a free running envelope at -20dBm and the DUT control setting at high gain mode. The result of folding 1000 consecutive samples and the extracted mean carrier is shown in Fig. 4.9. The spectrum of the corresponding extracted envelope is shown in Fig. 4.10.The extracted carrier amplitude and phase over the entire cycle of the envelope is shown in Fig. 4.11.

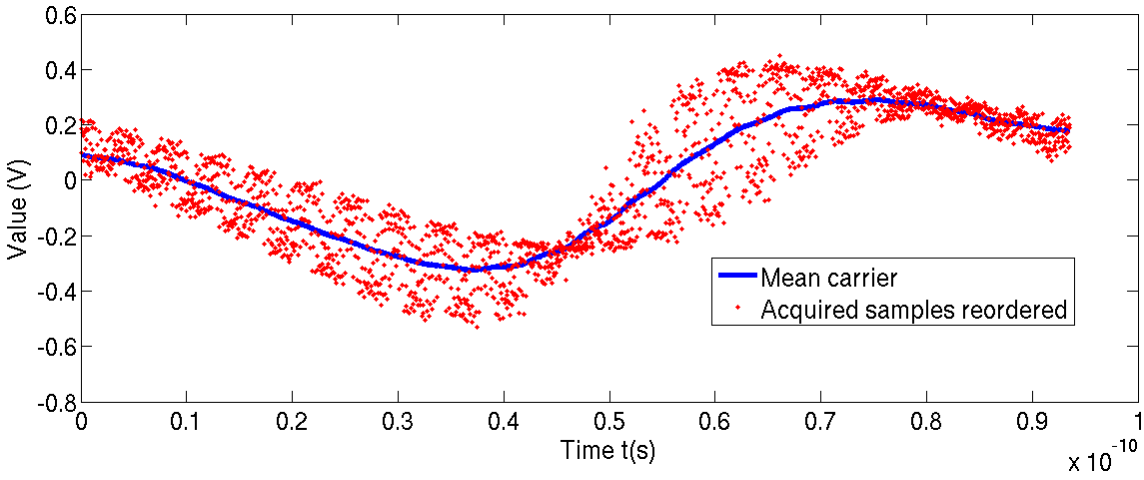

Figure 4.9: Samples reordered by phase remapping (red) and mean carrier (blue), $F_{c,ideal}$ = 10.67 GHz, Modulation freq = 20 MHz at -20 dBm sample rate of 829.889 MHz

modulation index >100% For validating the technique of period estimation and subsequent reconstruction, the test signal is generated with the DUT in high gain mode, carrier power at 0 dBm at a 13.3401 GHz and modulating signal at 20 MHz at -12 dBm. The sampling frequency is 887.889 MHz. Using 25000 samples the spectrum of the raw samples is shown in Fig. 4.12, near the peak, showing no dominant carrier tone and hence a large modulation index. The cost function plot for envelope period estimation using just 2000 samples is shown in Fig. 4.13. The peak is at 20 MHz. The extracted amplitude and phase of the local carrier is plotted with respect to the interval number (the envelope period is divided into 100 intervals) in Fig. 4.14. The change in sign of the carrier due to modulation with large modulation index appears as a π jump in the phase of the carrier.

synchronous sampling For validating the synchronous sampling setup, the carrier, the envelope and the sampling clocks are all synchronized. The DUT is kept at high gain

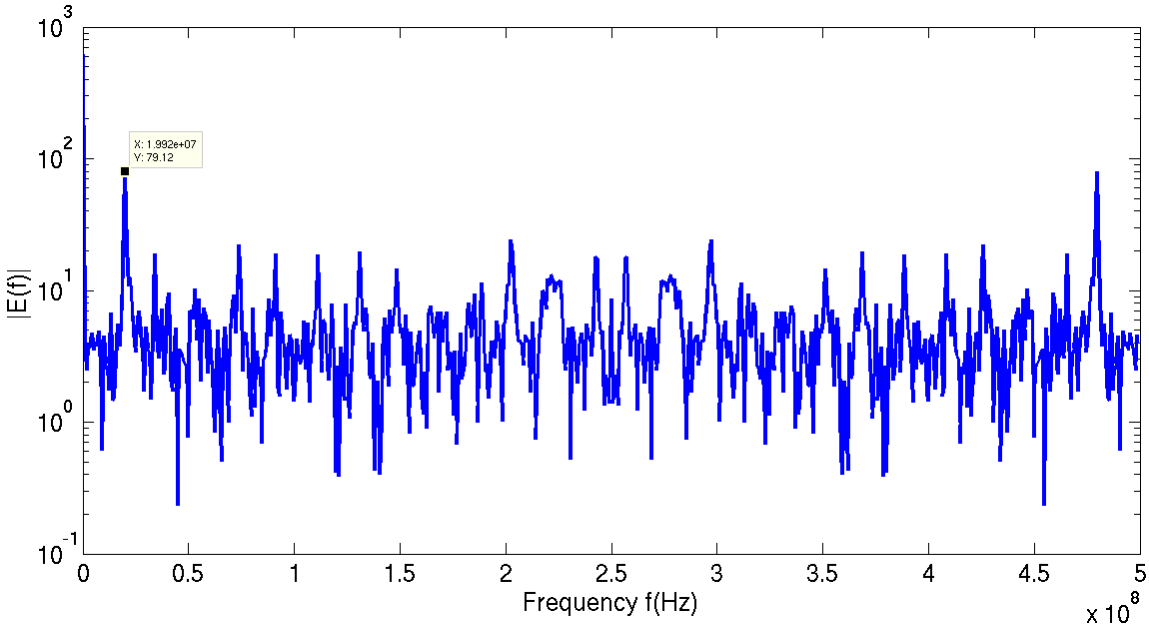

Figure 4.10: FFT of the ratio of the sample value to the mean carrier for a reference phase (peak) of the carrier showing a peak at 19.92 MHz (envelope frequency)

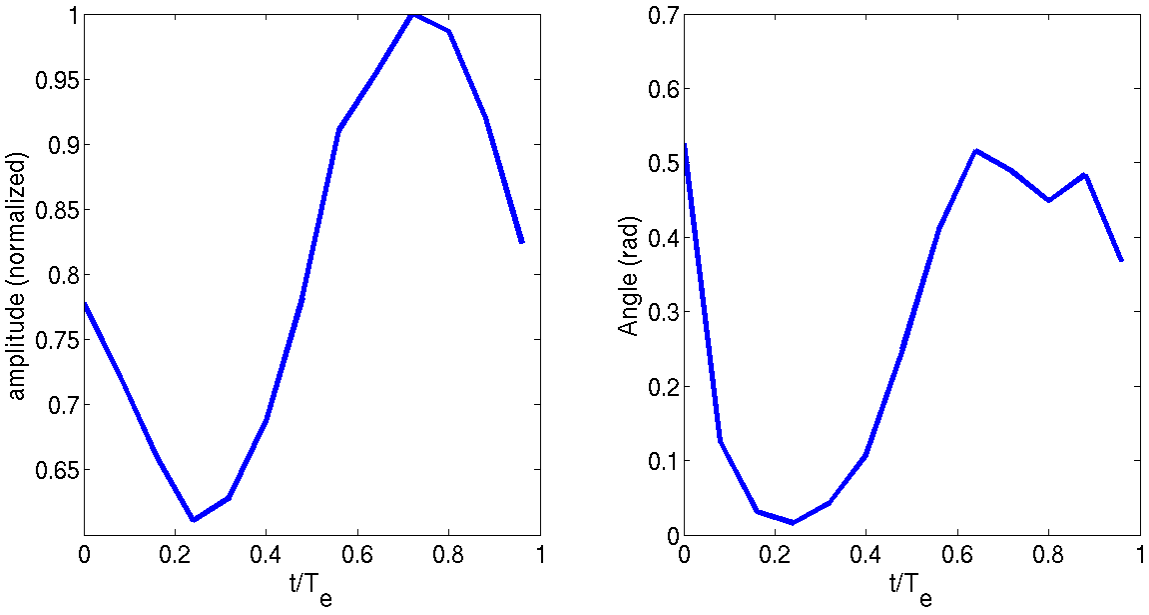

Figure 4.11: Amplitude (left) and Phase (right) of the reconstructed carrier for different phase of the envelope signal

mode. The carrier frequency is kept at 13 GHz, envelope frequency at 20 Mz, and the sampling clock at 1 GHz. The carrier power is at 0 dBm and the envelope power is kept at -12 dBm. The reconstructed envelope shape is shown in Fig.4.15. It must also be mentioned

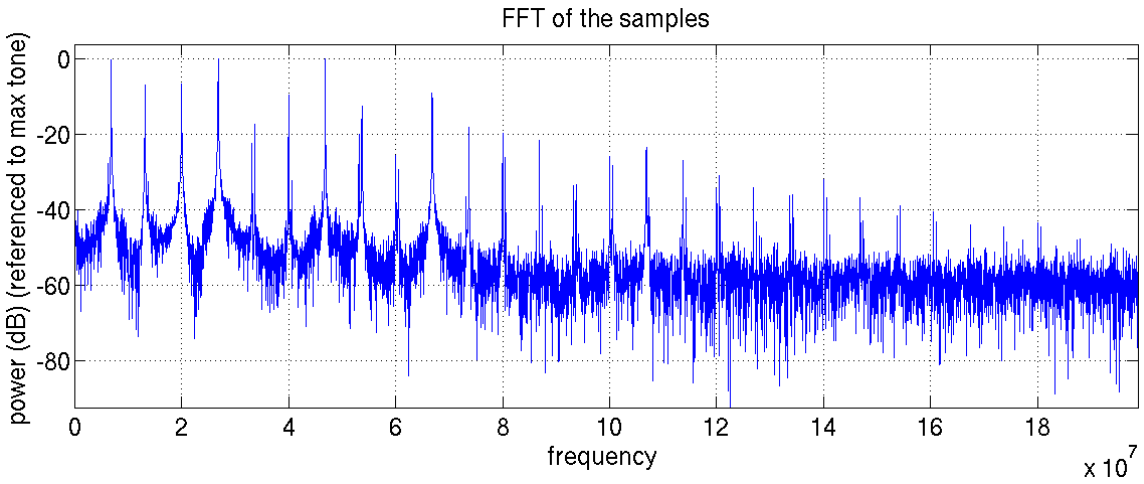

Figure 4.12: Spectrum (aliased) of samples showing no dominant carrier tone and hence a large index of modulation

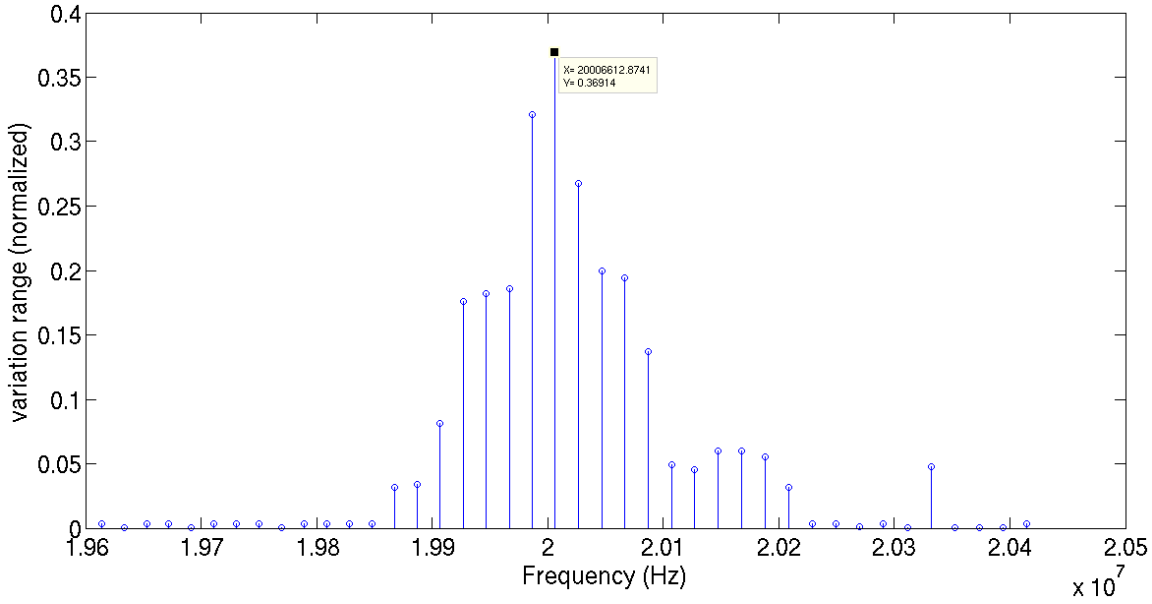

Figure 4.13: Cost function plot for envelope period estimation

that the synchronous setup mentioned above (sampling frequency exactly divides the carrier frequency) is sensitive to the initial phase of the carrier at the sampling instant. This is shown by sweeping the initial phase from 90 deg to 10 deg in steps of 10 deg while keeping the DUT in a intermediate-gain mode and the results are shown in Fig. 4.16. This makes it important to achieve phase synchronization between the sampling clock and the carrier clock which adds to the cost and complexity of the test setup.

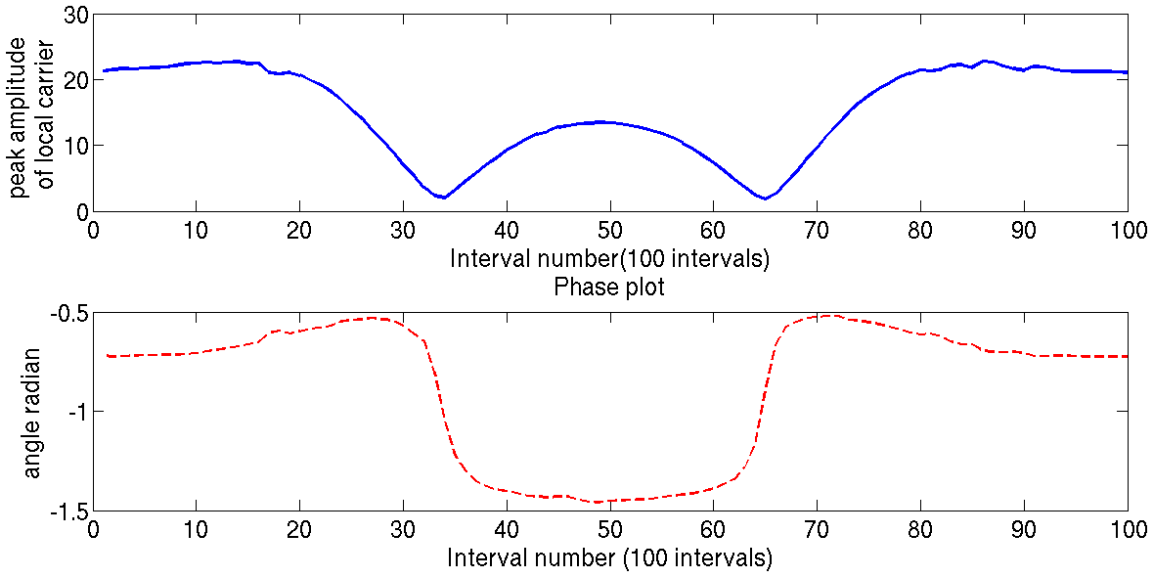

Figure 4.14: Extracted amplitude and phase (in π rad) of local carrier with envelope phase

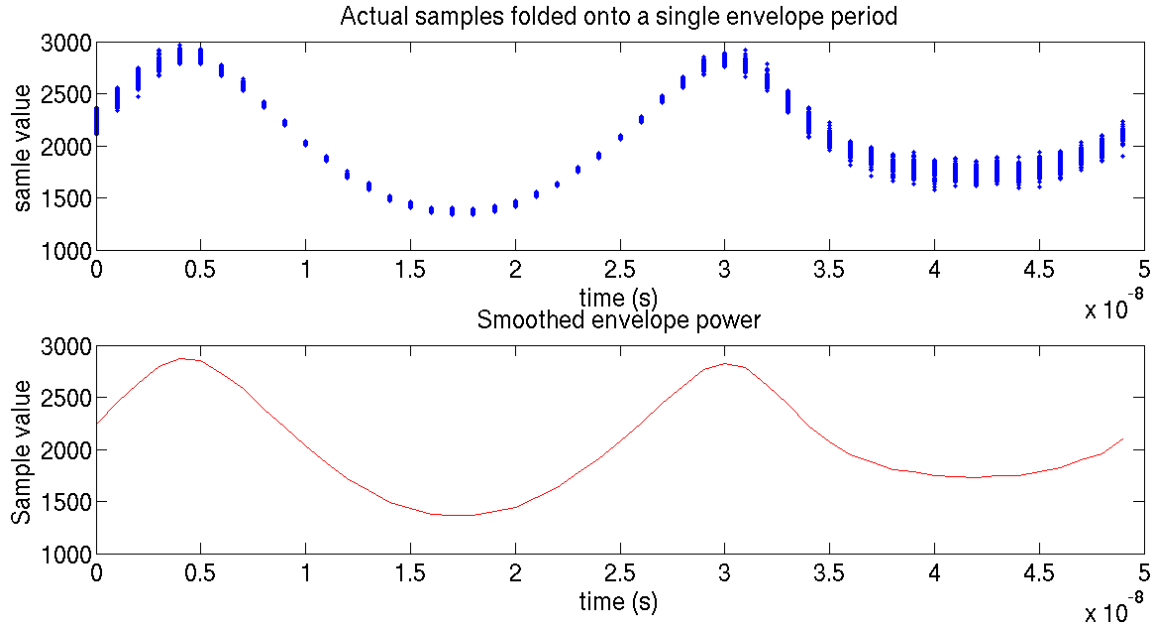

Figure 4.15: Extracted amplitude of local carrier with envelope phase for synchronous sampling 13 GHz carrier, 20 MHz envelope signal at -12 dBm at input and sampled at 1 GHz

4.4.2 Comparison of coherent and incoherent sampling

Due to the nature of the sampling (sampling frequency exactly divides the carrier frequency) chosen for coherent setup, the carrier phase information is mostly lost and appear as small amount of additional amplitude distortion. In coherent sampling, the sampling

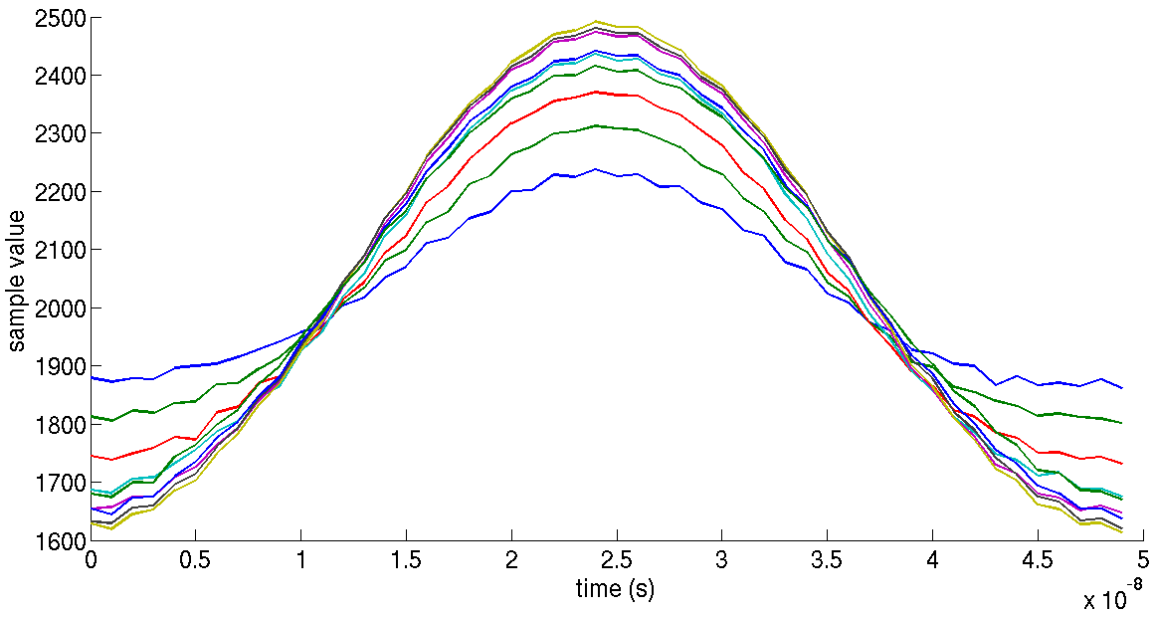

Figure 4.16: Extracted amplitude variation of local carrier with carrier phase at sampling clock edge for 13 GHz carrier and 1 GHz synchronous sampling

clock edge should be ideally coincident with the peak of the carrier to maximize the signal power and hence the signal to noise ratio. However, the peak of the carrier being a stationary point of the signal, this reduces the effect of the AM-PM on the envelope and hence any envelope based technique to separate out the amplitude to phase conversion effect will have to trade off phase induced sensitivity with signal to noise ratio (SNR). Such a trade-off of sensitivity and SNR is not present in proposed incoherent setup due to easy separation of the two effects and the phase of the carrier being measured over an entire carrier period instead of by its effect on the envelope shape. Hence, for comparing the accuracy of the incoherent setup against the coherent setup only the envelope amplitude characteristics for the two cases are compared. To avoid saturation in the digitizer, the DUT is set for intermediate gain and nonlinearity. The envelopes are reconstructed for similar carrier frequency in both cases (10 GHz for coherent and 10.17965 GHz for incoherent sampling) and same envelope frequency (20 MHz) and power (carrier at 0 dBm and envelope at -12 dBm). The reconstructed envelope amplitude characteristics after alignment are plotted in Fig. 4.17. The two curves are normalized to avoid power mismatch due to carrier phase offset in coherent setup. The two curves matches well at large amplitudes but the incoherent sampling

based reconstruction shows noise effects at low amplitude. Also in the incoherent sampling the peak power is less affected by the amplitude to phase effects while in coherent the peak shift of the carrier with respect to sampling edge due to amplitude to phase effect cause more asymmetric distortion in the envelope shape.

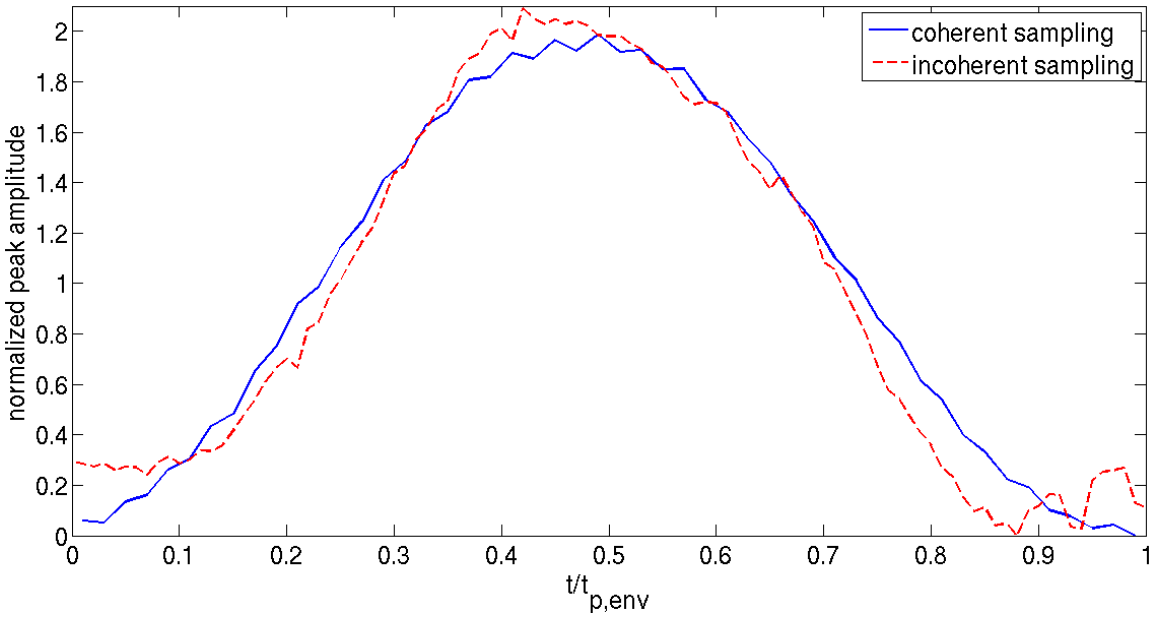

Figure 4.17: Comparison of extracted envelope amplitude characteristics for coherent (blue) and incoherent(red) sampling

The above procedure is repeated at few more power levels and mode settings. The carrier frequency is chosen to be around 13 GHz, the envelope frequency at 20 MHz. The envelopes obtained by coherent and incoherent setups are plotted in Fig.4.18. The corresponding correlation coefficients are tabulated in Table 4.2.

Table 4.2: Correlation coefficient between envelope data extracted from coherent and incoherent sampling for data shown in Fig 4.18

data set	a	b	c	d
R	0.9993	0.9992	0.9879	0.9863

The advantages of the proposed incoherent undersampling technique is evident at high power levels. In the given DUT it was observed that at high power level the amplitude to

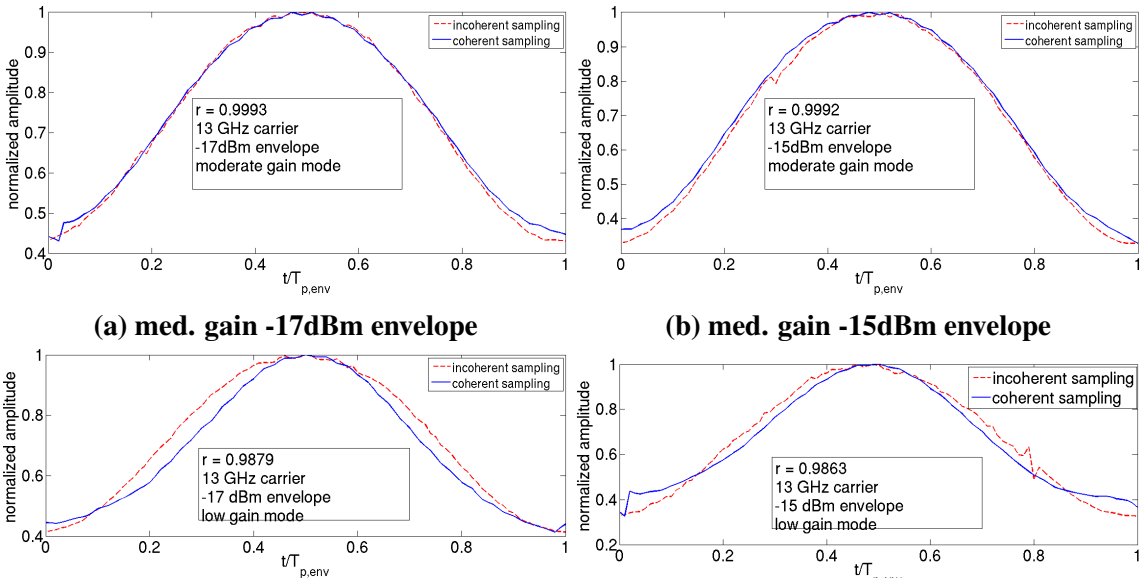

(a) med. gain -17dBm envelope **(b) med. gain -15dBm envelope**

(c) low gain -17dBm envelope **(d) low gain -15dBm envelope**

Figure 4.18: Comparison of envelope reconstruction using coherent and incoherent sampling

phase distortion showed a double peak. In the coherent sampling based acquisition, this showed up as a double peak in the envelope amplitude. However in the incoherent setup due to the inherent separation of phase and amplitude effects, the double peak correctly showed up in the phase characteristics and not in the amplitude characteristics as shown in Fig. 4.19. Such separation of phase and amplitude effects can help in device performance analysis.

4.5 Accuracy of reconstruction

The accuracy of the technique proposed in this work can be shown to be limited by the linearity and sampling uncertainty of the THA. In the case of this work the THA used has a 65 dB spurious free dynamic range and a sampling aperture jitter of less than 70 fs. The accuracy is also affected by the jitter in the sampling clock, especially low-frequency wander which can be important in free-running case and hence a stable source should be used for the sampling clock. If absolute value of the frequency is being measured, it is also necessary that the sampling clock frequency should be accurate to the precision of frequency estimation since all the frequency estimates are measured in reference to the

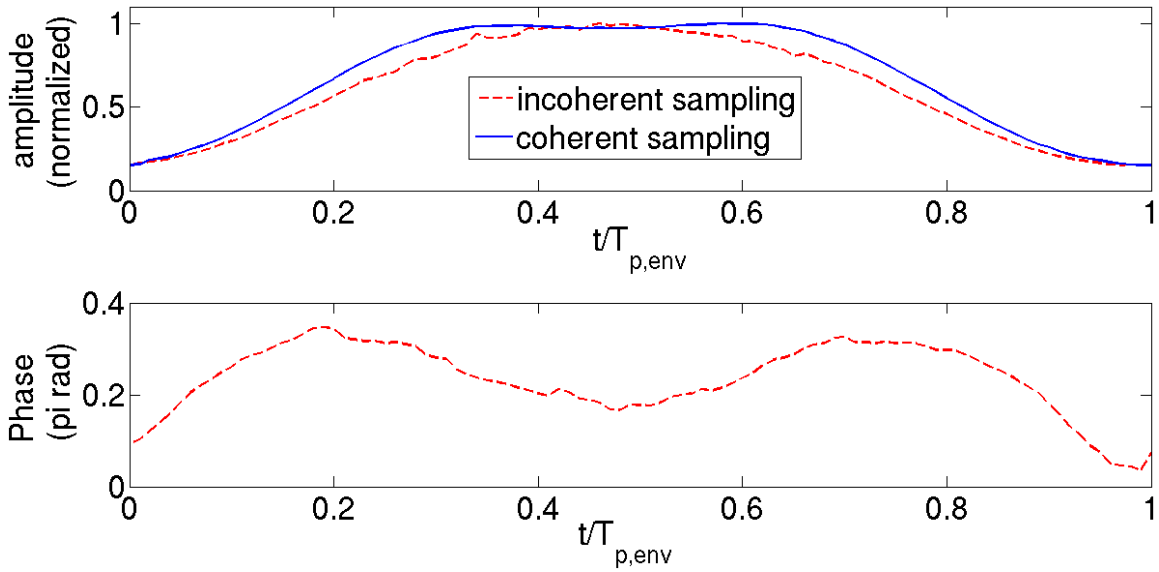

Figure 4.19: At high power level incoherent undersampling-based technique leads to separation of phase and amplitude effects

sampling-clock frequency. A free-running VCO is used in the experiment and the VCO under free-running condition has a large frequency instability. This limits the number of samples that can be used to extract the period of the carrier to approximately a thousand. But it has been shown in [45], that an accuracy of a few parts per million can be achieved with only a few hundred samples. The accuracy of the estimated characteristics of the DUT can be further improved by averaging the extracted data over multiple sample windows so that random errors from jitter are averaged out.

4.6 Conclusions

A low-cost setup is proposed for high-speed RF testing. The test instrumentation uses undersampling to reduce the cost of digitizer. No synchronization between the different clocks on the tester and signal sources are required thus allowing for reduced complexity of the test instrumentation by eliminating PLL. The proposed test setup does not suffer from sensitivity to unaccounted delay in the sampling clock paths since it uses incoherent sampling. Inherent separation of amplitude and phase distortion effect is achieved. The proposed setup is used to extract the envelope amplitude and phase distortion effects in a commercial mixer module. Using the recovered amplitude and phase characteristics,

one can easily derive the dynamic non linear model parameters of the DUT. This kind of measurement is often better than the static power sweep measurements due to possible memory effects in the measured parameters.

CHAPTER 5

INCOHERENT UNDER-SAMPLING BEYOND TRACK AND HOLD BANDWIDTH

5.1 Introduction

The track and hold amplifier (THA) dominates the cost of the setup for a incoherent under-sampling (IUS) setup. The THA limits the maximum bandwidth of the acquisition system. However, it is costly and sometimes practically impossible to extend the bandwidth of a wide-band system like a THA. To extend the bandwidth capability of the system further without extending the bandwidth of the THA a modified multi-channel architecture, can be used. It extends the bandwidth using mixers and provides a low-cost alternative. In this chapter we will combine the digital bandwidth interleaving (DBI) architecture with incoherent undersampling using both spectral estimation and time domain techniques for periodic signal waveform acquisition beyond THA bandwidth.

It is assumed that the period of the wide-band signal is known only approximately and no synchronization is allowed between the test setup and the source waveform. The proposed test system architecture preserves the cost benefits of the basic incoherent architecture, due to the lack of synchronization between the signal source and the tester clock. Under these conditions, the signals in the higher frequency bands after down-mixing are not likely to be periodic due to lack of a common period between the local oscillator and the input signal waveform. This implies that direct under-sampling based reconstruction using phase remapping as proposed in previous chapter for periodic waveforms is generally not applicable to the bandwidth interleaved signal acquisition setup.

However, by selecting the local oscillator (LO) frequency to be an integer multiple of the sampling clock, periodicity of the down-converted signal is restored leading to a simplification of the reconstruction technique along with an increase of accuracy. In the case such synchronization between the LO and the sampling clock is not possible a spectral estimation based technique can be used to estimate the power spectrum of the signal. Such

spectral estimation techniques need to be highly accurate in the presence of noise and windowing effects. Most fast Fourier transform (FFT) techniques rely on the use of a coherent window that spans over a integer number of periods of the test signal. However, the data after down-mixing in a bandwidth interleaving setup is not necessarily periodic, and its frequency is unknown. In such a case, a coherent window cannot be defined and the off-grid spectral components cause spreading in the FFT domain, limiting the spectral resolution achievable. We use an alternate technique that suits our test application and suffers less from spectral leakage due to windowing effects.

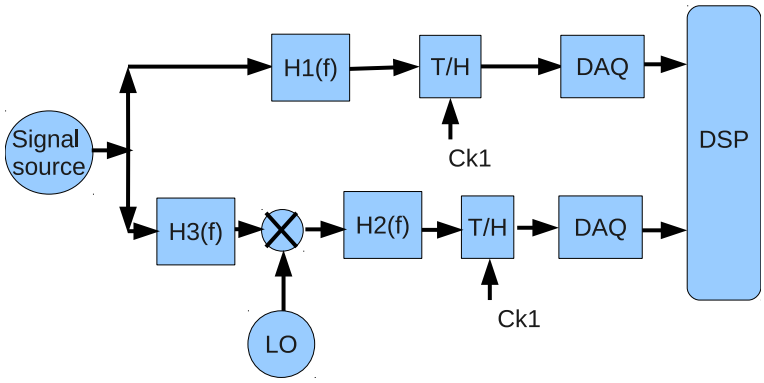

Figure 5.1: Schematic of a two band bandwidth interleaving waveform acquisition architecture. The data acquisition part uses incoherent undersampling

5.2 Bandwidth Interleaving

The basic 2-channel setup of a bandwidth interleaving data converter is shown in Fig 5.1. The input signal is divided into two or more channels, each of smaller bandwidth. The filters, H1 and H2 are low-pass filters to reduce out of band components. The filter, H3 is usually a band-pass filter which restricts the bandwidth of each channel and reduces aliasing. The signal in lower most frequency band is directly sampled and converted. The signal in each of the higher band channels is mixed with a clean tone generated by a local oscillator. This converts the band-pass signal to a base-band waveform, with small enough bandwidth for the data converter to sample directly. This allows signal acquisition beyond the bandwidth capability of the individual data converters. The accuracy of waveform capture is limited by the frequency stability of the LO clock and the sampling clock, distortion

introduced by the mixers, and the filtering effects in each channel. The down-converted signal from each band is combined through digital signal processing. Traditionally, the down-converted signal is over sampled so that the spectral estimation and correction is straightforward. However, to reduce the cost of the digitizer, in this work, signal in each channel is under-sampled. This introduces aliasing in the acquired waveform. To preserve the incoherent nature of the test setup, no synchronization is assumed between the LO and the data clock. Under these circumstances, the spectrum of the signal at the output of the mixer is potentially aperiodic. For example, let the signal period be given by f_{sig} and the LO clock frequency be f_{LO}. So that the input signal has spectral peaks at

$$\mathcal{F} = \{\pm f_{sig}, \pm 2f_{sig}, \pm 3f_{sig}, \ldots\}$$

depending on the choice of the LO frequency, after down conversion the dominant frequencies in the waveform spectra are given by

$$\begin{aligned} \mathcal{F}' &= f_{LO} - \{\pm f_{sig}, \pm 2f_{sig}, \pm 3f_{sig}, \ldots\} \\ &= \{\pm f_{sig} + \delta, \pm 2f_{sig} + \delta, \pm 3f_{sig} + \delta, \ldots\} \end{aligned} \tag{5.1}$$

where,

$$\delta = mod(f_{LO})_{f_{sig}}$$

is the grid offset from the ideal periodic grid for a period f_{sig} due to mixing operation with the LO clock. The frequency peaks are still on a uniformly-spaced grid of spacing f_{sig} but there is an offset from the ideal periodic frequency grid. Generally, this offset can be irrational and there is no common period of the signal. This makes the output of the mixer aperiodic as shown in Fig 5.2. So, it is necessary to modify the reconstruction technique to compensate for the shift in the frequency support of the signal.

At high data rate, replacing the band pass filter with a low pass filter is desirable. This can be achieved through lower sideband conversion by placing the local oscillator frequency at the upper edge of the frequency band and use a low pass filter before and after

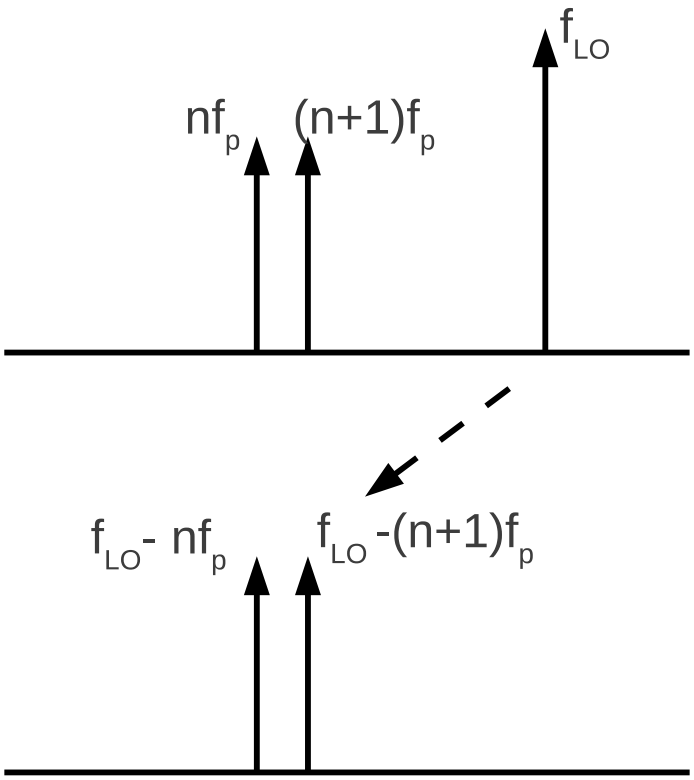

Figure 5.2: Effect of down conversion on the frequency of the signal: a periodic signal (top) having spectral peaks at integer multiples of fundamental gets translated to a signal with spectral peaks on an offset grid (bottom), without a common period

the mixer to reduce aliasing. However, extra processing step is needed to compensate for the inverted order of the frequency components and phase conjugation due to lower side band conversion.

5.3 High resolution spectrum estimation based reconstruction

For spectral-domain waveform reconstruction, high resolution and accuracy of the spectral estimation is required. A simple fast Fourier transform (FFT) based technique is inadequate since it suffers from too much leakage for a small number of samples and incoherent window. Since the signal is under-sampled, there is aliasing of spectral components. Hence, it needs to be "un-aliased" after the spectral estimation. To avoid the problem of aliasing, we directly estimate the signal by using a canonical definition of inverse FFT as a weighted

sum of the bases. Since the original signal is periodic, the spectrum of the signal is composed of spectral peaks (tones) located at integer multiple of the fundamental frequency of the signal. As mentioned in section 5.2, for a given choice of LO frequency it is easy to estimate the location of the spectral peaks of the signal after down-conversion. We define a sampling matrix defined as

$$A = \begin{pmatrix} e^{j\omega_1 T_s} & e^{j\omega_2 T_s} & \dots & e^{j\omega_n T_s} \\ e^{2j\omega_1 T_s} & e^{2j\omega_2 T_s} & \dots & e^{2j\omega_n T_s} \\ \vdots & \vdots & \ddots & \vdots \\ e^{mj\omega_1 T_s} & e^{mj\omega_2 T_s} & \dots & e^{mj\omega_n T_s} \end{pmatrix}$$

where m is the number of samples, n is the number of frequency components that fall in the band of interest, and T_s is the sampling time period. The frequencies, $\omega_1, \omega_2, \dots$ are given by :

$$\omega_i = i\omega_p + mod(f_{LO})_{\omega_p}$$

ω_p being the fundamental period of the signal. And by virtue of the periodicity, the signal will have spectral components at

$$f = f_{LO} - i\omega_p - mod(f_{LO})_{\omega_p}$$

If we assume that the spectrum of the signal evaluated at $f_{LO} - i\omega_p - mod(f_{LO})_{\omega_p}$, is given by C_i (C_i is complex), then the following relation must hold true,

$$Y = AC + \eta$$

where, C is the vector formed from the coefficients C_i Y being the vector formed by the samples acquired and η is random noise.

We estimate the spectrum C by :

$$\hat{C} = argmin\,\{||Ax - Y||_2^2 + \kappa||x||_1\} \tag{5.2}$$

which is a L1 regularized least mean square estimation problem. The method converges very fast with a few iteration of conjugate gradient. After estimating the signal in spectral domain, the time-domain signal is reconstructed using inverse fast Fourier transform (IFFT).

The resolution achieved is much better than that achieved by the standard FFT window. Two separate sets of data sampled at different sampling rates can be used to remove potential aliasing, if any. In the next section, simulation results are provided in support of the above claims.

5.3.1 Simulation results

To validate the results of the last section we used a simulation setup for the upper band of the bandwidth-interleaved system. The mixer was emulated by a multiplier function with a small amount of 3rd order non-linearity as given below:

$$mix_{out}(x(t), y(t)) = x(t)y(t) + \alpha_3 x^3(t)y(t)$$

coefficient α_3 is chosen to be small ($\sim 10^{-4}$); The output of the mixer is filtered with a low-pass filter having 3 dB cutoff at 12 GHz. The LO frequency is chosen to be at 26.177 GHz and the sampling frequency is chosen to be 1201 MHz. A noise is added to the signal after sampling. The noise power is chosen to be 40dB lower than the signal power. The simulation is carried out for both randomly chosen multi-tone signal and a 127 bit pseudo random bit stream (PRBS) signal filtered with a measured channel transfer function. The cost function plot for period estimation of a randomly chosen multi-tone signal with period 10 MHz is shown in Fig **??** and that for a 127-bit PRBS is shown in Fig **??**. The achieved accuracy of period estimation is of the order if 1 parts per million with just 1200 samples. The time-domain reconstructed waveform of the PRBS signal acquired over two different bands is shown in Fig 5.3. However this require some equalization of the distortion effects between the bands. In the following subsection we briefly discuss the estimation technique for equalization filter.

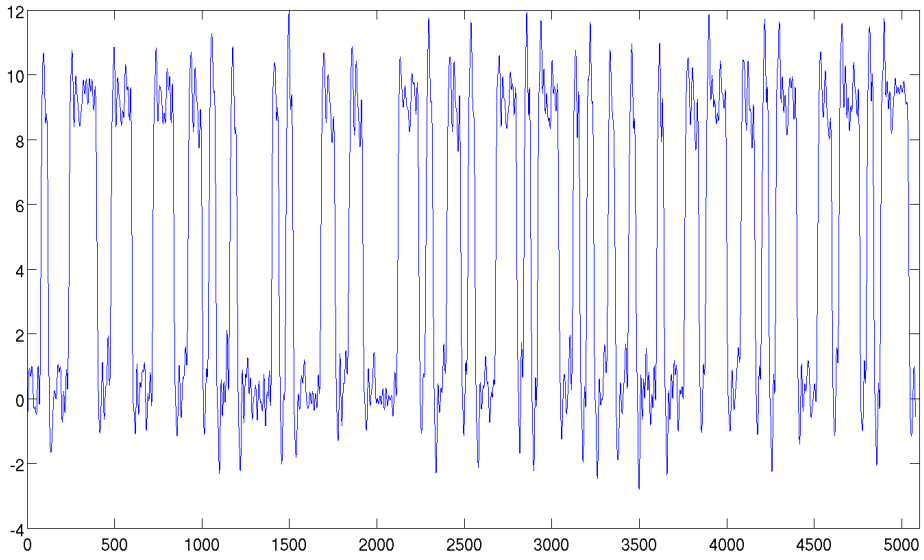

Figure 5.3: Reconstructed PRBS waveform by two channel bandwidth interleaving, x-axis represent sample number and y axis is waveform value

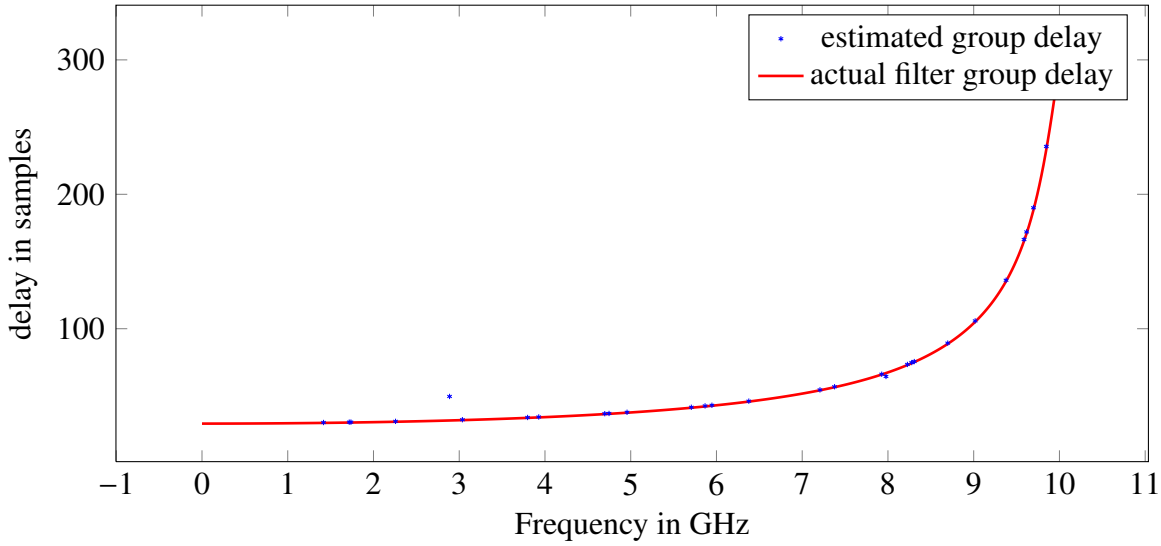

Figure 5.4: Estimated group delay for multi-tone simulations (1 sample = 2.5ps)

5.3.2 Estimating amplitude and phase distortion for equalization

To reconstruct signals from different bands, we need to estimate and equalize for the delay mismatch and the amplitude and phase distortion introduced due to the filtering effect of the individual channels. The amplitude distortion can be easily estimated by using a sinusoidal

pilot tone to measure the flatness of the channel filter function. However phase estimation is more difficult. Referring to Fig 5.1, the total phase contributed to the upper band has three sources: the filters H2, and H3 and the phase of the carrier at the 0th sampling instant, besides any contribution due to mixer nonlinearity and noise. Hence, it is clear that to enable equalization, the LO carrier phase must have a constant phase relationship with the sampling clock phase, this can be achieved by deriving the sampling clock by dividing the LO clock. Moreover, it is not feasible to use a reference tone to compare the phase at the input and the output of the channel. Thus any scheme used for equalization should not depend on controlling the absolute phase of the probe signal. To estimate the phase delay distortion, we used a four tone signal with a known phase relationship and estimate the delay at set of frequency sample points in the channel. Two of the tones are placed at a constant known frequency points while the other two are placed at the frequency sampling point. The extra pair of tones are required to remove ambiguity of phase delay arising due to asynchronous switching of the signal generator and the sampling clock. Using this data, we estimate a smooth group delay characteristics and use it to find the delay mismatch. To estimate the constant phase offset characteristics, we use two tone signal and estimate the phase difference between the reconstructed signal and the original signal after correcting for group delay distortion. To test the validity of the equalizer filter estimation technique, in simulation, we set H3 to be ideal zero phase brick wall filter and choose the local oscillator frequency to be a multiple of the sampling clock. The filter H2 is designed using the filter design toolbox in Matlab. The estimated delay then closely approximated the group delay of the filter H2, as shown in Fig 5.4.

5.3.3 Hardware Results

To validate the proposed data acquisition setup, a two tone signal at frequencies 1400MHz and 1500MHz, is used as the data signal. The samples were acquired at 511 MHz, using a FPGA board with a minimum sampling frequency of 500MHz. The LO frequency was chosen to be 1GHz. A 825 MHz low pass filter was used after the mixer to reduce out-of-band noise. The frequency estimation plot is shown in Fig 5.5, and the estimated spectrum

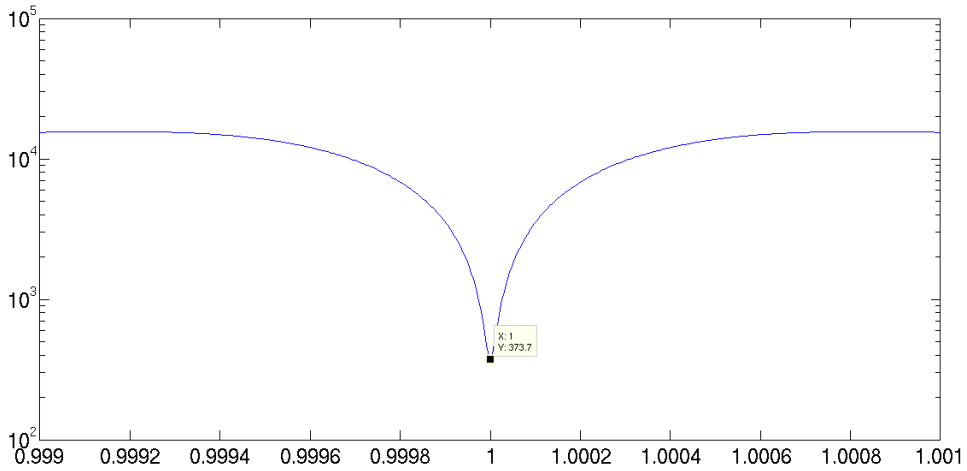

Figure 5.5: Frequency estimation of two tone signal at 1400MHz and 1500MHz; x-axis represents $F_p/F_{p-ideal}$

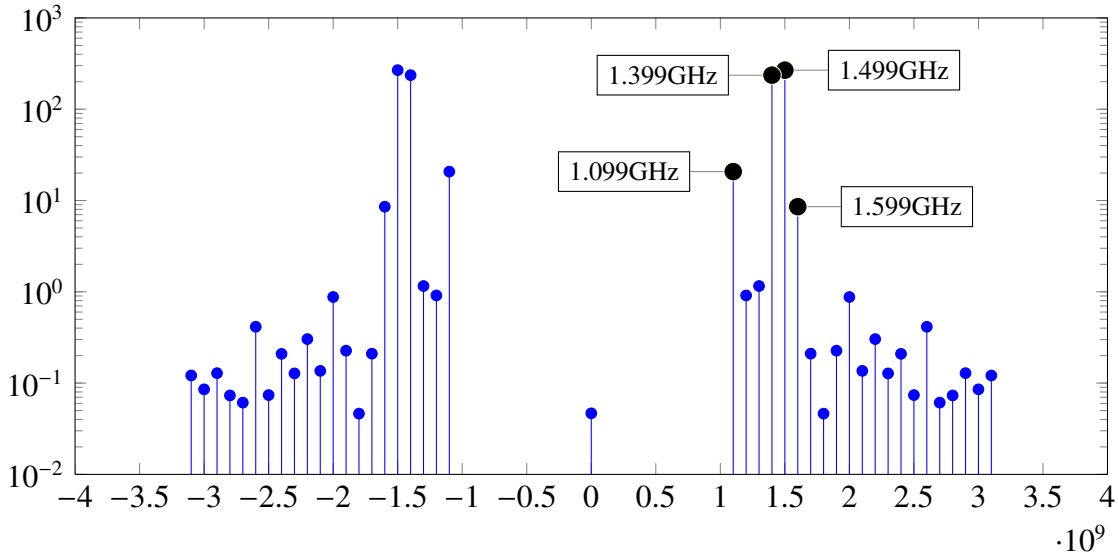

Figure 5.6: Reconstructed two tone spectrum

is shown in Fig 5.6. The time-domain reconstructed signal is shown in Fig. 5.7. It should be noted, that the noise in the spectrum gets cleaned up due to the estimation technique. There is also a feed-through component at 1 GHz in the spectrum due to mixer non-ideality. The gain flatness and the group delay response of the hardware setup, for the bandwidth of interest, is estimated from multiple two tone data sets at frequencies in the 1100 MHz to 1850 MHz band. The two tones were separated by 50 MHz. The estimated channel gain and group delay response is shown in Fig. 5.8 and Fig. 5.9 respectively. The gain flatness

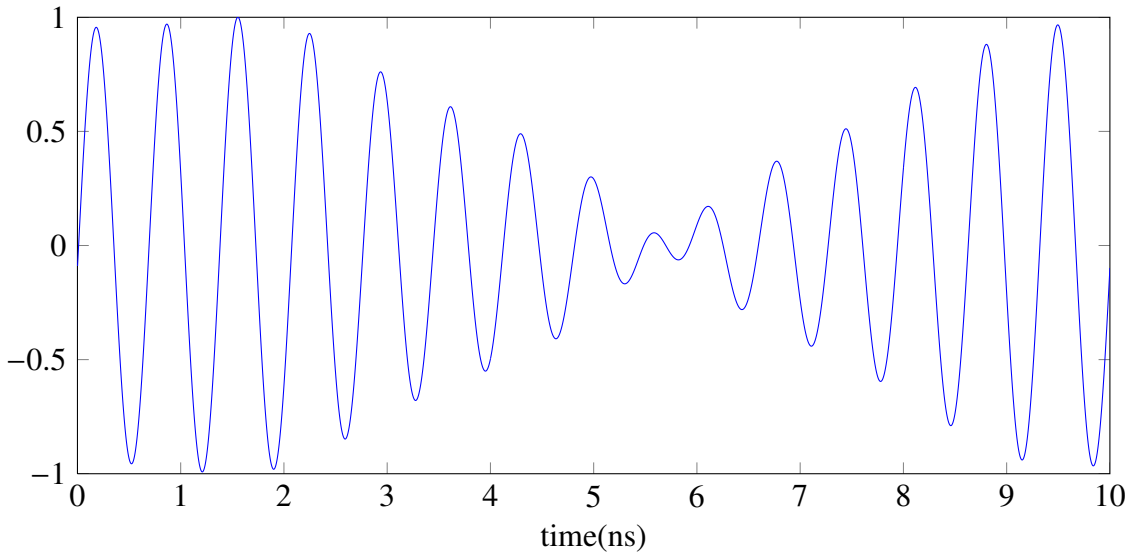

Figure 5.7: Reconstructed two tone waveform

closely approximates the transfer function of the 825 MHz low pass filter used in the setup.

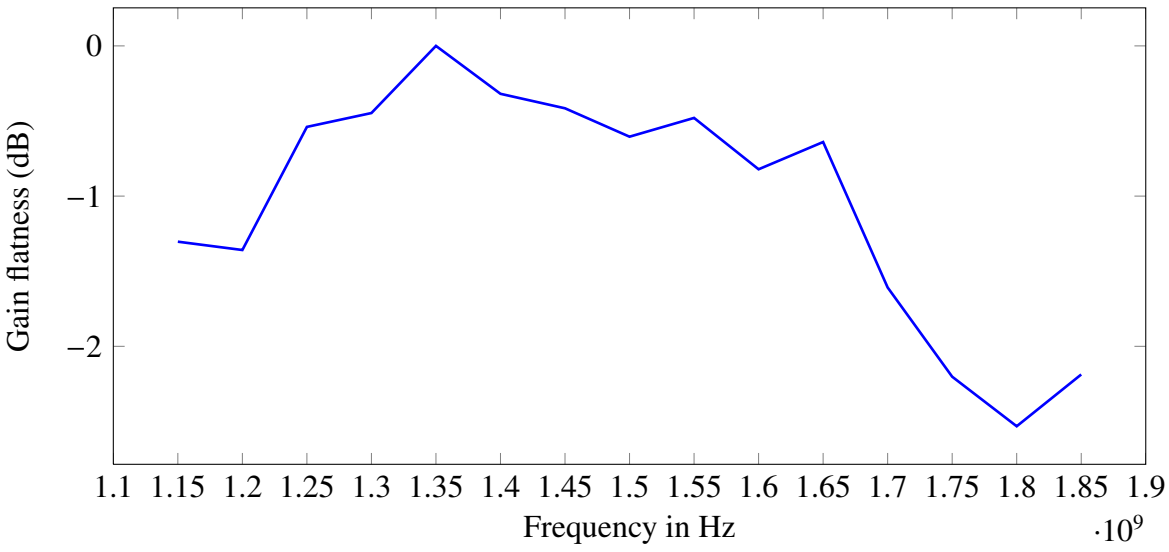

Figure 5.8: Estimated gain flatness for hardware setup from multiple two tone data

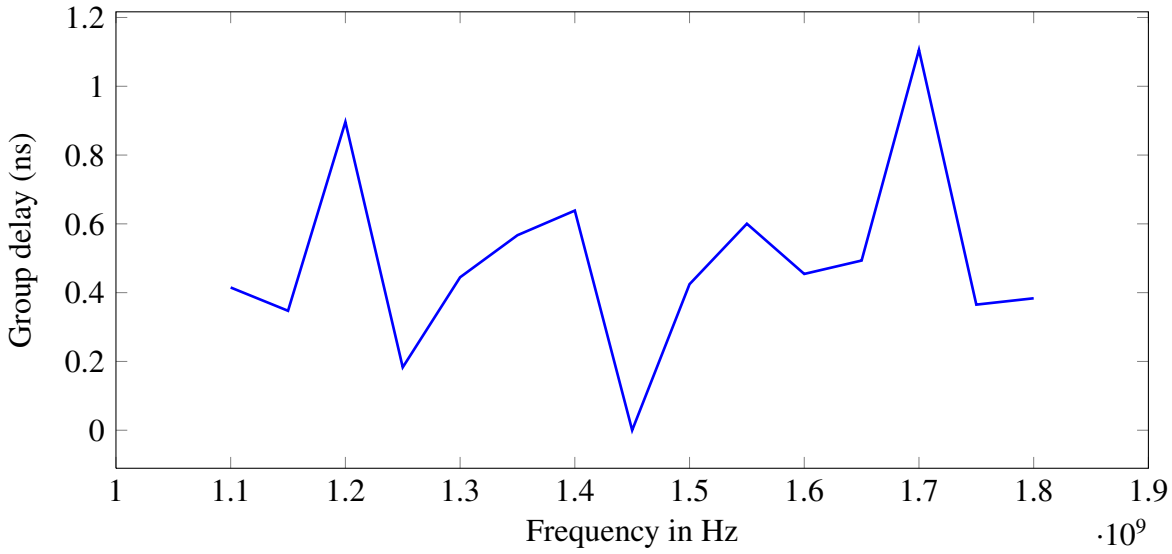

Figure 5.9: Estimated group delay response from multiple two-tone data

5.4 Proposed test setup for time domain reconstruction

As described previously, the bandwidth limitation of the track-and-hold amplifier can be surpassed by acquiring the wide band signal over multiple frequency bands, each band having a bandwidth less than the track and hold bandwidth. The setup is same as that shown in Fig. 5.1, under the assumption that the signal waveform is periodic. *To ensure a low cost test setup the local oscillator and sampling clock on the tester side are incoherent with respect to the test signal source. That is, there is no synchronization between the test signal source and the tester setup sampling clock/local oscillator*. Each band is acquired using incoherent undersampling (incoherent to test signal source) and combined using back-end signal processing algorithms. As mentioned earlier, this lack of synchronization potentially leads to a loss of periodicity in the signal at the mixer output, so that simple time-domain reconstruction techniques can not be used. In the proposed test setup, the sampling clock is chosen to have a period which is an integer multiple of the local-oscillator period. It is proved in the next section that choosing the sampling clock period to be an integer multiple of the local oscillator period restores the periodicity of the down converted signal for reconstruction purposes. Unlike previous sections, where due to a lack of periodicity, a

spectral domain technique was used leading to increased cost and complexity of the reconstruction technique, simple phase remapping based time domain reconstruction as shown in Fig. 3.1 can be used to reconstruct the signal on the basis of time domain period estimation. This simple condition on the frequency of sampling clock is the most important contribution of this work leading to a major simplification of the test instrumentation. Also, in a multi-band signal acquisition setup, since each band is separately processed and the filtering effect of each channel is compensated separately, the components in the different frequency channels need not be matched.

5.4.1 Validity of periodic reconstruction technique in the proposed setup : analytical proof

As a modification of the combined digital bandwidth interleaving and incoherent undersampling setup as proposed in 5.3, in this section, the LO frequency is restricted to be an exact integer multiple of the sampling frequency. The Fourier transform of a periodic signal is given by collection of impulses placed at integer multiples of the period. That is, if the period is given by T_p, then:

$$f(t + nT_p) = f(t)$$

and the spectrum is given by,

$$\hat{f}(\omega) = \sum_j \alpha_j \delta(\omega - 2\pi j/T_p)$$

where the index of summation j runs over all integers and $\delta(\cdot)$ is the Dirac delta function.

At the output of the mixer the spectral peaks shifts due to mixing. The spectrum at the mixer output is given by:

$$\hat{f}_{mix}(\omega) = \sum_j \alpha_j \delta(\omega - 2\pi j/T_p - 2\pi f_{LO})$$

where f_{LO} is the local-oscillator frequency. This is shown in Fig. 5.2. Even though the spectrum consists of isolated spurs separated by integer multiples of the fundamental frequency of the signal, the frequencies are offset due to the mixing operation. Hence the signal at the mixer output is not periodic unless the LO frequency is also a multiple of the signal period, which is not the case for an incoherent undersampling based test setup.

If the waveform at the output of the mixer is sampled as $f_{sampled}(n) = f_{mix}(nT_s)$ then the spectrum of the waveform at the output of the THA is a periodic repetition of the spectrum at the mixer output as given by:

$$\begin{aligned}\hat{f}_{samp}(\omega) &= \sum_j \hat{f}_{mix}(\omega - 2\pi j/T_s) \\ &= \sum_j \sum_k \alpha_j \delta(\omega - 2\pi k/T_p - 2\pi f_{LO} - 2\pi j/T_s)\end{aligned} \tag{5.3}$$

Where T_s is the sampling period. If the sampling clock and the local oscillator frequency are related by

$$f_{LO} = k_1/T_s \text{ for some integer } k_1$$

then, the relation in equation (5.3) simplifies to:

$$\hat{f}_{samp}(\omega) = \sum_j \sum_k \alpha_j \delta(\omega - 2\pi k/T_p - 2\pi j/T_s) \tag{5.4}$$

This is the same expression as that for the spectrum of the samples of the original periodic signal waveform. This implies that the samples acquired corresponds to the samples acquired by directly under-sampling the input periodic waveform with a wider bandwidth THA. The same can be proved from a purely time domain point of view: When sampled by a clock which is derived from the LO clock through frequency division with an integer division ratio, the samples acquired at the mixer output represent a signal which has the same period as the input waveform. The input signal with a period T_p, obeys

$$f(t + T_p) = f(t) \qquad \forall t$$

The signal at the mixer output after filtering is given by

$$f_1(t) = (f(t)c(t)) * g(t)$$

where $c(t) = c(t + T_{LO})$ is the clock waveform, $g(t)$ is the filter function and $*$ is the convolution operator. That is,

$$f_1(t) = \int f(t - \tau)c(t - \tau)g(\tau)\mathrm{d}\tau \tag{5.5}$$

so the samples are given by,

$$f_1(nT_s) = \int f(nT_s - \tau)c(nT_s - \tau)g(\tau)\mathrm{d}\tau \tag{5.6}$$

since the sampling clock is derived from the LO clock by integer division,

$$c(nT_s + t) = c(t)$$

so that,

$$f_1(nT_s + \tau_0) = \int f(nT_s + \tau_0 - \tau)c(\tau_0 - \tau)g(\tau)\mathrm{d}\tau \tag{5.7}$$

If $nT_s - mT_s = kT_p + \epsilon$, and $\tau_0 = 0$ then,

$$\begin{aligned}
&|f_1(nT_s) - f_1(mT_s)| \\
&= \left| \int \{f(nT_s - \tau) - f(mT_s - \tau)\}c(-\tau)g(\tau)\mathrm{d}\tau \right| \\
&= \left| \int \{f(nT_s - \tau) - f(nT_s - kT_p - \epsilon - \tau)\}c(-\tau)g(\tau)\mathrm{d}\tau \right| \\
&= \left| \int \{f(nT_s - \tau) - f(nT_s - \epsilon - \tau)\}c(-\tau)g(\tau)\mathrm{d}\tau \right| \\
&\leq \epsilon\Lambda_f \, max|c(t)| \int |g(\tau)|\mathrm{d}\tau \\
&= \epsilon\Lambda
\end{aligned} \tag{5.8}$$

where, Λ_f is the maximum of the absolute value of slope of the input waveform. The above equation confirms that the samples represent a continuous periodic function with the same period as that of the input waveform. This implies that the samples can be time folded similar to the phase remapping technique described earlier. And that the fundamental period can be estimated by using a time-domain metric described earlier.

5.4.2 Sensitivity to carrier phase at sampling edge

In the time-domain analysis presented in the last subsection, the epoch carrier phase for the first acquired samples, τ_0 is assumed to be 0. But in practice it is hard to control the phase of the setup accurately without complex phase alignment circuits. If we assume $T_p \geq \tau_0 \geq 0$,

then the acquired samples in presence of a small timing offset τ_0 in the sampling edge can be written following eqn. (5.7),

$$\begin{aligned} f_1(nT_s, \tau_0) =& f(nT_s + \tau_0) \\ &= \int f(nT_s + \tau_0 - \tau)c(\tau_0 - \tau)g(\tau)\mathrm{d}\tau \end{aligned}$$

with change of variable $\tau - \tau_0 \rightarrow \tau$

$$= \int f(nT_s - \tau)c(-\tau)g(\tau + \tau_0)\mathrm{d}\tau$$

if carrier waveform has even symmetry around 0,

$$= \int f(nT_s - \tau)c(\tau)g(\tau + \tau_0)\mathrm{d}\tau \tag{5.9}$$

so that,

$$f_1(nT_s, \tau_0) - f_1(nT_s, 0) = \int f(nT_s - \tau)c(\tau)\left[g(\tau + \tau_0) - g(\tau)\right]\mathrm{d}\tau$$

So it is important to provide minimum bandwidth for the low-pass filter represented by the impulse response $g(t)$ to reduce the sensitivity to small error in phase matching between sampling clock and the LO clock since the value of $\{g(\tau + \tau_0) - g(\tau)\}$ increases as the bandwidth of $g(t)$ increases. In general, the lower the bandwidth at the output of the mixer, the waveform is less sensitive to small offset in the initial carrier phase at the sampling clock edge. Therefore it is important to minimize the bandwidth of each channel to reduce the sensitivity to small phase-matching errors between the sampling clock and the LO clock.

5.5 Simulation Results

To simulate the signal reconstruction procedure, a 16 bit pattern 1010110010110100 at 10 Gbps is over sampled and filtered using a 10 GHz to 20 GHz cutoff band pass filter. This and all the other filters used are synthesized as type 2 Chebyshev filters using the Matlab filter synthesis command. The waveform is down-converted using a sinusoidal carrier at 14.579 GHz. Subsequently, the signal is a) sampled directly and, b) sampled after passing it through a low pass filter with cutoff 8 GHz. The sampling frequency is chosen to be $1/15^{th}$ of that of the local oscillator. The band pass filtered signal and its reconstruction when

there is a perfect phase match between the sampling clock and the local oscillator is shown in Fig. 5.10. To verify the effect of sampling phase offset and the filter bandwidth on the

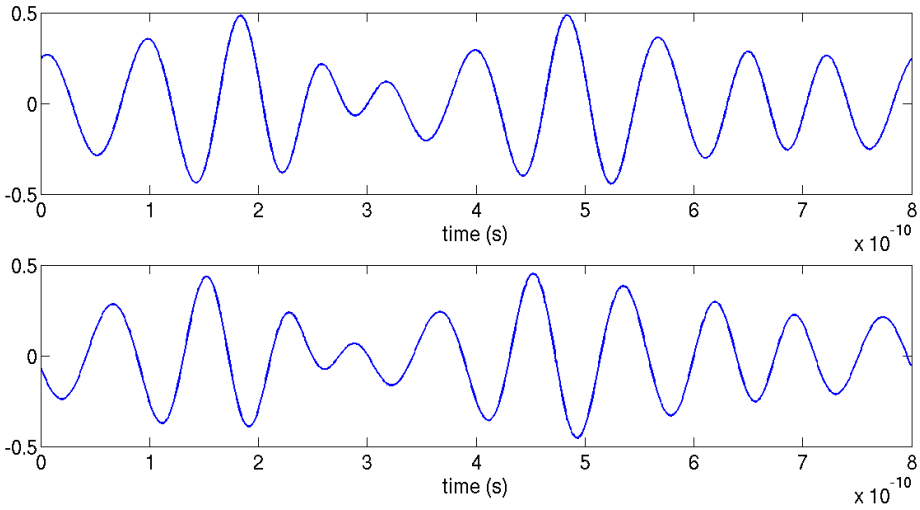

Figure 5.10: The band pass filtered waveform(top) and the reconstructed waveform obtained through time folding of incoherently undersampled data after down mixing(bottom). x-axis is time, y-axis is normalized value

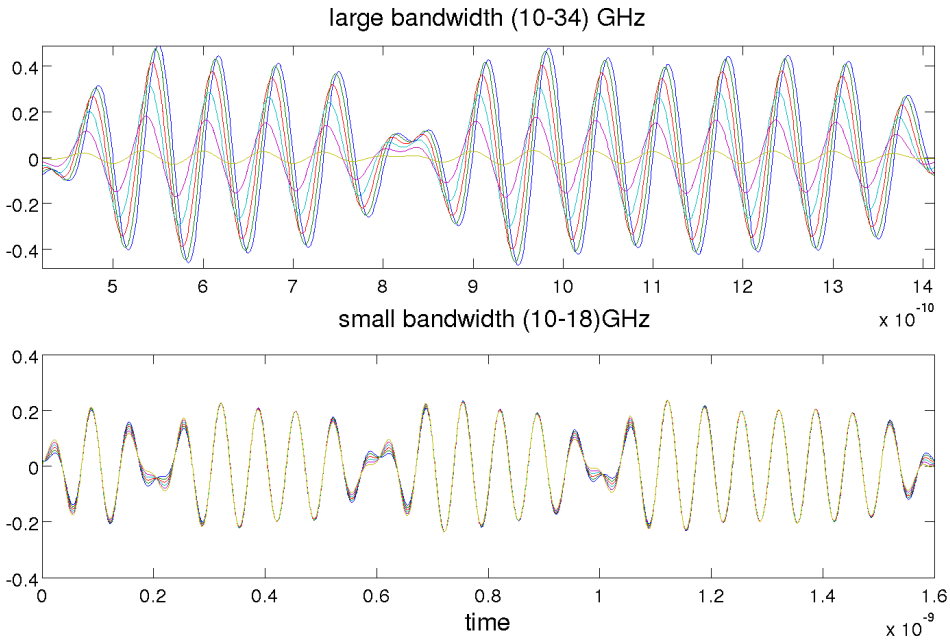

Figure 5.11: Sensitivity to initial phase offset for direct sampling at mixer output (top) and sampling after passing through a low pass filter (bottom), the initial phase offset is swept over one quadrant and the corresponding reconstructed waveforms are plotted.x-axis is time, y-axis is normalized value

accuracy of reconstructed signal waveform, the initial sampling phase offset between the

carrier and the sampling clock is swept from 0 to $\pi/2$ of the carrier clock by incorporating a time offset in the sampling clock. The results are shown in Fig. 5.11, where the top part of Fig. 5.11 shows data without the use of a low pass filter and the bottom part shows data with the use of a low pass filter. It can be easily verified that the low bandwidth of the low pass filter after down mixing reduces the sensitivity of the reconstruction error to the initial sampling phase error. Also, the waveform shows no significant sensitivity in waveform amplitude to phase offset. There is a small delay as expected and the error is much smaller than that for direct sampling after passing through mixer without a low pass filter. One important point that needs to be mentioned here is that the LO frequency need not be placed at the edge of the band to be down converted, as long as it does not fall on the periodic grid causing components to directly overlap after down-mixing.

5.6 Hardware validation

The schematic of the hardware setup for proof-of-concept of the reconstruction algorithm is shown in Fig. 5.12. The central core of the system is designed with a Hittite HMC554LC3B passive mixer with a 7-9dB conversion loss over 11-20GHz bandwidth. To compensate for the loss, the signal is pre-amplified with a Minicircuits AVA24+ broadband amplifier with 12dB gain from 5-20GHz and another stage of amplification after down conversion using Mnicircuits PMA-5453+ with nominal 19dB gain upto 6GHz. To prevent the carrier feed through components and also to limit the bandwidth the signal at the output of the mixer is passed through a LFCN8400+ 8.4GHz cutoff low-pass filter from Minicircuits. The preamplifier, the mixer, the low pass filter, and the base band amplifier are all placed on a test module shown in Fig. 5.13. The lower frequency components of the waveform is suppressed using a PMI HP10G high-pass filter with 10 GHz cutoff. The data at the output is sampled using a Hittite 18 GHz bandwidth THA HMC660LC4B evaluation board and digitized and acquired using a National Semiconductor ADC12D1800 ADC evaluation board. The sampling clock and the LO clock are generated by synchronized stand alone source. A frequency rich test waveform is generated by passing a digital pattern from

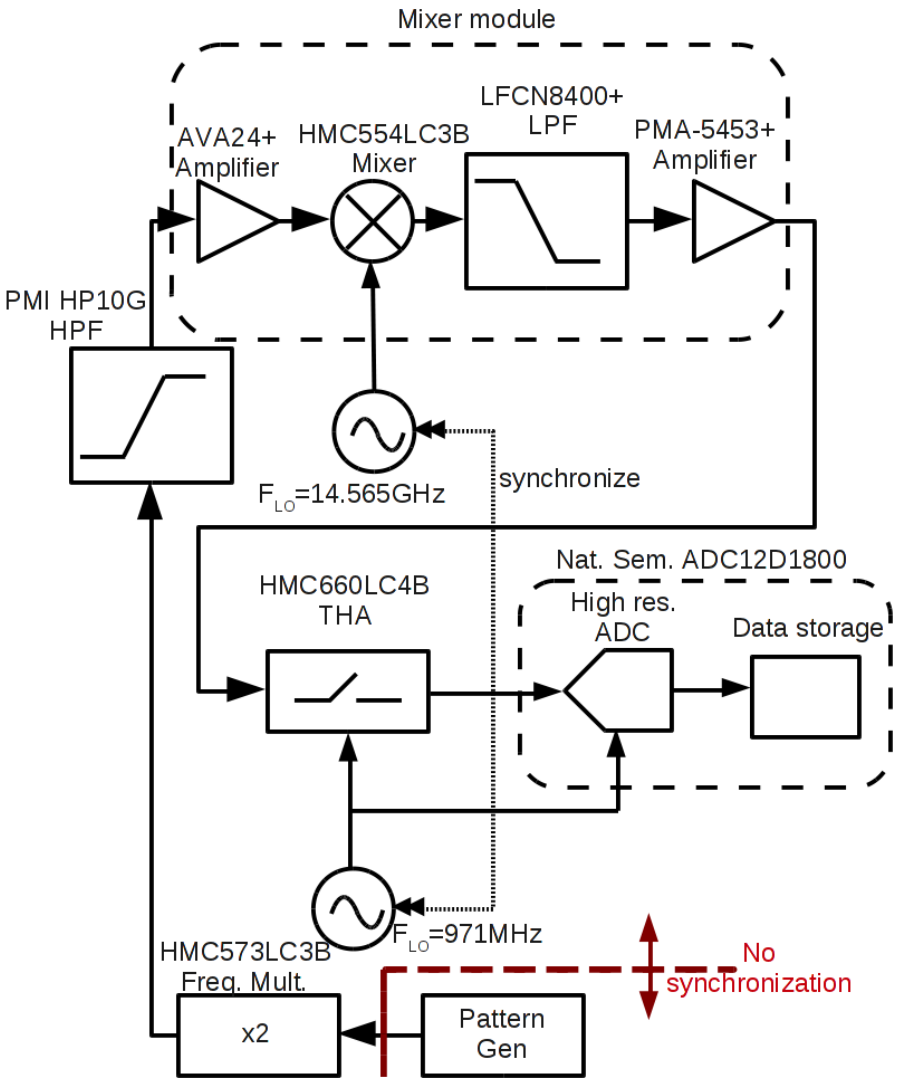

Figure 5.12: Hardware setup for digital bandwidth interleaving based acquisition of periodic waveform, the sampling and LO clocks are incoherent with respect to the source pattern generator

a 3.35 Gbps digital pattern generator through a Hittite HMC573LC3B 8-22 GHz output active frequency doubler.

As a test signal, a 8 bit pattern 10101100 was generated from the pattern generator at 3.35 Gbps and passed through a frequency doubler and high pass filter. The period is estimated by minimizing the zero crossing cost function described in Chap. 3. The corresponding cost function plot is shown in Fig. 5.14. This also verifies the periodicity of the signal at the output of the THA.

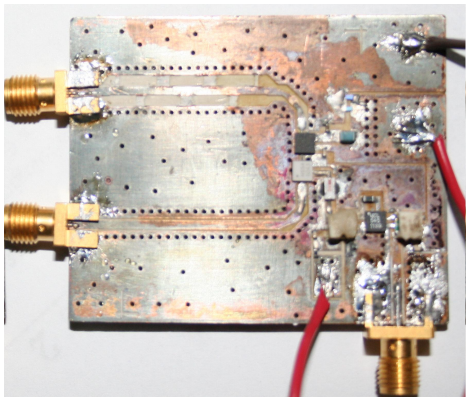

Figure 5.13: Picture of the mixer module used to down-convert the signal

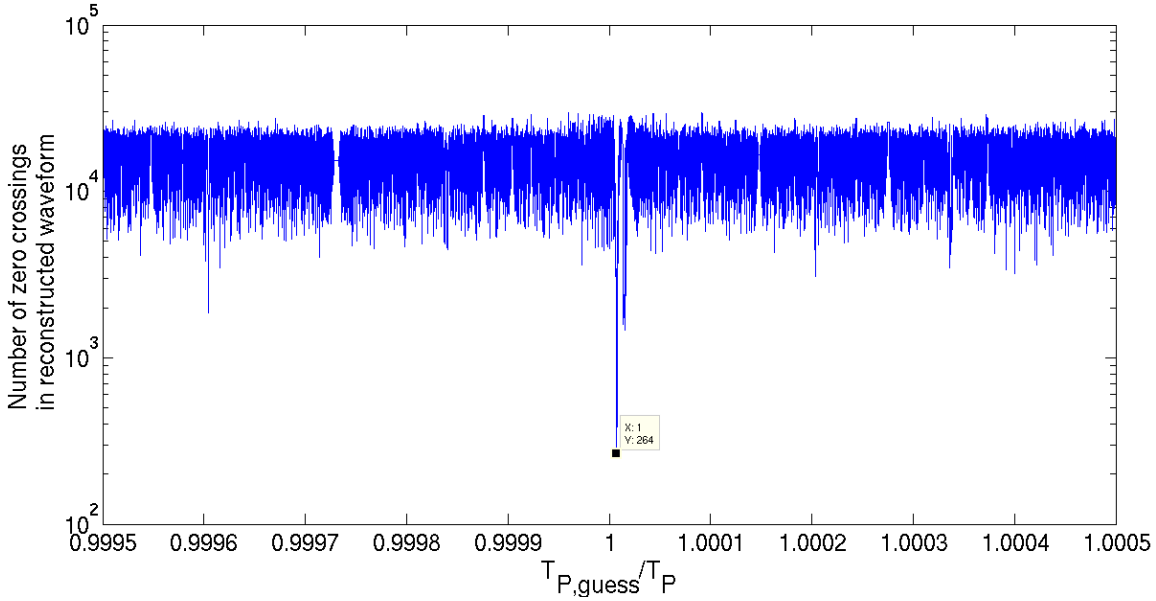

Figure 5.14: Zero-crossing cost function plot for estimating period of the acquired signal ([10101100] pattern 3.35Gbps passed through a frequency doubler and high pass filter with 10GHz cutoff), x-axis is the ratio of guessed period to the actual period and y-axis is the number of zero crossings in the reconstructed waveform, the sharp minima is the period

5.6.1 Estimation of the transfer function and equalization

For an accurate reconstruction of signal waveform, it is necessary to equalize for the filtering effects introduced by the test setup. This requires the channels transfer functions be estimated. In the present work the channel transfer function was estimated using spectrally diverse signal waveforms as probe signals and a reference reconstruction from direct undersampling due to absence of a more accurate standard for calibration (the accuracy can be

easily improved if such a source is available). The use of a spectrally diverse probe signals, enable a better estimation of the group delay behavior of the channel compared to multi-tone signals using significantly less number of measurements. It is also easier to generate such signals using pattern generator source compared to single tone or multi-tone signals since in multi-tone signals it is practically not possible to control the amplitude and phase balance of the different tones over the whole band at high frequencies. The estimated transfer function is shown in Fig. 5.15, the red dots being the raw data points and the blue solid line being the estimation after smoothing over multiple experimental data sets to reduce the effect of measurement noise. In estimating the transfer function, the spectral components with energy lower than a selected threshold level are removed to reduce the effect of noise amplification. The values from 18-20 GHz have accuracy limitation because of these being beyond the THA bandwidth which distorts the acquired samples used as reference for the estimation. The equalization is achieved using an inverse filter synthesized from the estimated channel transfer function.

Minimum phase estimation Even though in the results presented in this work, both phase and amplitude is estimated from the probe signal reconstruction, it must be mentioned that the phase estimation is usually very sensitive to noise. However since most stable systems are minimum phase (or can be represented by an equivalent minimum phase system cascaded with a delay element), the phase transfer function can be estimated from the amplitude transfer function. In minimum phase systems, the phase transfer function in the Hilbert transform of the amplitude transfer function and hence the two are not independent.

Matching the power in two bands While the equalization in each band can be implemented by estimating the intra-band filter transfer function, it is important to also equalize the delay and gain for each band while combining signals from each band. The gain in different bands can be estimated by allowing small amount of overlap band between each consecutive channel in the multi-band setup. After applying the intra-band equalization to each band the gain in each band is adjusted so that the signal components in the

overlap region of the two bands agree as much as possible. However the small amount of mismatch due to error in estimating the signal near the band edge can be taken care of by combining the signals using a smooth transition function over the two bands in the overlap region using a smoothly varying weight as:

$$\hat{f(t)} = \alpha \hat{f_1(t)} + (1 - \alpha)\hat{f_2(t)} \tag{5.10}$$

where, $f_1(t)$ and $f_2(t)$ are the reconstructed spectra after equalization in bands 1 and 2 respectively and $0 \leq \alpha \geq 1$ is a smoothly varying parameter between the two bands. $\alpha = 0$ at the left edge of the overlap and $\alpha = 1$ at the right edge of the overlap region.

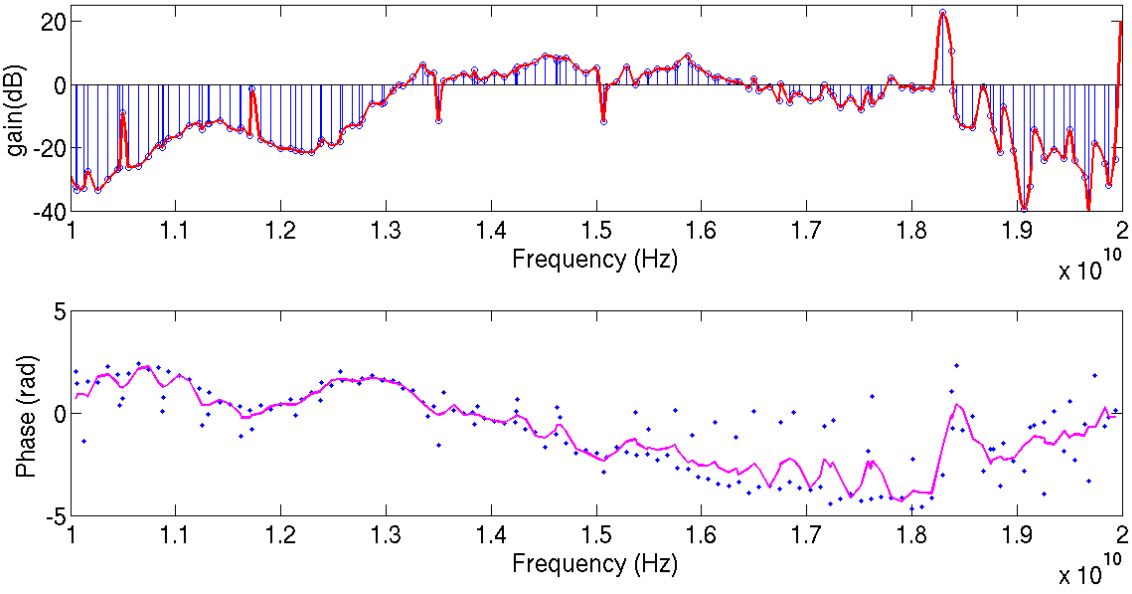

Figure 5.15: Estimated gain(top) and phase(bottom) transfer function of the mixer module

Using the estimated transfer function, we equalize the filtering effect and reconstruct a 31 bit prbs pattern output at 3.35 Gbps passed through a frequency doubler and a high pass filter. The time domain compensated waveform is shown along with the reference waveform directly sampled after the high pass filter in Fig. 5.16. The corresponding spectra are shown in Fig. 5.17.

After correcting for the non-ideal channel response the channels need to be matched for gain and delay at the overlap regions. the gains can be matched by ensuring an overlap

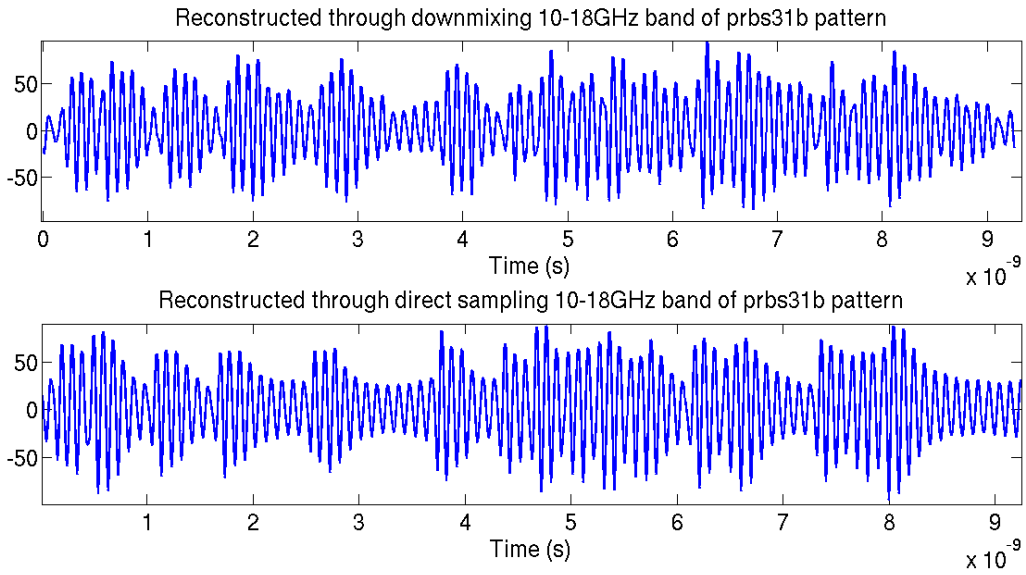

Figure 5.16: Equalized(top) and reference(bottom) time domain waveform. The equalized signal is acquired using the proposed setup after downmixing and compensated for the filtering effects of the channel, while the reference setup is acquired using direct incoherent undersampling of the high pass filter output

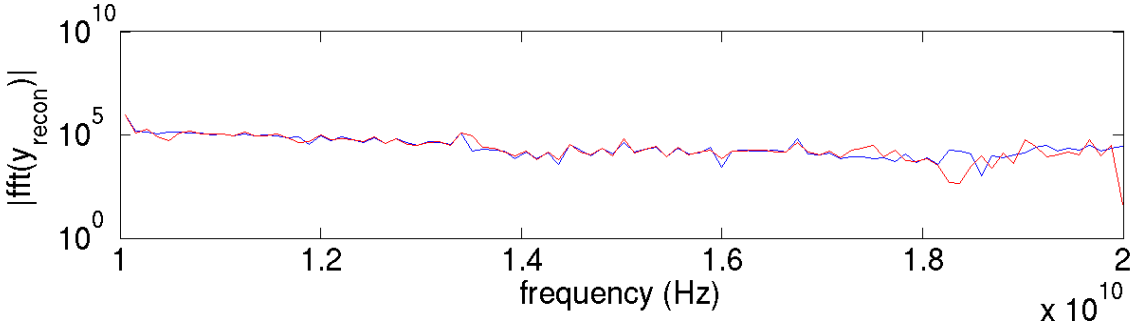

Figure 5.17: Equalized (blue) and reference (red) magnitude(top) and phase(bottom) spectrum. The equalized signal is acquired using the proposed setup after downmixing, while the reference setup is acquired using direct incoherent undersampling of the high pass filter output

between the flat band response of the adjacent bands and choosing the gains so as to maintain a continuity of the spectrum across the overlap region. To combine the two bands a hard cutoff can be chosen for frequency or smooth transition from one band to the other can be chosen. As an example for the test signal described in the last paragraph, the spectrum after gain balancing in the overlap between the two bands is shown in Fig. 5.18. The delay between the two channels is not estimated because there is no fixed inherent delay in the

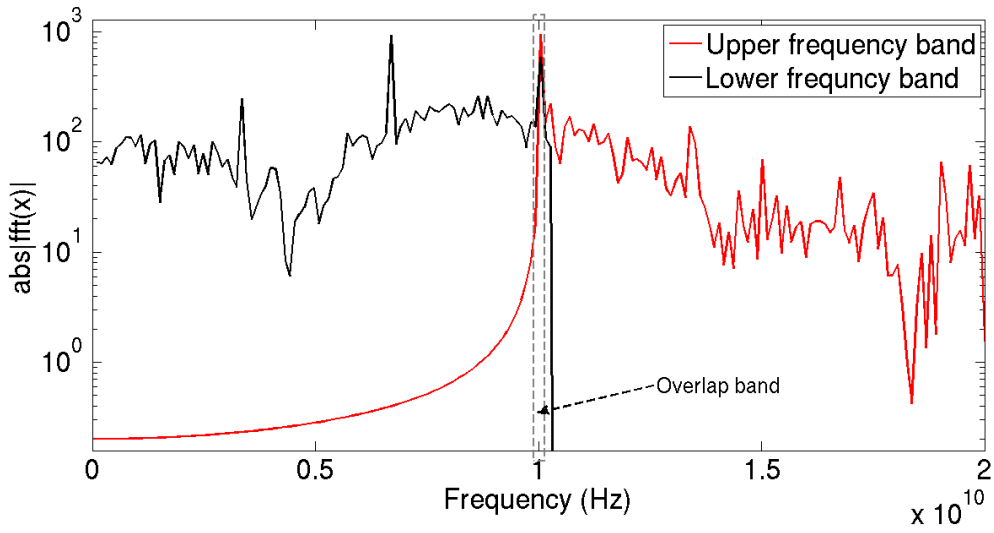

Figure 5.18: The lower (black) frequency band and the upper frequency band signals

experimental setup used and it varies from run to run. As a demonstration the low-pass

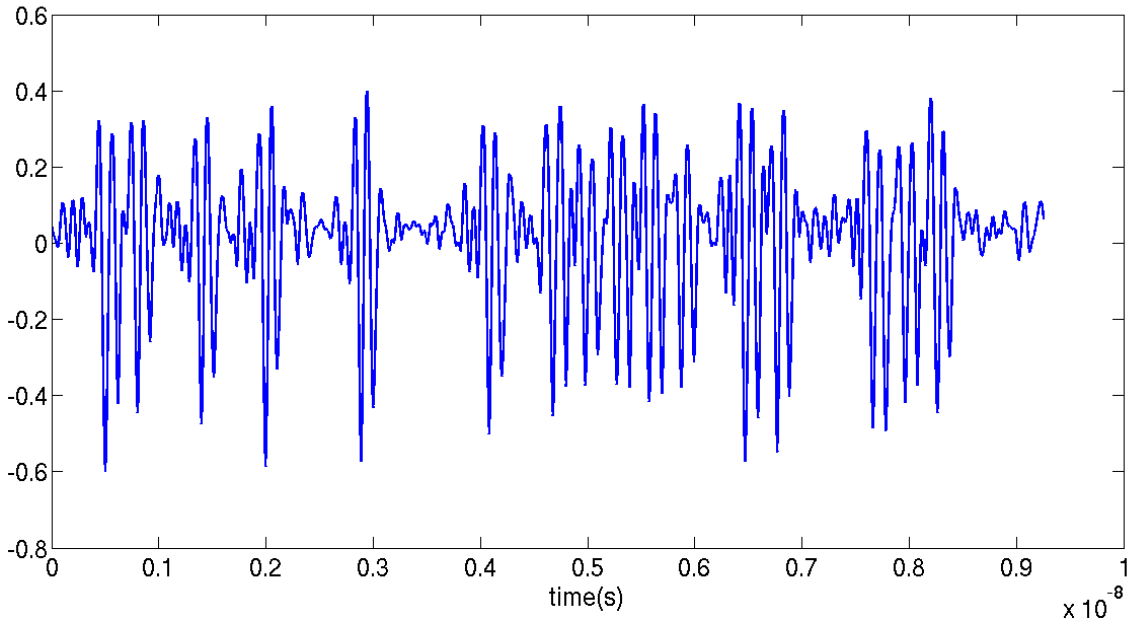

Figure 5.19: Reconstructed by recombining from 2 channels delay is equalized manually, 31 bit prbs at 3.35 Gbps passed through a frequency doubler. x-axis is time and y-axis is normalized

component (below 10 GHz) of a output of the doubler directly acquired through incoherent under-sampling is combined with the estimated and equalized high frequency component (10 - 20 GHz) shown in Fig. 5.19. Along with the 18 GHz bandwidth reconstruction using

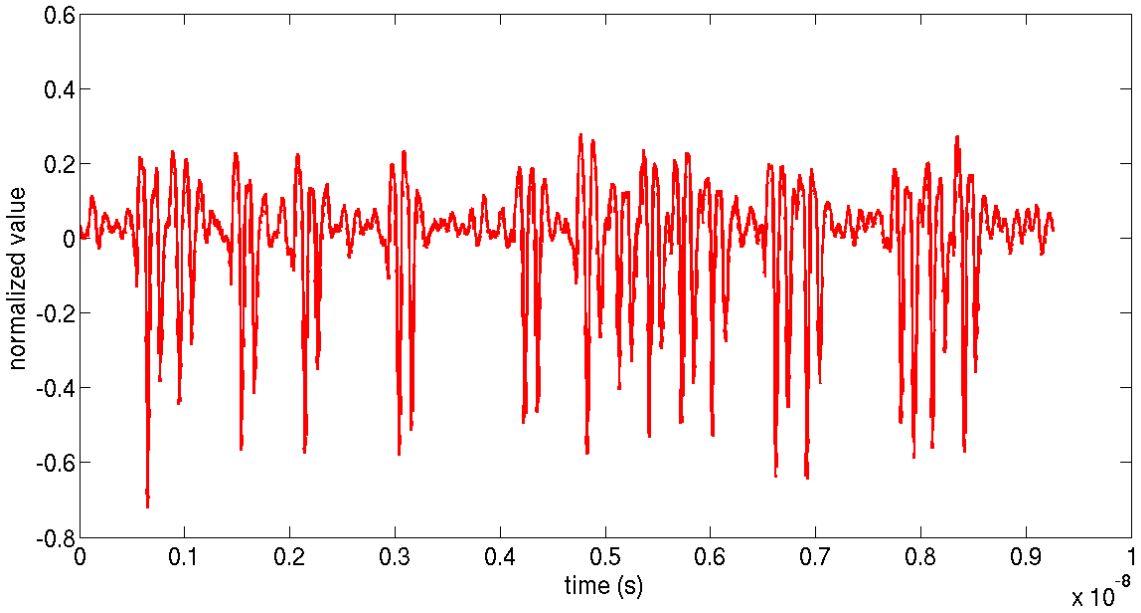

Figure 5.20: Reference 0 - 18GHz waveform sampled directly after frequency doubler, input is 31 bit prbs at 3.35 Gbps. x-axis is time and y-axis is normalized value

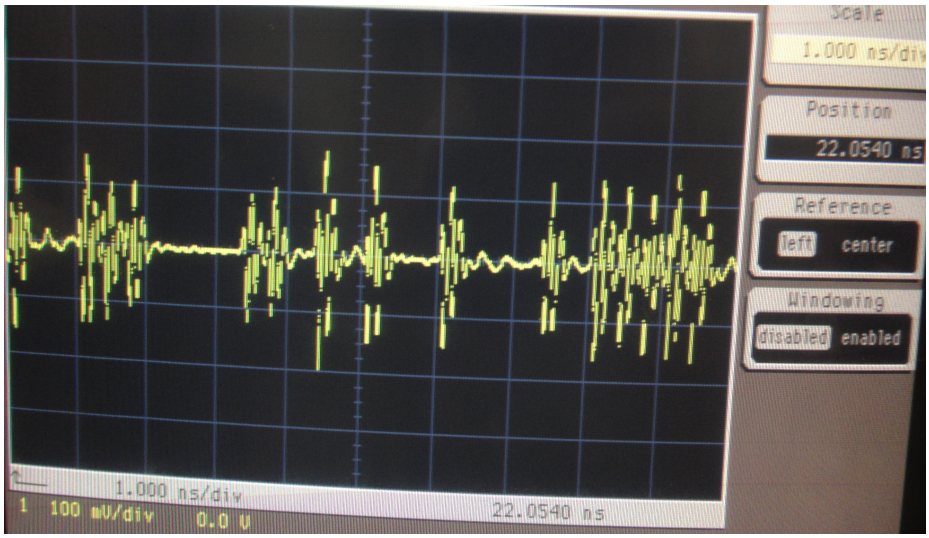

Figure 5.21: Reference waveform screen capture using sampling oscilloscope, input is 31 bit prbs at 3.35 Gbps. x-axis is time and y-axis is normalized value

directly acquired samples in Fig. 5.20. A screen image of the same waveform captured using a 40 GHz sampling scope is shown in Fig. 5.21. The delay mismatch is tuned manually for the best reconstruction. The input patters is 31 bit prbs at 3.35 Gbps passed through frequency doubler.

5.6.2 Tracking phase deviation in the input signal

To emulate the phase deviation in input signal in presence of small phase noise, the input signal from pattern generator was delay modulated with a triangular wave at 50 KHz and ±25 ps (peak) which is approximately equal to 0.167UI at 3.35 Gbps. The signal is then passed through a frequency doubler and high pass filter before being acquired through the mixer module using the proposed bandwidth interleaving technique. The phase delay is tracked using sliding windows in similar manner for the clock frequency modulation tracking as described in the chapter on the basic incoherent undersampling. The resultant extracted phase deviation is shown in Fig. 5.22. As can be seen from the figure that the

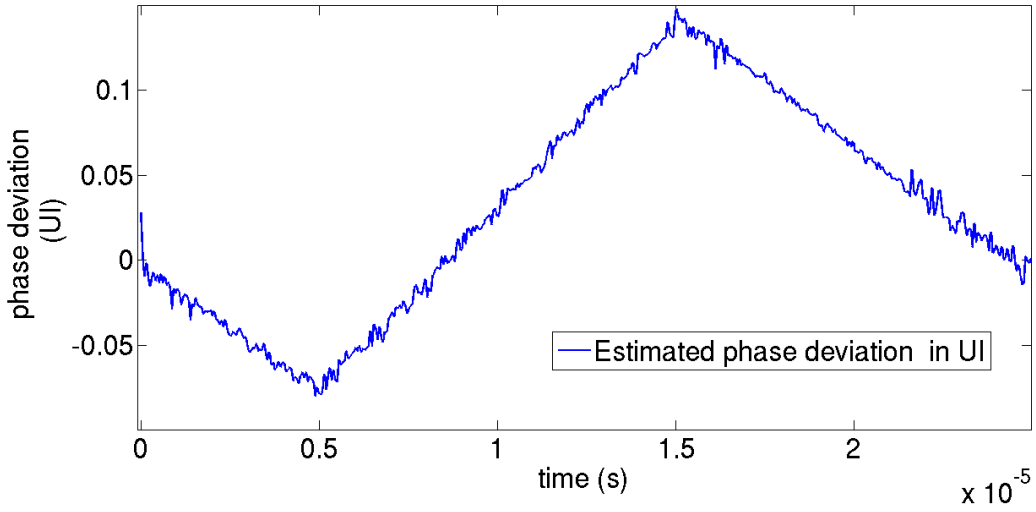

Figure 5.22: Estimated delay deviation

linearity of the phase deviation is maintained along with the peak-to-peak amplitude. This implies that if clean clocks (local clock and sampling clock) are available, the proposed technique can be used to measure close in phase noise.

5.7 Practical consideration: design of a power splitter

The proposed technique to extend the incoherent undersampling-based setup to beyond the track-and-hold bandwidth relies on the ability to divide the signal into multiple frequency bands without large distortions. If the bands are acquired separately, high-pass filters and low-pass filters can be used to acquire each bands. But in such cases the delay between

the bands become variable from run to run and needs to be calibrated in a blind estimation process from the acquired samples. Also it requires the data to be acquired over multiple runs and hence increases the data acquisition time significantly. In order to have an efficient system, it is necessary that the data is split into different frequency band using broadband power splitters for simultaneous digitization.

However, it must be mentioned that most broadband splitters are designed to work properly under a matched load conditions at all ports. But due to the nature of the load in a multi-band splitter, this is not the case. To understand this, one must recall that a filter in the stop-band usually presents (looking into the input of the filter) a reflective load and a matched load in the passband. Since in a multi-band splitter, the filters have pass bands in different frequency range, one of the ports of the broadband splitter is always terminated in a highly reflective load. One way of solving this problem would be to co-design and optimize the filters along with the splitter but this is not a practical solution.

A simpler solution is to terminate each output terminal of the splitter into a matched broadband buffer instead of feeding the filters directly. This ensures that the reflections form the filters in the stop-band do not reach the splitter terminals and hence do not affect the splitter performance. Besides the increased component count and complexity this technique also degrades the signal to noise ratio (SNR) due to the ultra-wide-band required of the buffers. It is also relevant here that buffers need not have any gain and hence can be obtained to span the whole bandwidth even when the track hold meets to cover the whole signal bandwidth requiring a multi-band solution in the first place.

5.8 Conclusions

In this chapter a technique for extending the bandwidth capability of a standard incoherent undersampling based technique was proposed. To maintain the cost advantage of the incoherent acquisition scheme, the system was designed to operate without any synchronization between the tester and the signal source. The signal components with frequency beyond the track-and-hold bandwidth were down-converted using a linear mixer. However such

mixing with incoherent local carrier leads to a loss of periodicity in the signal at the mixer output. To allow the application of simple time-domain reconstruction and period estimation a sampling strategy was developed to restore the periodicity of the acquired samples by sampling with a clock which is a sub-harmonic of the local oscillator.

Using the proposed setup, reconstruction of wide-band waveforms were demonstrated over multiple frequency bands. Also the possibility of using such a system for close in phase noise is demonstrated by showing that the phase of the reconstructed signal maintains a linear relationship with the input signal phase.

CHAPTER 6

SYSTEM SIMULATION FRAMEWORK FOR PERFORMANCE ASSESSMENT

6.1 Introduction

The principles of incoherent undersampling presented so far were developed for off chip test solutions. To make it more acceptable to the current on-chip test features, it is necessary to adopt these techniques to on-chip environment with a goal to improve the accuracy and coverage of the on chip test capability at the same time reducing the overhead. However to estimate the effectiveness of a sampling based system to detect faults and extreme parametric variations it is necessary to first develop a reasonably accurate and computationally efficient simulation framework. Such a framework is required to be able to promote deviations observed in waveforms at the block level through the hierarchy to a system level simulator, preserving the effects of the non ideal waveform across various time domain crossings.

Mixed signal systems, incorporating both digital and analog components, are hard to simulate. The analog blocks in the system require high resolution time domain simulation with detailed device models, while the digital systems work in the discrete time domain with finite levels. To reduce the simulation effort, simplified behavioral models of the system blocks are used with idealized waveforms. A major challenge in simulation of such systems is to reconcile the two distinct time domains : continuous-time analog vs discrete-time digital with latches and flip-flops at the domain crossing boundaries. A common approach to emulate such domain crossing is to model the latch as a perfect two valued quantizer, that compares the value of the input at a given (infinitely sharp) clock edge with a threshold and produces a digital output. While such simulation frameworks can provide reasonable accuracy for determining nominal timing margins in the system, they fail to capture the effects of noise and other non ideal behavior. This makes estimation of the effect of an observed deviation in the signal waveform at any of the inputs of the latch or

the clock signal at the system level a difficult proposition.

Inability to estimate the effects of non ideal waveforms in the analog domain on system performance severely limits the ability to fix design margins since one can not determine if a certain deviation can lead to a failure at the system level or can be observed by the test suite. To be able to accurately estimate such effects, we need a model that can take an initial probability distribution of the node voltages of the latch and evolve it through time to the end of a transient in the clock edge. Such a model is conceptually shown in Fig. 6.1. The inputs to such a model are the input waveforms $u(t)$, and clock waveforms

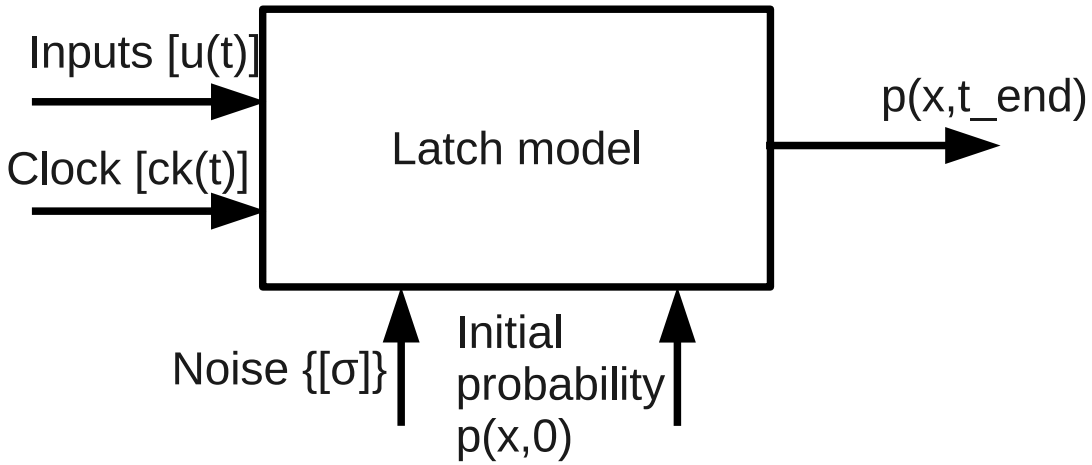

Figure 6.1: Conceptual diagram showing the proposed model

$ck(t)$ and an initial probability distribution $p(x,0)$ where x is the state space defined by the node voltages, and the noise power at the internal nodes $\{\sigma\}$. The model then integrates the effect of the noise through the clock edge transient in the metastable region of the latch and outputs the final probability distribution $p(x,t_{end})$. For practical reasons, the noise is assumed to be white noise. [59].

One way of solving such a problem is to do Monte-carlo simulations to simulate multiple scenarios in the presence of noise with a reduced order dynamic model. However a more efficient way is to obtain the associated deterministic equations for the evolution of the probability density from the reduced order dynamic model and vary it in time. In this work the latter approach is taken. A benefit of such an approach is considerable reduction

of the simulation effort.

Once the final probability density is calculated it can be used to evaluate the probability of a '1' or a '0' or an indeterminate state by integrating the probability density over appropriate regions of the state space. The given probability can then be used in the system simulation by building transition trees with each path having an associated probability. Branches in the trellis diagram can be dropped when the probability of a given branch falls below a certain predetermined threshold.

The main contributions of this work are:

- *Development of a new approach to dynamic modeling of latches for fast mixed-mode system simulation*
- *Development of a model that can incorporate both noise and non ideal input waveforms*
- *Proposing a new framework for simulation of digitally assisted analog systems*

The rest of the chapter is organized as follows: In section 6.2 summarizes the state of the art followed by a discussion of the theoretical basis of the proposed modeling approach in section 6.3. In section 6.5, we will take up a simple example and apply the proposed modeling technique to it. In section 6.6 results are presented followed by conclusions.

6.2 Motivation for new simulation flow

As mentioned before, the modeling of latch metastability dynamics is extremely important. However, most of the modeling till now has focused on determining the probability of a latch staying in the metastable state after a fixed time from an ideal clock transition. A simple model of a latched comparator is shown in Fig. 6.2. The non overlapping clock phases ϕ_1 and ϕ_2 alternatively switch the comparator between a tracking phase and a regenerative phase. In the tracking phase, the state of the internal nodes track the input setting an initial condition while in the regenerative phase the initial condition is resolved through

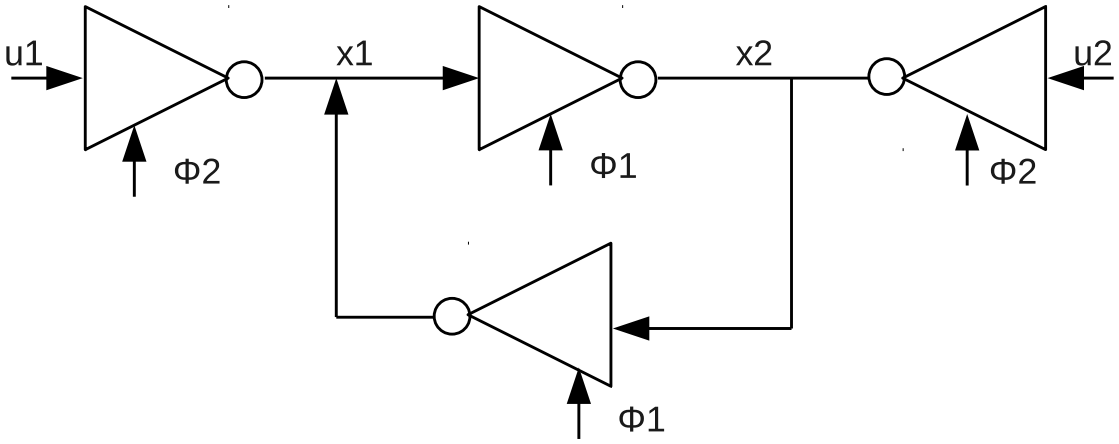

Figure 6.2: A simple latched comparator circuit

a metastable region into the final latch values. Most of the initial research on latch metastability modeled the regenerative inverters as linearized small signal trans-conductance with adequate capacitor loading at the output nodes. This treatment gives rise to a simple exponential growth model in the regenerative phase [36, 37]. In [38], the model was enhanced to account for the effects of miller capacitance. The linearized model is unable to track the voltage dynamics in the regenerative phase as the voltage grows large and hence the non-linear effects are ignored. In [40], the authors incorporated this non-linearity to improve the accuracy of the model. A very general analysis of latch dynamics was presented in [39].

However all the models mentioned so far are ideal in the sense that they neglect the effects of the noise or mismatch. One such study of the effect of mismatch on metastability dynamics was presented in [60]. More recently a probabilistic approach to explaining metastability in presence of noise is used. An error probability calculation using total input referred noise at the sampling clock was proposed in [41]. A linear time varying model was used to describe the basic underlying latch dynamics.

A more accurate modeling approach was proposed in [42]. In this research the behavior in the regenerative phase was accurately modeled by a stochastic dynamic equation (SDE) and the trajectory mean and standard deviation was calculated by integrating the SDE. A similar SDE based approach was also adopted in [43] and had the important observation

that a single point input referred noise may not be an accurate representation of the metastability. The general framework of that paper essentially was derived from that proposed in [44].

The present available approaches fail to model the effects of non ideal clock edges and input waveforms. Such effects are significant in high speed current mode logic (CML) circuits which are the logic family of choice for ultra high speed design due to their superior performance compared to other logic families. In this work a more general model of the regenerative phase of a latched comparator in presented using a SDE based approach. In order to capture the effects of non ideal clock edges, it is assumed that the inverter response is a general non-linear function of the state variables and the latch inputs. A more detailed discussion of the proposed model is presented in the next section.

The basic simulation flow proposed in this work can be represented using a flowchart as shown in Fig. 6.3. After simulating the components at transistor level, the data is used to identify a subspace of inputs for which the system level impact needs to be assessed. A reduced order model for the latch and other components downstream of the faulty component is obtained which agrees on the specific subspace of input waveforms using noiseless simulation at the SPICE level. After this the principal noise sources are identified and using this the SDE for the latch is obtained. From the SDE, theFokker-Planck equation (FPE) is obtained. Which is then solved to obtain the transition probabilities for the subspace of input waveforms. The transition probabilities thus obtained can then be used to determine how the top level system dynamics transition through the different digital states using a Markov chain based model [35].

6.3 Proposed model

The proposed model for simulating the transition behavior of a latch in the regenerative phase is shown in Fig. 6.4. It is a more generalized version of the model presented in Fig. 6.2.

The ideal switched inverters are replaced by more general nonlinear current functions

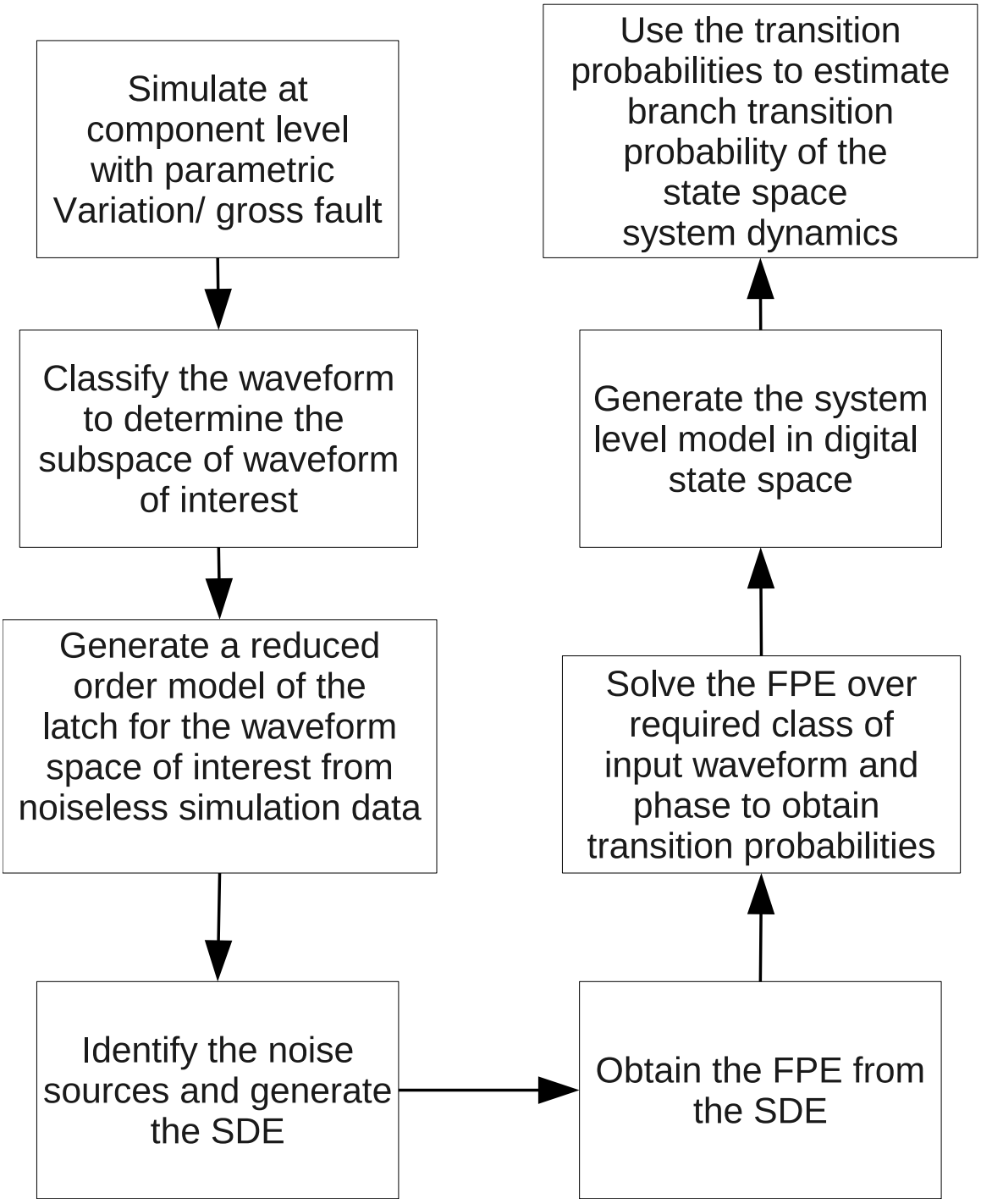

Figure 6.3: Flowchart describing the basic simulation flow to estimate impact of device level parametric variation and gross faults on the system level observables

$(g11, g12, g21, g22)$, which are dependent on the input, output and clock waveforms. It must be mentioned here that in the case of general nonlinear models for the current functions, simple closed form analytical solutions usually do not exist and the signal values

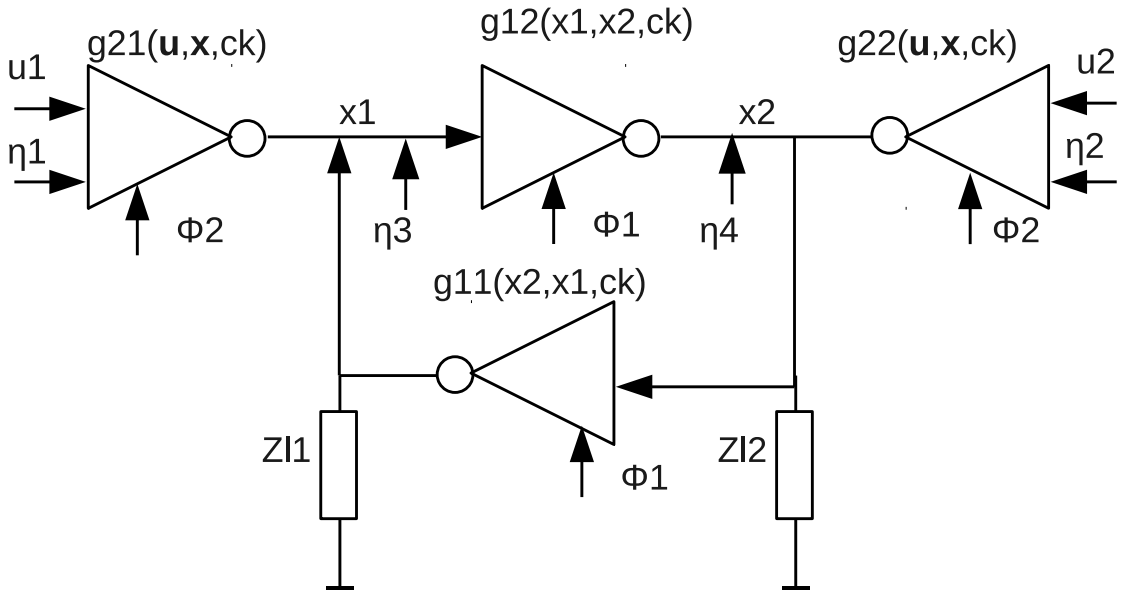

Figure 6.4: Improved latch model for simulation

must be calculated through numerical simulations. This implies that reduced order models for the current functions (g_{ij}) need to be constructed before simulation. Also, the reduced dimensional models may have inaccuracies and in those cases where higher accuracy is required, the state model needs be expanded to higher dimension, to include higher order derivatives.

The trans-conductance models themselves can be constructed by model order reduction from nominal simulations over the space of the observed input waveforms which includes the output obtained from simulation of the non ideal analog blocks. Techniques such as trajectory piece wise linear approach [33] and "mani-MOR"[34] can be used to build such models for higher accuracy requirement.

To further generalize, white noise sources, ($\eta_1, \eta_2, \eta_3, \eta_4$) are included. All the noise sources are assumed to be independent. The load impedances, (Z_{L1} and Z_{L2}) are modeled by a parallel combination of resistances (R_1 and R_2) and capacitances (C_1 and C_2) respectively.

Under these assumptions, the SDE governing the dynamics of the latch is given by:

$$\begin{aligned}
\mathrm{d}x_1 =& -\frac{1}{C_1}\left(g_{11}(x_2, x_1, ck) + g_{21}(u_1, x_1, ck) + x_1/R_1\right)\mathrm{d}t \\
&+ \mathrm{d}\eta_3 + \frac{1}{C_1}\frac{\partial g_{21}}{\partial u_1}(u_1, x_1, ck)\mathrm{d}\eta_1 \\
\mathrm{d}x_2 =& -\frac{1}{C_2}\left(g_{12}(x_1, x_2, ck) + g_{22}(u_2, x_2, ck) + x_2/R_2\right)\mathrm{d}t \\
&+ \mathrm{d}\eta_4 + \frac{1}{C_2}\frac{\partial g_{22}}{\partial u_2}(u_2, x_2, ck)\mathrm{d}\eta_2
\end{aligned} \tag{6.1}$$

If required, noise sources can also be considered in the clock ck, by using a first order perturbation about ck. In order to solve the set of SDE given in 6.1, numerically, a large numerical effort is required. Instead of solving the set of dynamic equation directly it is computationally more manageable to solve for the evolution of probability density function (PDF) in the state space. The dynamics of the evolution of the PDF is given by the FPE [59]. For the model under consideration, the FPE can be written as:

$$\begin{aligned}
\frac{\partial p(x_1, x_2, t)}{\partial t} =& \frac{\partial}{\partial x_1}(\mu_1 p(x_1, x_2, t)) + \frac{\partial}{\partial x_2}(\mu_2 p(x_1, x_2, t)) \\
&+ \sum_{i=1}^{4} \sigma_i^2 \frac{\partial^2}{\partial x_i^2} D_{ii} p(x_1, x_2, t)
\end{aligned} \tag{6.2}$$

where,

$$\begin{aligned}
\mu_1 =& \frac{1}{C_1}\left(g_{11}(x_2, x_1, ck) + g_{21}(u_1, u_2, x_1, x_2, ck) + x_1/R_1\right) \\
\mu_2 =& \frac{1}{C_2}\left(g_{12}(x_1, x_2, ck) + g_{22}(u_2, u_1, x_2, x_1, ck) + x_2/R_2\right) \\
D_{11} =& D_{22} = 1 \\
D_{33} =& \left(\frac{1}{C_1}\frac{\partial g_{21}}{\partial u_1}(\bar{u}, \bar{x}, ck)\right)^2 \; D_{44} = \left(\frac{1}{C_2}\frac{\partial g_{22}}{\partial u_2}(\bar{u}, \bar{x}, ck)\right)^2
\end{aligned} \tag{6.3}$$

and $< \mathrm{d}\eta_i^2 >= \sigma_i^2 \mathrm{d}t$ is the power spectral density of the noise. For more diverse noise sources with mutual correlation, the term in second order spatial derivatives would be :

$$\sum_{i=1}^{4} \sigma_i \sigma_j r(i, j) \frac{\partial^2}{\partial x_i \partial x_j} D_{ij} p(x_1, x_2, t) \tag{6.4}$$

where, $r(i, j)$ is the correlation coefficient of the noise sources indexed i and j respectively, with D_{ij} being the appropriate coupling term for example for noise source 3 and 4 the cross

term will be,

$$D_{34} = \frac{\partial g_{21}}{\partial u_1}(\bar{u}, \bar{x}, ck)\frac{\partial g_{22}}{\partial u_2}(\bar{u}, \bar{x}, ck)$$

The equation has two parts, a drift part with first order spatial derivatives which represent the noise free dynamics of the system and a diffusion part which represents the scattering effects of the noise. In the general nonlinear case, the FPE does not have a closed form analytical solution. Which means that the equation should be solved numerically. Solving the FPE explicitly reduces the error in estimation since it can handle cases where the final pdf is not necessarily a Gaussian and also inherently accounts for the effects of non ideal input and clock waveforms. For a numerical solution of the FPE, the trans-conductance functions used need not be expressed in closed form and can be defined only at discrete points in the state space, with piece wise smooth, continuous function. The values at the intermediate points can be calculated using interpolation techniques.

The initial condition can be set from the solution at the end of a previous clock cycle or by assuming a pure '1' or '0' state as a Dirac delta function $p(x_1, x_2, 0) = \delta(x_1 - 1, x_2)$ and $p(x_1, x_2, 0) = \delta(x_1, x_2 - 1)$ respectively. Once the numerical solution of the FPE is obtained by solving (6.2) using the initial condition $p(x_1, x_2, 0)$ up to the end of the available time (t_{avl}), the PDF can be integrated to obtain the probability of a '1' or a '0' as

$$P(1) = \int_{V_{ss}}^{V_{th,l}} p(x_1, x_2, t_{avl})\mathrm{d}x_1 \tag{6.5a}$$

$$P(0) = \int_{V_{th,h}}^{V_{dd}} p(x_1, x_2, t_{avl})\mathrm{d}x_1 \tag{6.5b}$$

Where $V_{th,h}$ and $V_{th,l}$ represent the high and low logic threshold. Once the probabilities in (6.5) are known they can be used to construct the trellis diagram for the digital finite state machine. The proposed simulation framework thus allows one to promote the effects of non ideal response at the analog blocks through the continuous time - discrete time domain crossing and evaluate the effects at a system level.

6.4 Choice of numerical solver

Since the PDF in simulation behaves as a compressible fluid and the dynamics has a steady state, sharp accumulation and gradients in PDF can form during the simulation. Hence the numerical solver should be able to preserve sharp gradients in the PDF. Such problem regularly arises in fluid dynamics simulation where shock fronts can form and solvers commonly used for hyperbolic equations can maintain numerical stability in presence of such shock fronts. This problem is popularly known as the Riemannian problem where a sharp gradient in the fluid density is propagated in a velocity field. Straight forward finite difference based and weak formulation based techniques used for solving elliptic equations usually produce too much numerical dispersion and causes smearing of edges and or oscillation instability in solving hyperbolic equations. While characteristic based Riemannian solvers are highly accurate in solving such problems, it is costly to implement them.

Approximately accurate modified central finite differencing schemes [61, 62, 63] have been proposed which can solve the hyperbolic problem with low numerical dispersion and good stability performance. This techniques are simple to implement and are independent of the eigenstructure of the problem and hence can be easily applied to a wide range of problems. Due to the inherent simplicity and universal nature of the central differencing based solvers is chosen for the example problem.

In the next section the concepts presented are applied to a CML latch model.

6.5 Example: CMOS CML latch modeling

In this section the concepts from section 6.3, are used to simulate a CML latch as an example. The basic CML latch circuit is shown is Fig. 6.5. For simplicity it will be assumed that the circuit has no mismatch and that the noise on the two nodes have equal power density and is small. This implies that the circuit will operate under differential conditions and the time varying part of the common mode signal given by $V_{cm} = \frac{1}{2}(x_1 + x_2)$ will be small. This makes it feasible to consider the ac component of the signal by removing the dc common mode, and considering the excursion of x_1 and x_2 about this dc value.It is also assumed

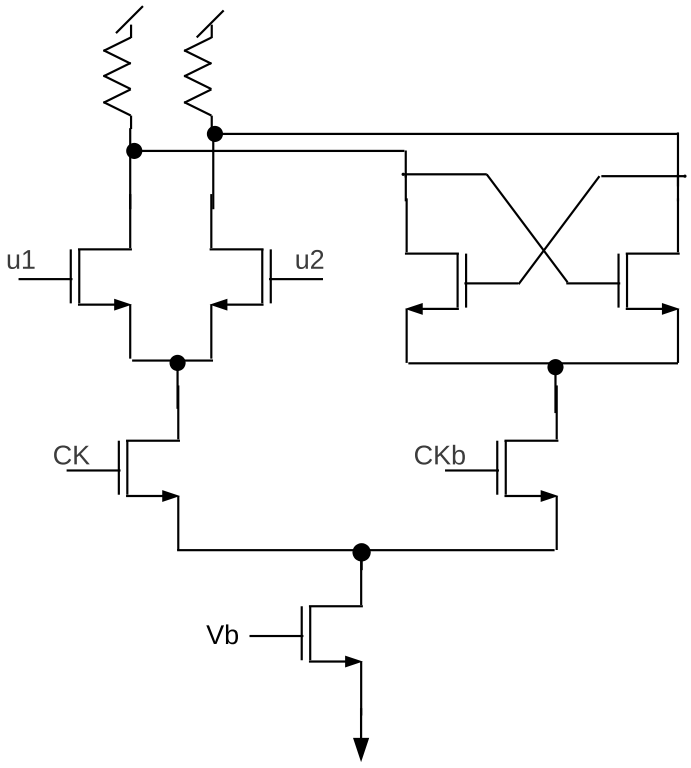

Figure 6.5: Schematic of a CML latch

that the output impedance of all the transistors can be neglected in comparison with the individual drain loads.

Also the total current is limited by design to I_{tot}. The clock signal controls how much of this current flows in the buffer and the rest goes into the regenerative pair. Again neglecting the common mode of the clock signal, and considering only the differential mode of the clock signal *ck*, we can write,

$$\begin{aligned} I_{buf} &= s_1(ck) I_{tot} \\ I_{reg} &= (1 - s_1(ck)) I_{tot} \end{aligned} \tag{6.6}$$

for the two branches of the current with $s_1(ck)$ being the shaping function representing transfer characteristics of the differential pair driven by the clock. It varies from 0 to 1 as clock waveform varies from $-V_{ck}$ to $+V_{ck}$ and shows saturation at both ends with linear dependence for small signal values. The linear trans-conductance of the differential pair

for small inputs being equal to:

$$gm_{ck,lin} = \sqrt{2k_n(\frac{W_c}{L_c})\frac{I_{tot}}{2}}$$

where, k_n is a technology parameter and W_c and L_c are the width and length of the switching CMOS transistors. A simple choice for such a shaping function could be a raised cosine edge as:

$$s_1(ck) = \begin{cases} 0 & ck \leq -V_{ck} \\ 0.5\left(1 - cos\left(\pi\frac{ck+V_{ck}}{2V_{ck}}\right)\right) & |ck| \leq V_{ck} \\ 1 & ck \geq V_{ck} \end{cases}$$

with,

$$gm_{ck,lin} = \frac{\pi}{4V_{ck}} I_{tot}$$

or,

$$V_{ck} = \frac{\pi}{4\left(\frac{gm}{I_{tot}}\right)} = \frac{\pi}{2\left(\frac{gm}{I_{d,bias}}\right)} \tag{6.7}$$

For the upper differential pair driven by the inputs, the tail current is limited to I_{buf}. The differential voltage $u_1 - u_2$ causes the current to commute between the x_1 and the x_2 nodes. For small values of differential inputs, the linear trans-conductance for each branch is given by:

$$gm_{buf,lin} = \sqrt{2k_n(\frac{W}{L})\frac{I_{buf}}{2}}$$

so that the current for the two branches are given by:

$$i_{1,buf} = gm_{buf,lin} * (u_1 - u_2)/2$$

$$i_{2,buf} = gm_{buf,lin} * (u_2 - u_1)/2$$

However for large inputs, maximum current commutation occurs and the current in each branch is limited to $\pm\frac{I_{buf}}{2}$. The saturation occurs as the input voltage becomes comparable to :

$$(u_1 - u_2)/2 \approx \frac{I_{buf}/2}{gm_{buf,lin}}$$

or,

$$|u_1 - u_2| \approx \sqrt{\frac{I_{buff}}{k_n(\frac{W}{L})}}$$

For this example the slope discontinuity is smoothed out by using a moving average filter. A more exact model can be easily reconstructed by plotting the output current vs the input voltage as the tail current is varied from an exact simulation. The equations for the regenerative circuit is similar with u_1 and u_2 replaced by x_2 and x_1 respectively. For the regenerative branch we can write:

$$gm_{reg,lin} = \sqrt{2k_n(\frac{W}{L})\frac{I_{reg}}{2}}$$
$$i_{1,reg} = gm_{reg,lin} * (x_2 - x_1)/2$$
$$i_{2,reg} = gm_{reg,lin} * (x_1 - x_2)/2$$

The current in each branch being limited to $\pm\frac{I_{reg}}{2}$ with saturation applied to the input,

$$|x_2 - x_1| \approx \sqrt{\frac{I_{reg}}{k_n(\frac{W}{L})}}$$

Again smooth transition between the linear and the saturation regimes is obtained by applying a moving average filter to the i-v transfer characteristics.

For the noise perturbation a direct equivalent noise excitation at the output nodes x_1 and x_2 is added with an average power of σ. The other noise voltages are neglected for this example. Also the parallel R and C is assumed as a load at each of the output nodes. So the SDE governing the dynamics can be written as:

$$\begin{aligned} \mathrm{d}x_1 &= -\frac{1}{C}\left(i_{2,buf} + i_{2,reg} + \frac{x_1}{R}\right)\mathrm{d}t + \sigma \mathrm{d}\eta_1 \\ \mathrm{d}x_2 &= -\frac{1}{C}\left(i_{2,buf} + i_{2,reg} + \frac{x_2}{R}\right)\mathrm{d}t + \sigma \mathrm{d}\eta_2 \end{aligned} \tag{6.8}$$

so the relevant FPE is given as:

$$\begin{aligned}\frac{\partial p}{\partial t} =& \frac{\partial}{\partial x_1}\frac{1}{C}\left(i_{2,buf} + i_{2,reg} + \frac{x_1}{R}\right)p \\ &+ \frac{\partial}{\partial x_2}\frac{1}{C}\left(i_{2,buf} + i_{2,reg} + \frac{x_2}{R}\right)p \\ &+ \sigma^2\left(\frac{\partial^2}{\partial x_1^2} + \frac{\partial^2}{\partial x_2^2}\right)p \end{aligned} \tag{6.9}$$

6.6 Simulation Results

For the simulation, realistic values for a 180 nm CMOS technology are used, from a reference design designed to work at 10 Gbps. The I_{tot} is taken to be 3.9 mA and the operating point of the transistors are taken to be such that ratio of trans-conductance to quiescent drain current is $\frac{gm}{I_d} = 4$ for the clock switching transistors and $\frac{gm}{I_d} = 3$ for the differential pairs for both the buffer and the regenerative transistors for the maximum tail current condition. The load resistance is taken to be $R = 200\Omega$ and load capacitance $C = 90fF$. The resultant current curves with varying clock voltage is shown in Fig. 6.6. The FPE is a con-

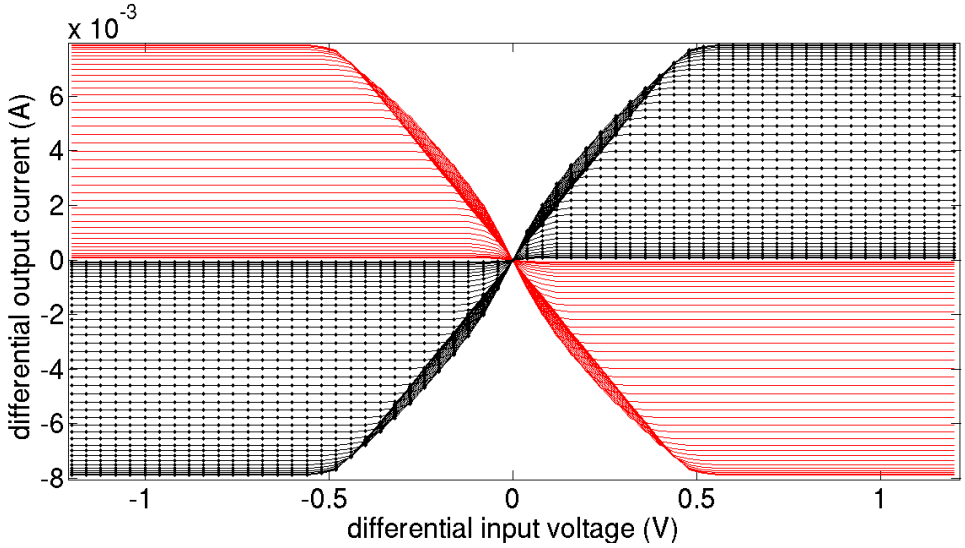

Figure 6.6: Output current vs voltage for the differential pair with varying clock drive

servation law for the probability density function. Also the model calls for possibility of sharp edges (e.g. asymptotically stable state trajectories). Hence a high accuracy scheme with low numeric dissipation should be used. A good choice for such a system are the

"monotone upstream-centered schemes for conservation laws"(MUSCL) based schemes. The semi-discrete formulation proposed by Kurganov and Tadmor [63] is used for each direction. For the time integration a forward Euler integration is used. The proposed scheme is a semi-discrete version of the monotone upstream-centered schemes for conservation laws(MUSCL) scheme. In the present case a piecewise linear MUSCL reconstruction is used with maximum spectral radius of the local advection velocity as the flux. That is, the spatial derivatives are centered on the cell and approximated as:

$$\frac{\partial F_i}{\partial x} \approx \frac{F_{i+\frac{1}{2}} - F_{i-\frac{1}{2}}}{\Delta x}$$

where,

$$F_{i-\frac{1}{2}} = \frac{1}{2}\left\{\left[F(u^R_{i-\frac{1}{2}}) + F(u^L_{i-\frac{1}{2}})\right] - a_{i-\frac{1}{2}}\left[u^R_{i-\frac{1}{2}} - u^L_{i-\frac{1}{2}}\right]\right\}$$
$$F_{i+\frac{1}{2}} = \frac{1}{2}\left\{\left[F(u^R_{i+\frac{1}{2}}) + F(u^L_{i+\frac{1}{2}})\right] - a_{i+\frac{1}{2}}\left[u^R_{i+\frac{1}{2}} - u^L_{i+\frac{1}{2}}\right]\right\}$$

the local propagation velocities being given by,

$$a_{i\pm\frac{1}{2}} = max\left[\rho\left(\frac{\partial F(u_i)}{\partial u}\right), \rho\left(\frac{\partial F(u_{i\pm1})}{\partial u}\right)\right] \tag{6.10}$$

ρ being the spectral radius of the respective Jacobian

u^R and u^L are the left and right piecewise linear MUSCL reconstruction at the half grid points. The diffusion operator is approximated as :

$$\frac{\partial^2 p_{i,j}}{\partial x^2} + \frac{\partial^2 p_{i,j}}{\partial y^2} = \frac{1}{4\Delta x^2}\left[p_{i-1,j} + p_{i+1,j} + p_{i,j-1} + p_{i,j+1} - 4p_{i,j}\right] \tag{6.11}$$

Due to the small accuracy of the forward Euler integration the time step is chosen to be 2 orders of magnitude smaller than that required by the CFL condition for stability.

To demonstrate the capability of the technique a sinusoidal input and a finite slew clock is used. The clock and the signal waveform are shown in Fig. 6.7. It is simulated with an

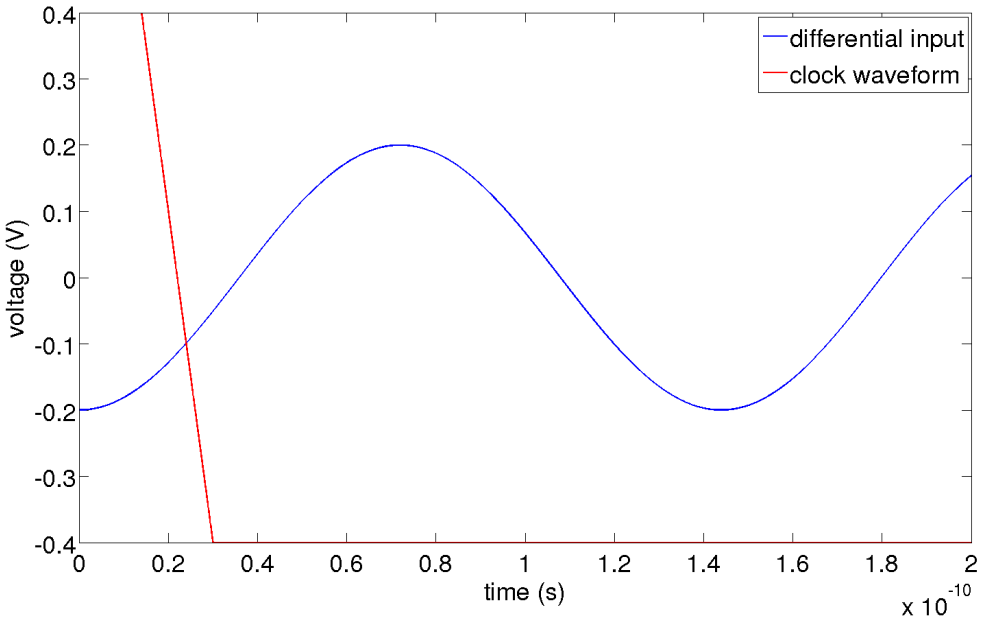

Figure 6.7: The clock and input waveform

initial condition for the probability density away from metastability and evolve it in time without noise first. The results are shown in Fig. 6.8. The probability contours of the same

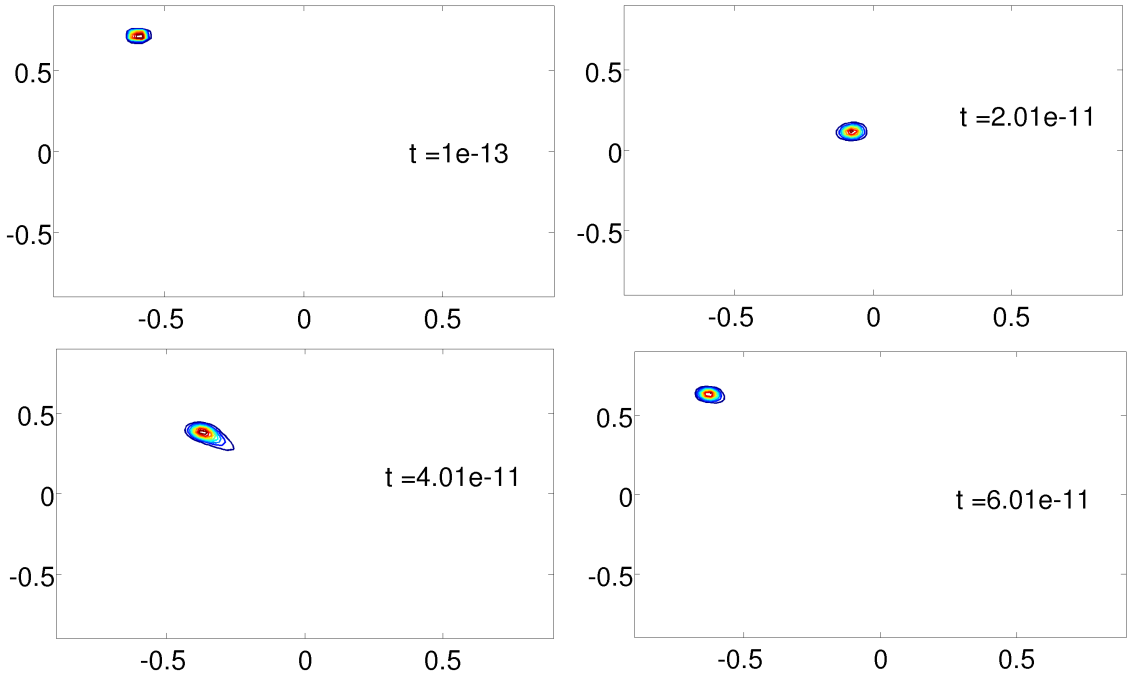

Figure 6.8: Contour plot of evolution of probability through time in absence of noise at 0, 20ps, 40ps and 60ps; x and y axes represent the two states of the system

dynamics with noise is shown in Fig. 6.9. It can be seen that in presence of noise there is a distinct probability of both p(1) and p(0). It is also evident that in presence of noise the probability distribution is no longer a unimodal Gaussian distribution and hence earlier techniques may not be valid. The integrated probabilities after settling down are given by integrating the probability solution as $P(1) = 0.19$ and $P(0) = 0.81$.

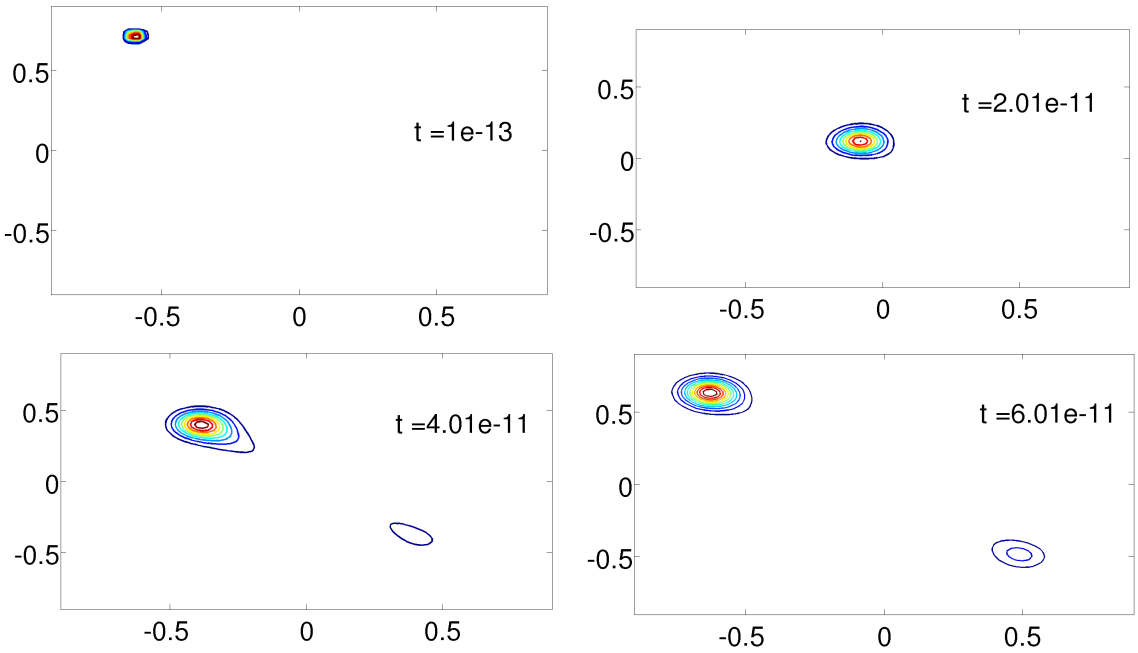

Figure 6.9: Contour plot of evolution of probability through time with noise at 0, 20ps, 40ps and 60ps; x and y axes represent the two states of the system

The variation of transition probability phases for the four phases as we sweep the clock over a period of 1010... data (two clock period), is shown in Fig. 6.10.

6.6.1 Application to system simulation : example

The above model is applied to simulate the dynamics of a clock phase recovery loop using a binary phase detector following the Markov chain based method proposed in [35]. This can be used in systems where a data clock is forwarded over long traces ans accumulate phase skew. To correct the phase skew a phase rotator based system can be used to acquire the clock phase as shown in Fig. 6.12. The signal is sampled at three phases early(e), center(c) ,and late(l) separated by half the clock period as shown in Fig. 6.13. The state machine is

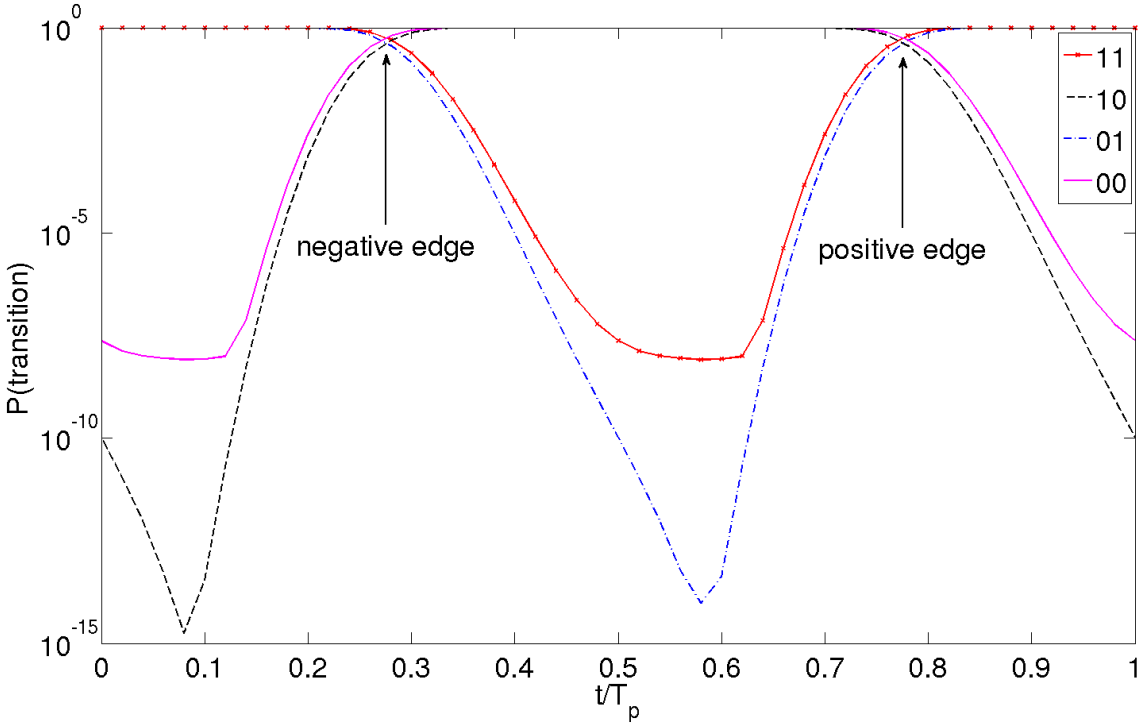

Figure 6.10: Probability of transition as the sampling phase is varied over a 1-0-1 transition period

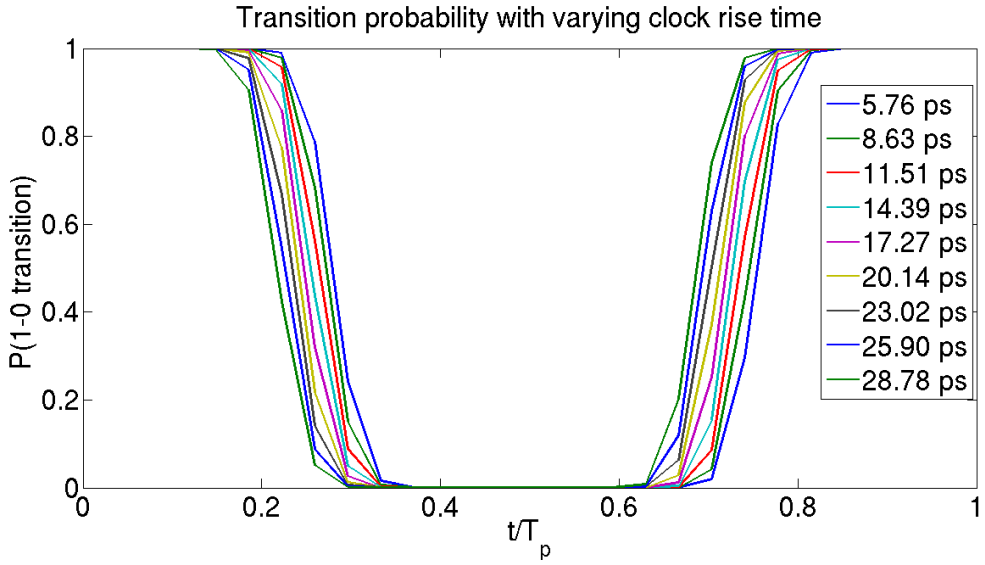

Figure 6.11: Probability of transition as the sampling phase is varied over a 1-0-1 transition period as the clock edge rise time is varied

described as:

$$\phi \leftarrow \phi + 1 \quad \text{if} \quad [e,c,l] == 110\, or\, 001$$

$$\phi \leftarrow \phi - 1 \quad \text{if} \quad [e,c,l] == 100\, or\, 011 \tag{6.12}$$

where ϕ is the index of discrete phase (offset) state that the system can be in. The corresponding state transition diagram is shown in Fig. 6.14.

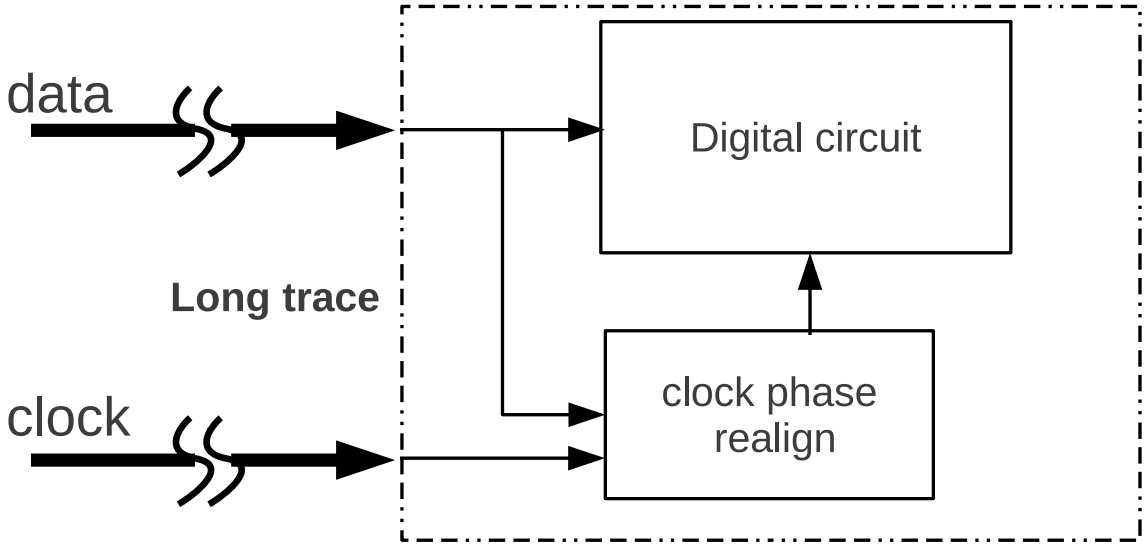

Figure 6.12: When clock and data are transmitted over long traces the clock phase can accumulate skew which needs to be corrected using phase realignment

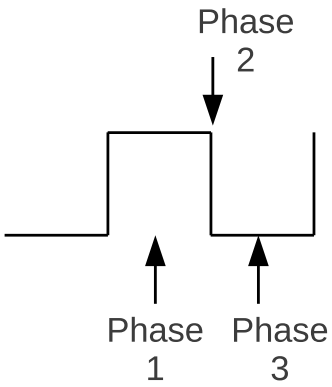

Figure 6.13: The phase detector detects the clock phase offset by sampling at three phases and detecting whether the transition is between the phases 1,2 (clock phase lagging) or between the phases 2,3 (clock phase leading)

The incoming data will have a finite transition probability given by $p(+_e)$ and $p(-_e)$ for positive and negative transition probabilities from a 0 and a 1 respectively. The steady state

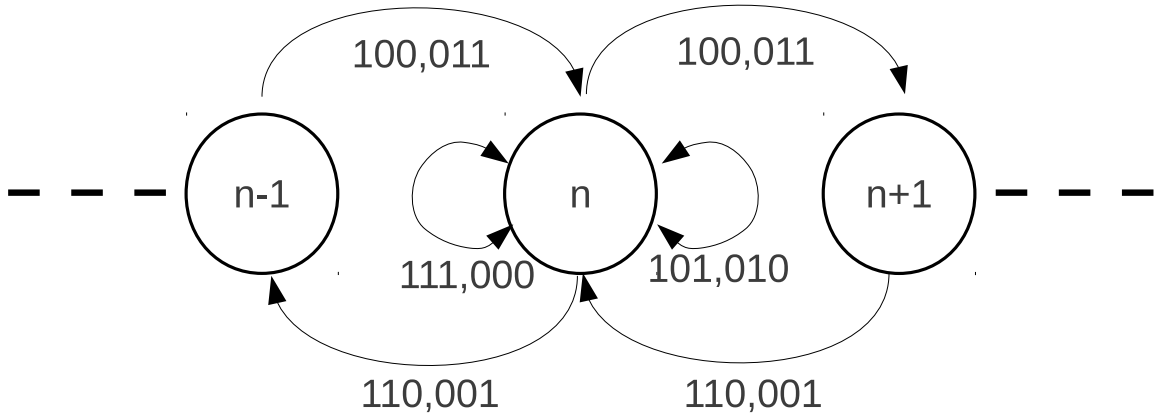

Figure 6.14: State transition diagram of a binary phase detector based clock recovery

mark density of the data must then be given by:

$$p_{data}(1) = \frac{p(+_e)}{p(+_e) + p(-_e)}$$
$$p_{data}(0) = \frac{p(-_e)}{p(+_e) + p(-_e)}$$

For a random data stream usually, $p(+_e) = p(-_e) = 0.5$. The phase noise performance of the system will be given by the array of numbers $p(+_e/\ -_e\ /n_e, \phi, 1/0)$. Where $p(+_e/\ -_e\ /n_e, \phi, 1/0)$ gives the probability of the center latch to be at an offset ϕ from the ideal edge position when a positive edge $(+_e)$ or a negative edge $(-_e)$ or no edge is present and the output is a 1 or a 0. From the simulation of the metastability the transition probabilities $p(+_e/\ -_e\ /n_e, \phi, \{00, 01, 10, 11\})$ will be obtained. Where, $p(+_e/\ -_e\ /n_e, \phi, \{00, 01, 10, 11\})$ gives the probability of a $\{00, 01, 10, 11\}$ transition at an offset ϕ from the ideal edge position when a positive edge $(+_e)$ or a negative edge $(-_e)$ or no edge is present. In the next set of equations, the following shorthand expression is used for transition probabilities, with d_1, d_2 or d_3 being 1's or 0's.

$$\{d_1 d_2 d_3 - d_1' d_2' d_3'\} \equiv p(e, \phi_e, \{d_1 d_1'\}) p(e, \phi_c, \{d_2 d_2'\}) p(e, \phi_l, \{d_3 d_3'\})$$

The dynamics of the state probabilities neglecting drift due to clock phase noise is given

by the following set of equations written in compact form:

$$
\begin{aligned}
p^n(e,\phi,d_1d_2d_3) = \Big[& p^{n-1}(ne,\phi,111)\{111-d_1d_2d_3\} + p^{n-1}(ne,\phi,010)\{010-d_1d_2d_3\} \\
& + p^{n-1}(ne,\phi,101)\{101-d_1d_2d_3\} + p^{n-1}(ne,\phi,000)\{000-d_1d_2d_3\} \\
& + p^{n-1}(ne,\phi-\delta\phi,011)\{011-d_1d_2d_3\} + p^{n-1}(ne,\phi-\delta\phi,100)\{100-d_1d_2d_3\} \\
& + p^{n-1}(ne,\phi+\delta\phi,110)\{110-d_1d_2d_3\} + p^{n-1}(ne,\phi+\delta\phi,001)\{001-d_1d_2d_3\}\Big]\, p(ne|e) \\
& + \Big[p^{n-1}(+_e,\phi,111)\{111-d_1d_2d_3\} + p^{n-1}(+_e,\phi,010)\{010-d_1d_2d_3\} \\
& + p^{n-1}(+_e,\phi,101)\{101-d_1d_2d_3\} + p^{n-1}(+_e,\phi,000)\{000-d_1d_2d_3\} \\
& + p^{n-1}(+_e,\phi-\delta\phi,011)\{011-d_1d_2d_3\} + p^{n-1}(+_e,\phi-\delta\phi,100)\{100-d_1d_2d_3\} \\
& + p^{n-1}(+_e,\phi+\delta\phi,110)\{110-d_1d_2d_3\} + p^{n-1}(+_e,\phi+\delta\phi,001)\{001-d_1d_2d_3\}\Big]\, p(+_e|e) \\
& + \Big[p^{n-1}(-_e,\phi,111)\{111-d_1d_2d_3\} + p^{n-1}(-_e,\phi,010)\{010-d_1d_2d_3\} \\
& + p^{n-1}(-_e,\phi,101)\{101-d_1d_2d_3\} + p^{n-1}(-_e,\phi,000)\{000-d_1d_2d_3\} \\
& + p^{n-1}(-_e,\phi-\delta\phi,011)\{011-d_1d_2d_3\} + p^{n-1}(-_e,\phi-\delta\phi,100)\{100-d_1d_2d_3\} \\
& + p^{n-1}(-_e,\phi+\delta\phi,110)\{110-d_1d_2d_3\} + p^{n-1}(-_e,\phi+\delta\phi,001)\{001-d_1d_2d_3\}\Big]\, p(-_e|e)
\end{aligned}
\tag{6.13}
$$

where, $p(\{ne/+_e/-_e\}|e)$ is the probability that in the last clock cycle, there was were no edge or a positive edge or a negative edge given that the current clock there is a edge of type e respectively. The phase noise of the clock will be given by the steady state solution of the equation (6.13) obtained by setting $p^n(.) = p^{n-1}(.)$. Also, $p(e,\phi,d) = p(d|e,\phi)p(e)p(\phi)$, and $p(e,\phi,d_1d_2d_3) = p(d_1|e,\phi-\pi)p(d_2|e,\phi)p(d_3|e,\phi+\pi)p(e)p(\phi)$ Now it can be assumed that the state space of the PLL is divided into $4N$ discrete phases. For each of the index c, the transition probabilities can be evaluated as:

$$
\begin{pmatrix}
p^c\{0,0\} & p^c\{1,0\} \\
p^c\{0,1\} & p^c\{1,1\}
\end{pmatrix}
$$

by using the proposed model starting with appropriate initial condition. It is also worth mentioning that the the transition probabilities are independent of time as long as the input and clock waveforms remain same. Once the transition probabilities are evaluated, the

expression in (6.13) can be used to evaluate the trellis diagram of the state transition after each time period. The mode and standard deviation of the phase dynamical behavior starting from a point initial condition is shown in Fig. 6.15 and Fig. 6.16.

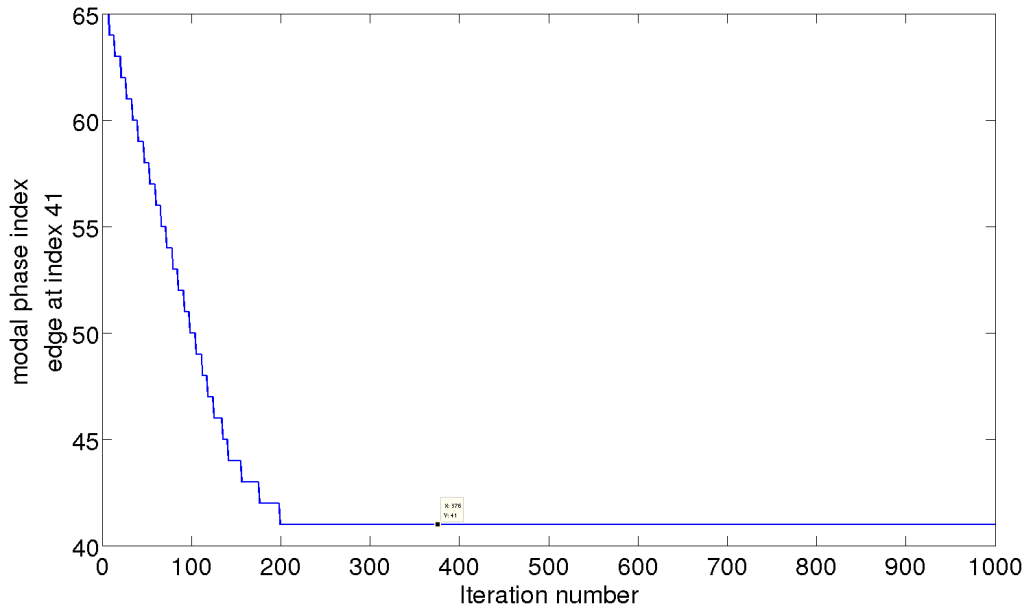

Figure 6.15: Simulated system dynamical behavior of the standard deviation of phase starting from a point initial condition around phase index 65 with the edge located at index 41

6.7 Conclusions

A novel technique of modeling latches that can emulate the effect of non-ideal input and clock waveforms is proposed. The technique first relies on deriving the reduced order noise free model of the latch followed by the inclusion of noise effects in the form of a stochastic differential equation. From the SDE the FPE is derived for the probability density evolution in time. The FPE is then solved numerically to derive the appropriate transition probabilities. Which can be then used to evaluate a state dynamics of a discrete time digital system that is excited by the output of the latch. An example is provided with a qualitative analysis of a CMOS latch and how it can be adapted to a system simulation. This can lead to significant improvement in time and accuracy in simulating systems with both continuous time and discrete time components.

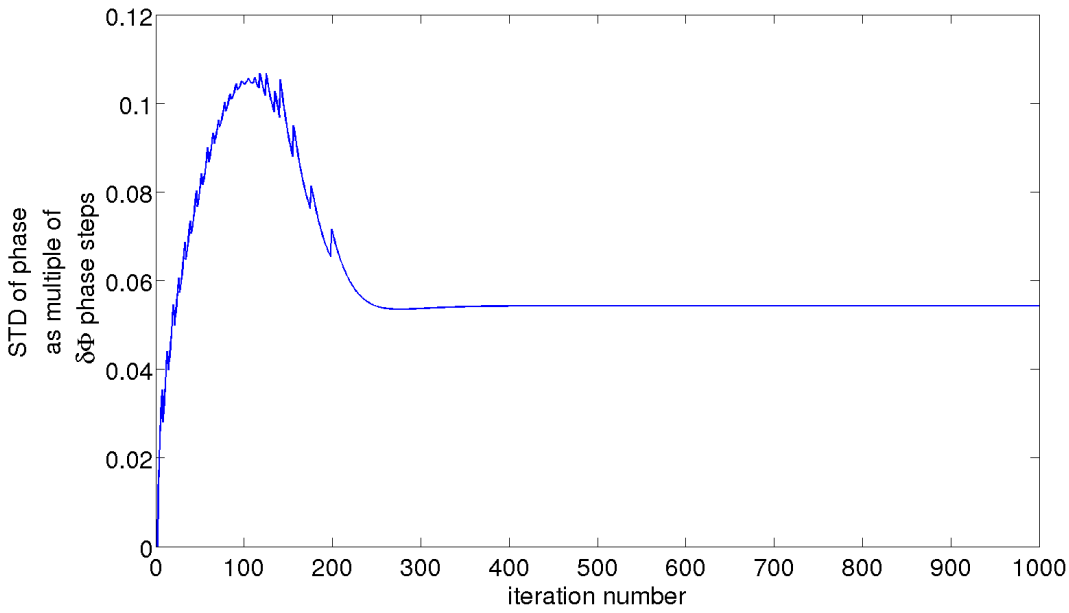

Figure 6.16: Simulated system dynamical behavior of the standard deviation of phase starting from a point initial condition

CHAPTER 7

CONCLUSIONS AND FUTURE DIRECTIONS

This thesis presents algorithms and a methodology for low complexity, robust high-speed waveform acquisition. The proposed techniques are based on an incoherent (trigger-free) undersampling framework for periodic waveform acquisition. Incoherent undersampling-based techniques reduce the cost of test hardware, by addressing the two main aspects affecting the test equipment cost.

First, using undersampling reduces the number of analog to digital conversion per second. This leads to a relaxation of the specifications and hence a reduction in the cost of the analog to digital converter (ADC). It is costly to design an ADC for Nyquist rate sampling of high-frequency signals, and undersampling is the only efficient way to acquire wide-band signals. In undersampling-based waveform acquisition systems, the only wide-band component required is the track-and-hold amplifier used for sampling at a reduced rate compared to the Nyquist rate, and the ADC conversion rate is reduced.

The second cost saving aspect of incoherent undersampling arises from the use of a trigger-free setup which does not require any precise phase synchronization between the tester and the signal source. This makes the system insensitive to unmatched delays in various parts of the test equipment and thus reduces the cost and improves the accuracy of the system.

As a further improvement over the classical waveform acquisition setup proposed previously, the computation cost in the back-end algorithm is reduced by developing a low-cost time-domain metric for period estimation. The metric, which is based on the number of zero crossings in the reconstructed waveform, can be used to estimate the waveform period from the acquired samples in a blind manner with significant improvement in the computational complexity compared to the corresponding spectral domain techniques.

As mentioned before, the classical incoherent undersampling-based system requires a wide-band track-and-hold amplifier which poses a barrier to the frequency scaling of the

system. However, this research demonstrates a multi-band signal acquisition technique to extend the bandwidth of the incoherent undersampling-based setup, beyond the track-and-hold bandwidth, which extends the maximum bandwidth of the system by using relatively narrow band mixers to down convert the signal waveform components with frequencies beyond those of the track-and-hold amplifier bandwidth, followed by incoherent undersampling. The basic architecture is an adaptation of the well known hybrid filter bank technique to an incoherent undersampling-based framework. The incoming signal is split into multiple frequency bands of relatively smaller bandwidth. The signal in each band is then down converted by mixing with an incoherent (no synchronization with the signal source) local oscillator tone, followed by undersampling. The process of mixing with an incoherent local oscillator tone leads to a loss of periodicity at the mixer output, leading to a slight increase in complexity of the reconstruction algorithm. However, the periodicity can be restored by sampling with a clock that has a period equal to an integer multiple of the local oscillator clock period, thus permitting the use of low-complexity time-domain reconstruction techniques.

The applicability of the incoherent undersampling technique to a radio frequency (RF) test is further improved by the development of a new test architecture for linearity testing of RF transmitter components. The proposed technique actually removes the requirement of any frequency/phase locking between the periodic amplitude modulation envelope waveform and the periodic carrier waveform. Such amplitude modulated waveforms are usually aperiodic, and instead have two separate periods, one for the envelope and one for the carrier. Modified period estimation and reconstruction techniques were developed to enable the reconstruction of such amplitude modulated signals, with the capability to reconstruct the signals over a wide range of modulation index leading to the extraction of the instantaneous carrier amplitude and phase with varying envelope phase. The proposed technique achieves separation of the amplitude and the phase information leading to a better estimation of the amplitude-to-amplitude and amplitude-to-phase effects introduced by a nonlinear device under test (DUT).

A major barrier to the adaptation of such a low-cost system, where a trade-off is achieved between the accuracy and the cost of the system, is the difficulty in estimating the system-level loss of yield and test overkill using the low-cost test equipment. The difficulty in estimating such numbers arises from the prohibitive cost of simulating complex systems to estimate the impact of a parametric variation at the device level on the system's input-output behavior. Such systems often consist of high accuracy analog cores controlled by digital algorithms. This thesis proposes, an end-to-end, efficient system level simulation framework. A new metastability model of the regenerative comparator latch is developed to enable such a simulation flow. The proposed simulation flow allows the component level behavior in the continuous time domain to be elevated to transition probabilities in a system-level discrete-time domain for event-driven Markov chain based simulation flow.

In light of the above discussion, the main contributions of the present research can be summarized as follows:

- The research develops a low-cost time domain metric for period estimation in the presence of frequency drifts
- The research extends basic incoherent undersampling based test architecture to beyond track and hold bandwidth
- The research develops sampling strategies to extend simple time-domain period estimation techniques to multi-band architecture while maintain the undersampling framework
- The research demonstrates that linear phase noise scaling in the multichannel acquisition can lead to the possibility of measuring timing jitter
- The research extends the proposed technique to RF testing for the non-linearity of transmitter components
- The research enables a system-level simulation framework which can estimate the impact of physical parameter variation not only at the device level but also for an

entire system of complex mixed-signal systems

Despite these contributions, there is much room for improvement of the achieved results for future applications. Some of the possible future research directions are listed in the following section.

7.1 Future scope

This section, investigates in detail, the future scope of improvement in the proposed solutions. The main scope of future research includes the improvement of the reconstruction algorithms and post-processing techniques to extract information from the signal about timing noise. The details are given in the following subsections.

7.1.1 Improvement in the equalization techniques for multichannel acquisition

The technique of combining incoherent undersampling with bandwidth interleaving as developed in this thesis requires for its proper operation equalization of the distortions introduced by the channels. However, estimating the channel response, requires that the proposed technique rely on the availability of a reference reconstruction. The cost of a reference-based calibration can significantly limit the usability of the proposed test architecture. Hence, it is desired that the calibration be as reference-free as possible. In the future, such blind reference-free channel estimation techniques could be developed.

In this thesis the impact of the mixer non-linearity on the final reconstruction is ignored. It is necessary to be able to estimate the impact of the mixer non-linearity on the system accuracy. It will be necessary to develop correction techniques against mixer non-linearity to improve the operable power range of the proposed test system and to relax the specifications requirement of the mixer, which should lead to further cost reduction.

7.1.2 Timing noise measurement

While the measurement of timing noise was previously demonstrated in classical incoherent undersampling system, it is not clear how the noise scales through such systems,

especially in the presence of dispersion effects introduced by the data acquisition path. Every measurement setup introduces some degree of linear filtering of the signal waveform, nonlinear distortions, and noise. The relationship of the measured jitter at the output of a test setup to the input jitter is complex. Due to the free running behavior of the signal waveform and the sampling clock in an incoherent undersampling-based setup, the accumulated phase noise in the test setup can be unbounded, and over time can easily overwhelm the input signal jitter. Undersampling leads to further complexity due to the spectral aliasing of wide-band noise, and the lack of an estimate of the instantaneous slope of the signal waveform. Under these conditions, small order perturbation analysis is not valid and the standard assumption of noise equi-partition between amplitude noise and phase noise may not hold. Further, due to the non-linear phase response of the measurement setup, there is a possibility of interconversion between phase noise and amplitude noise which can lead to an erroneous measurement of the jitter distribution. Moreover, in multi-channel acquisition, the noise measured from each band is correlated and these noise components cannot be combined in a straight forward manner to evaluate the total noise. This thesis demonstrates the possibility of measuring slowly varying (close in) phase noise. However, what still needs to be verified is whether or not the measurement scaling factor and accuracy depend on the nature of the acquired waveform or on the nature of the noise distribution, especially for comparatively fast varying phase noise components. For completeness, a theoretical framework needs to be developed for such a system.

7.1.3 Adaptation of the proposed system simulation flow to complex systems

The proposed simulation flow developed in this thesis for the system level impact assessment of physical parameter variation at the device level needs to be further developed for better accuracy. This thesis demonstrates the basic technique using a small system of a delay locked loop using a digitally-controlled phase rotator. However, it would be much more useful to apply the technique to complex real-life systems like an ADC, a digital to analog converter (DAC), etc.. This will involve application and development of sophisticated model order reduction techniques as well as system-level simulation frameworks to achieve

reasonable reduction in simulation time without significantly sacrificing the accuracy of the simulation results.

REFERENCES

[1] F. Bien, H. Kim, Y. Hur, M. Maeng, J. Cha, S. Chandramouli, E. Gebara, and J. Laskar, "A 10-gb/s reconfigurable cmos equalizer employing a transition detector-based output monitoring technique for band-limited serial links," *Microwave Theory and Techniques, IEEE Transactions on*, vol. 54, pp. 4538 –4547, dec. 2006.

[2] K. Hyoungsoo, J. de Ginestous, F. Bien, L. Kil-Hoon, S. Chandramouli, H. Youngsik, C. Scholz, E. Gebara, and J. Laskar, "An electronic dispersion compensator (edc) with an analog eye-opening monitor (eom) for 1.25-gb/s gigabit passive optical network (gpon) upstream links," *Microwave Theory and Techniques, IEEE Transactions on*, vol. 55, pp. 2942 –2950, dec. 2007.

[3] T. Ellermeyer, U. Langmann, B. Wedding, and W. Pohlmann, "A 10-gb/s eye-opening monitor ic for decision-guided adaptation of the frequency response of an optical receiver," *Solid-State Circuits, IEEE Journal of*, vol. 35, pp. 1958 –1963, dec. 2000.

[4] B. Analui, A. Rylyakov, S. Rylov, M. Meghelli, and A. Hajimiri, "A 10-gb/s two-dimensional eye-opening monitor in 0.13- mu;m standard cmos," *Solid-State Circuits, IEEE Journal of*, vol. 40, pp. 2689 – 2699, dec. 2005.

[5] D. Bhatta, K.-H. Lee, H. S. Kim, E. Gebara, and J. Laskar, "A 10gb/s two dimensional scanning eye opening monitor in 0.18um cmos process," in *Microwave Symposium Digest, 2009. MTT '09. IEEE MTT-S International*, pp. 1141 –1144, june 2009.

[6] W. Black and D. Hodges, "Time interleaved converter arrays," *Solid-State Circuits, IEEE Journal of*, vol. 15, pp. 1022 – 1029, dec 1980.

[7] N. Kurosawa, H. Kobayashi, K. Maruyama, H. Sugawara, and K. Kobayashi, "Explicit analysis of channel mismatch effects in time-interleaved adc systems," *Circuits and Systems I: Fundamental Theory and Applications, IEEE Transactions on*, vol. 48, pp. 261 –271, Mar. 2001.

[8] A. Petraglia and S. Mitra, "Analysis of mismatch effects among a/d converters in a time-interleaved waveform digitizer," *Instrumentation and Measurement, IEEE Transactions on*, vol. 40, pp. 831 –835, Oct. 1991.

[9] S.-W. Sin, U.-F. Chio, U. Seng-Pan, and R. Martins, "Statistical spectra and distortion analysis of time-interleaved sampling bandwidth mismatch," *Circuits and Systems II: Express Briefs, IEEE Transactions on*, vol. 55, pp. 648 –652, july 2008.

[10] J.-E. Eklund and F. Gustafsson, "Digital offset compensation of time-interleaved adc using random chopper sampling," in *Circuits and Systems, 2000. Proceedings. ISCAS 2000 Geneva. The 2000 IEEE International Symposium on*, vol. 3, pp. 447 –450 vol.3, 2000.

[11] M. Tamba, A. Shimizu, H. Munakata, and T. Komuro, "A method to improve sfdr with random interleaved sampling method," in *Test Conference, 2001. Proceedings. International*, pp. 512 –520, 2001.

[12] E. Candes and M. Wakin, "An introduction to compressive sampling," *Signal Processing Magazine, IEEE*, vol. 25, pp. 21 –30, march 2008.

[13] R. Lawton, S. Riad, and J. Andrews, "Pulse and time-domain measurements," *Proceedings of the IEEE*, vol. 74, pp. 77 – 81, jan. 1986.

[14] L. Noirie, F. Cerou, G. Moustakides, O. Audouin, and P. Peloso, "New transparent optical monitoring of the eye and ber using asynchronous under-sampling of the signal," in *Optical Communication, 2002. ECOC 2002. 28th European Conference on*, vol. 5, pp. 1 –2, 2002.

[15] I. Shake, H. Takara, and S. Kawanishi, "Simple measurement of eye diagram and ber using high-speed asynchronous sampling," *Lightwave Technology, Journal of*, vol. 22, pp. 1296 – 1302, May 2004.

[16] H. Choi and A. Chatterjee, "Jitter characterization of pseudo-random bit sequences using incoherent sub-sampling," *Asian Test Symposium*, vol. 0, pp. 9–14, 2010.

[17] H. Choi, A. V. Gomes, and A. Chatterjee, "Signal acquisition of high-speed periodic signals using incoherent sub-sampling and back-end signal reconstruction algorithms," *Very Large Scale Integration (VLSI) Systems, IEEE Transactions on*, vol. PP, no. 99, pp. 1 –11, 2010.

[18] N. Tzou, T. Moon, X. Wang, H. Choi, and A. Chatterjee, "Dual-frequency incoherent subsampling driven test response acquisition of spectrally sparse wideband signals with enhanced time resolution," in *VLSI Test Symposium (VTS), 2012 IEEE 30th*, pp. 140 –145, april 2012.

[19] A. Petraglia and S. Mitra, "High-speed a/d conversion incorporating a qmf bank," *Instrumentation and Measurement, IEEE Transactions on*, vol. 41, pp. 427 –431, jun 1992.

[20] S. Velazquez, T. Nguyen, S. Broadstone, and J. Roberge, "A hybrid filter bank approach to analog-to-digital conversion," in *Time-Frequency and Time-Scale Analysis, 1994., Proceedings of the IEEE-SP International Symposium on*, pp. 116 –119, oct 1994.

[21] G. Ding, C. Dehollain, M. Declercq, and K. Azadet, "Frequency-interleaving technique for high-speed a/d conversion," in *Circuits and Systems, 2003. ISCAS '03. Proceedings of the 2003 International Symposium on*, vol. 1, pp. I–857 – I–860 vol.1, may 2003.

[22] P. Pupalaikis and M. Schnecker, "A 30 ghz bandwidth, 80 gs/s sample rate real-time waveform digitizing system," in *Optical Fiber Communication (OFC), collocated National Fiber Optic Engineers Conference, 2010 Conference on (OFC/NFOEC)*, pp. 1 –3, march 2010.

[23] T. Kailath, A. Sayed, and B. Hassibi, "Linear estimation, ser," *Information and System Sciences Series. Upper Saddle River, NJ, USA: Prentice Hall*, 2000.

[24] D. Marelli, K. Mahata, and M. Fu, "Hybrid filterbank adcs with blind filterbank estimation," *Circuits and Systems I: Regular Papers, IEEE Transactions on*, vol. 58, pp. 2446 –2457, oct. 2011.

[25] J. Savir and Z. Guo, "Test limitations of parametric faults in analog circuits," *Instrumentation and Measurement, IEEE Transactions on*, vol. 52, no. 5, pp. 1444–1454, 2003.

[26] A. Abderrahman, M. Sawan, Y. Savaria, and A. Khouas, "New analog test metrics based on probabilistic and deterministic combination approaches," in *Electronics, Circuits and Systems, 2007. ICECS 2007. 14th IEEE International Conference on*, pp. 82–85, 2007.

[27] A. Bounceur, S. Mir, E. Simeu, and L. Rolndez, "Estimation of test metrics for the optimisation of analogue circuit testing," *Journal of Electronic Testing*, vol. 23, no. 6, pp. 471–484, 2007.

[28] F. Liu and S. Ozev, "Efficient simulation of parametric faults for multi-stage analog circuits," in *Test Conference, 2007. ITC 2007. IEEE International*, pp. 1–9, 2007.

[29] S. Sunter and N. Nagi, "Test metrics for analog parametric faults," in *VLSI Test Symposium, 1999. Proceedings. 17th IEEE*, pp. 226–234, 1999.

[30] K. Saab, N. Ben-Hamida, and B. Kaminska, "Parametric fault simulation and test vector generation," in *Design, Automation and Test in Europe Conference and Exhibition 2000. Proceedings*, pp. 650–656, 2000.

[31] N. Nagi, A. Chatterjee, and J. Abraham, "Fault simulation of linear analog circuits," *Analog Integrated Circuits and Signal Processing*, vol. 4, no. 3, pp. 245–260, 1993.

[32] E. Yilmaz, A. Meixner, and S. Ozev, "An industrial case study of analog fault modeling," in *VLSI Test Symposium (VTS), 2011 IEEE 29th*, pp. 178–183, 2011.

[33] M. Rewienski and J. White, "A trajectory piecewise-linear approach to model order reduction and fast simulation of nonlinear circuits and micromachined devices," *Computer-Aided Design of Integrated Circuits and Systems, IEEE Transactions on*, vol. 22, no. 2, pp. 155–170, 2003.

[34] C. Gu and J. Roychowdhury, "Model reduction via projection onto nonlinear manifolds, with applications to analog circuits and biochemical systems," in *Computer-Aided Design, 2008. ICCAD 2008. IEEE/ACM International Conference on*, pp. 85–92, 2008.

[35] A. Demir and P. Feldmann, "Stochastic modeling and performance evaluation for digital clock and data recovery circuits," in *Design, Automation and Test in Europe Conference and Exhibition 2000. Proceedings*, pp. 340–344, 2000.

[36] H. J. M. Veendrick, "The behaviour of flip-flops used as synchronizers and prediction of their failure rate," *Solid-State Circuits, IEEE Journal of*, vol. 15, no. 2, pp. 169–176, 1980.

[37] D. Chen, D. Singh, J. Chromczak, D. Lewis, R. Fung, D. Neto, and V. Betz, "A comprehensive approach to modeling, characterizing and optimizing for metastability in fpgas," in *Proceedings of the 18th Annual ACM/SIGDA International Symposium on Field Programmable Gate Arrays*, FPGA '10, (New York, NY, USA), pp. 167–176, ACM, 2010.

[38] L.-S. Kim and R. Dutton, "Metastability of cmos latch/flip-flop," *Solid-State Circuits, IEEE Journal of*, vol. 25, no. 4, pp. 942–951, 1990.

[39] L. Marino, "General theory of metastable operation," *Computers, IEEE Transactions on*, vol. C-30, no. 2, pp. 107–115, 1981.

[40] T. Polzer and A. Steininger, "Digital late-transition metastability simulation model," in *Digital System Design (DSD), 2013 Euromicro Conference on*, pp. 121–128, 2013.

[41] J. Kim, B. Leibowitz, J. Ren, and C. Madden, "Simulation and analysis of random decision errors in clocked comparators," *Circuits and Systems I: Regular Papers, IEEE Transactions on*, vol. 56, no. 8, pp. 1844–1857, 2009.

[42] P. Nuzzo, F. De Bernardinis, P. Terreni, and G. Van der Plas, "Noise analysis of regenerative comparators for reconfigurable adc architectures," *Circuits and Systems I: Regular Papers, IEEE Transactions on*, vol. 55, no. 6, pp. 1441–1454, 2008.

[43] P. Figueiredo, "Comparator metastability in the presence of noise," *Circuits and Systems I: Regular Papers, IEEE Transactions on*, vol. 60, no. 5, pp. 1286–1299, 2013.

[44] A. Demir, E. Liu, and A. Sangiovanni-Vincentelli, "Time-domain non-monte carlo noise simulation for nonlinear dynamic circuits with arbitrary excitations," *Computer-Aided Design of Integrated Circuits and Systems, IEEE Transactions on*, vol. 15, pp. 493–505, May 1996.

[45] D. Bhatta, J. Wells, and A. Chatterjee, "Time domain characterization and test of high speed signals using incoherent sub-sampling," in *Test Symposium (ATS), 2011 20th Asian*, pp. 21 –26, nov. 2011.

[46] W. Bosch and G. Gatti, "Measurement and simulation of memory effects in predistortion linearizers," *Microwave Theory and Techniques, IEEE Transactions on*, vol. 37, no. 12, pp. 1885–1890, 1989.

[47] C. Clark, G. Chrisikos, M. S. Muha, A. A. Moulthrop, and C. P. Silva, "Time-domain envelope measurement technique with application to wideband power amplifier modeling," *Microwave Theory and Techniques, IEEE Transactions on*, vol. 46, no. 12, pp. 2531–2540, 1998.

[48] M. Abouchahine, A. Saleh, G. Neveux, T. Reveyrand, J. Teyssier, D. Barataud, and J. Nebus, "Broadband time-domain measurement system applied to the characterization of cross-modulation in nonlinear microwave devices," in *Microwave Symposium Digest, 2009. MTT '09. IEEE MTT-S International*, pp. 1201 –1204, june 2009.

[49] S. Sen, S. Devarakond, and A. Chatterjee, "Rapid radio frequency amplitude and phase distortion measurement using amplitude modulated stimulus," in *Test Symposium (ATS), 2010 19th IEEE Asian*, pp. 277–282, 2010.

[50] S. Sen, S. Devarakond, and A. Chatterjee, "Low cost am/am and am/pm distortion measurement using distortion-to-amplitude transformations," in *Test Conference, 2009. ITC 2009. International*, pp. 1–10, 2009.

[51] E. Erdogan and S. Ozev, "Detailed characterization of transceiver parameters through loop-back-based bist," *Very Large Scale Integration (VLSI) Systems, IEEE Transactions on*, vol. 18, no. 6, pp. 901–911, 2010.

[52] A. Banerjee, V. Natarajan, S. Sen, A. Chatterjee, G. Srinivasan, and S. Bhattacharya, "Optimized multitone test stimulus driven diagnosis of rf transceivers using model parameter estimation," in *VLSI Design (VLSI Design), 2011 24th International Conference on*, pp. 274–279, IEEE, 2011.

[53] R. Rashidzadeh, M. Ahmadi, and W. Miller, "Test and measurement of analog and rf cores in mixed-signal soc environment," *Computer-Aided Design of Integrated Circuits and Systems, IEEE Transactions on*, vol. 26, pp. 1855 –1865, oct. 2007.

[54] S. Ahmed, M. Saad El Dine, T. Reveyrand, G. Neveux, D. Barataud, and J. Nebus, "Time-domain measurement system using track amp; hold amplifier applied to pulsed rf characterization of high power gan devices," in *Microwave Symposium Digest (MTT), 2011 IEEE MTT-S International*, pp. 1 –4, june 2011.

[55] J. Hakkinen, P. Syri, J.-V. Voutilainen, and M. Moilanen, "A frequency mixing and sub-sampling based rf-measurement apparatus for ieee 1149.4," in *Test Conference, 2004. Proceedings. ITC 2004. International*, pp. 551 – 559, oct. 2004.

[56] H. Ku and J. Kenney, "Behavioral modeling of nonlinear rf power amplifiers considering memory effects," *Microwave Theory and Techniques, IEEE Transactions on*, vol. 51, no. 12, pp. 2495–2504, 2003.

[57] H. Ku, M. Mckinley, and J. Kenney, "Extraction of accurate behavioral models for power amplifiers with memory effects using two-tone measurements," in *Microwave Symposium Digest, 2002 IEEE MTT-S International*, vol. 1, pp. 139–142 vol.1, 2002.

[58] R. Vaughan, N. Scott, and D. White, "The theory of bandpass sampling," *Signal Processing, IEEE Transactions on*, vol. 39, pp. 1973 –1984, sep 1991.

[59] A. H. Jazwinski, *Stochastic processes and filtering theory*. Mathematics in science and engineering, New York: Academic press, 1970.

[60] W. A. M. Van Noije, W. Liu, and J. Navarro, S.J., "Precise final state determination of mismatched cmos latches," *Solid-State Circuits, IEEE Journal of*, vol. 30, no. 5, pp. 607–611, 1995.

[61] P. D. Lax, "Weak solutions of nonlinear hyperbolic equations and their numerical computation," *Communications on Pure and Applied Mathematics*, vol. 7, no. 1, pp. 159–193, 1954.

[62] H. Nessyahu and E. Tadmor, "Non-oscillatory central differencing for hyperbolic conservation laws," *Journal of Computational Physics*, vol. 87, no. 2, pp. 408 – 463, 1990.

[63] A. Kurganov and E. Tadmor, "New high-resolution central schemes for nonlinear conservation laws and convection–diffusion equations," *Journal of Computational Physics*, vol. 160, no. 1, pp. 241–282, 2000.

LIST OF PUBLICATIONS

[1] D. Bhatta, A. Banerjee, S. Deyati, N. Tzou, and A. Chatterjee, "Low cost signal reconstruction based testing of rf components using incoherent undersampling," *Journal of Electronic Testing*, vol. 30, no. 2, pp. 213–228, 2014.

[2] J. Natarajan, S. Kapoor, D. Bhatta, A. Chatterjee, and A. Singh, "Timing variation adaptive pipeline design: Using probabilistic activity completion sensing with backup error resilience," in *VLSI Design and 2014 13th International Conference on Embedded Systems, 2014 27th International Conference on*, pp. 122–127, IEEE, 2014.

[3] D. Bhatta, N. Tzou, S.-w. Hsiao, and A. Chatterjee, "Time domain reconstruction of incoherently undersampled periodic waveforms using bandwidth interleaving," in *Test Symposium (ATS), 2013 22nd Asian*, pp. 283–288, IEEE, 2013.

[4] N. L. Tzou, D. Bhatta, S.-W. Hsiao, and A. Chatterjee, "Periodic jitter and bounded uncorrelated jitter decomposition using incoherent undersampling," in *Proceedings of the Conference on Design, Automation and Test in Europe*, pp. 1667–1672, EDA Consortium, 2013.

[5] D. Bhatta, I. Mukhopadhyay, S. Natarajan, P. Goteti, and B. Xue, "Framework for analog test coverage," in *Quality Electronic Design (ISQED), 2013 14th International Symposium on*, pp. 468–475, IEEE, 2013.

[6] D. Bhatta, A. Bannerjee, S. Deyati, N. Tzou, and C. A., "Time domain reconstruction of signal envelope for high speed rf test setup using incoherent undersampling," in *Latin American Test Workshop, LATW 2013*, pp. 1–5, apr 2013.

[7] D. Bhatta, N. Tzou, H. Choi, and A. Chatterjee, "Spectral estimation based acquisition of incoherently under-sampled periodic signals: Application to bandwidth interleaving," in *Test Symposium (ATS), 2012 IEEE 21st Asian*, pp. 196 –201, nov 2012.

[8] N. Tzou, D. Bhatta, S.-W. Hsiao, H. W. Choi, and A. Chatterjee, "Low-cost wideband periodic signal reconstruction using incoherent undersampling and back-end cost optimization," in *Test Conference (ITC), 2012 IEEE International*, pp. 1 –10, nov 2012.

[9] S.-W. Hsiao, N. Tzou, D. Bhatta, and A. Chatterjee, "24ghz dual core pll design for 60 ghz transceiver and efficient validation methodology," in *Microwave Conference Proceedings (APMC), 2012 Asia-Pacific*, pp. 193 –195, dec 2012.

[10] D. Bhatta, J. Wells, and A. Chatterjee, "Time domain characterization and test of high speed signals using incoherent sub-sampling," in *Test Symposium (ATS), 2011 20th Asian*, pp. 21 –26, nov 2011.

[11] A. Trippe, E. Juntunen, D. Bhatta, K. Chuang, K.-H. Lee, J. Laskar, J. Papapolymerou, and E. Gebara, "An adaptive broadband bicmos active spur canceller," in *Microwave Symposium Digest (MTT), 2011 IEEE MTT-S International*, pp. 1 –4, jun 2011.

[12] D. Bhatta, K.-H. Lee, H.-S. Kim, E. Gebara, and J. Laskar, "A multi-ghz phase detector with auto-zeroing scheme for self-calibrated quadrature generation," in *Microwave Conference (EuMC), 2010 European*, pp. 656 –659, sep 2010.

[13] D. Bhatta, K.-H. Lee, H. S. Kim, E. Gebara, and J. Laskar, "A 10gb/s two dimensional scanning eye opening monitor in 0.18um cmos process," in *Microwave Symposium Digest, 2009. MTT '09. IEEE MTT-S International*, pp. 1141 –1144, june 2009.

[14] K.-H. Lee, D. Bhatta, H. Kim, E. Gebara, and J. Laskar, "A 10 gb/s coherent detection system with feed-forward equalizers for optical duobinary transmission," in *Microwave Integrated Circuits Conference, 2009. EuMIC 2009. European*, pp. 286 –289, sept 2009.

[15] K.-H. Lee, H. Kim, D. Bhatta, E. Gebara, and J. Laskar, "Performance analysis of feed-forward equalizers based on passive and active delay cells for multi-gb/s optical fiber links," in *Microwave Conference, 2008. APMC 2008. Asia-Pacific*, pp. 1 –4, dec 2008.